

University of Crete

**Foundation for Research &
Technology - Hellas**

Visualization and Control of the Electron Quantum Paths in High Field Laser- Atom Interactions

KOLLIPOULOS GEORGIOS



CRETE 2014

University of Crete

**Foundation for Research &
Technology - Hellas**

Visualization and Control of the Electron Quantum Paths in High Field Laser- Atom Interactions

KOLLIPOULOS GEORGIOS

Submitted as doctoral Thesis to
the Faculty of Physics of the
University of Crete,
Crete, Greece

Presented by
Kolliopoulos Georgios

Crete, September 2014

Supervisors:

Professor Dimitrios Charalambidis

Dr. Paraskevas Tzallas

Ευχαριστίες

Κατά την εκπόνηση της ανά χείρας διατριβής είχα την τύχη να βρω σημαντικούς συμπαραστάτες και αρωγούς. Πιστεύω βαθιά πως, δίχως την δική τους συμβολή, η ολοκλήρωση του έργου αυτού θα ήταν ίσως αδύνατη. Παράλειψη μιας έστω ελαχίστης αναφοράς στην προς εμέ προσφορά τους, θα ήταν σημάδι αγνωμοσύνης.

Θα ήθελα να ευχαριστήσω τον Καθηγητή κύριο Δημήτριο Χαραλαμπίδη για τις πολύτιμες παρεμβάσεις του σε κρίσιμα σημεία αυτής της προσπάθειας.

Τους Διδάκτορες κυρίους Hartmut Schroeder και Bergues Boris για την αποδοτική συνεργασία που είχαμε και ιδιαίτερα για την καθοδήγηση στη χρήση του Μικροσκοπίου Ιόντων. Επίσης, θα ήθελα να τους ευχαριστήσω για την όμορφη φιλοξενία που μου προσέφεραν στην Γερμανία και τις ωραίες συζητήσεις που είχα μαζί τους πάνω στη Φυσική με υπέροχες βουαρικές μπύρες ως γευστικούς συνοδούς.

Αγαπητά πρόσωπα με τα οποία συνυπήρξαμε ως μέλη της ίδιας ερευνητικής ομάδας και που, πέρα από την υλική βοήθειά τους στα πλαίσια της συνεργασία μας και του κοινού μας στόχου, μου προσέφεραν επίσης την φιλία και την ηθική τους στήριξη. Μια ελάχιστη αναφορά στην Διδάκτορα Κική Κοσμά, τον νυν Διδάκτορα Paolo Carpeggiani, τον Τάσο Μαυρή (για τον οποίον ιδιαίτερος ελπίζω οι λίγες γνώσεις ...ιστορίας, που έλαβε ως αντίδωρο για την βοήθεια και τον χρόνο που μου αφιέρωσε κατά τη διάρκεια νυχτερινών μετρήσεων, να τού παρέχουν μια μικρή ικανοποίηση) και τον Balázs Bódi, δεν θα μπορούσε να λείπει από το κείμενο αυτό.

Όπως επίσης, φυσικά, δεν θα μπορούσε να λείπει μια ιδιαίτερη αναφορά στους δύο παλαιότερους υποψηφίους διδάκτορες που είχα συναντήσει κατά την είσοδό μου στην ερευνητική ομάδα. Οι νυν Διδάκτορες Jann Kruse και Μανώλης Σκαντζάκης στάθηκαν πολύτιμοι βοηθοί για την εισαγωγή μου στο ερευνητικό πεδίο. Νιώθω μια ιδιαίτερη χαρά που η δική μου εργασία αποτελεί, σε αρκετά σημεία της, μια λογική συνέχεια των δικών τους εργασιών. Χρησιμοποιεί δε τεχνογνωσία και εμπειρία που συσσωρεύτηκαν με δικό τους κόπο.

Η τεχνική υποστήριξη που έλαβα από τους κ.κ. Αποστόλη Εγγλέζη, Γιάννη Λαμπράκη και Μιχάλη Λουλάκη, υπήρξε για εμένα πολύ σημαντική. Πολύς κόπος και πολύς χρόνος εξοικονομήθηκε χάρη στην δική τους φροντίδα. Η σωματική και η ψυχολογική μου καταπόνηση θα ήτανε πολύ μεγάλες δίχως τη δική τους αρωγή.

Στο ίδιο πλαίσιο, θα ήθελα να ευχαριστήσω και τους μηχανουργούς του Ιδρύματος Τεχνολογίας και Έρευνας. Στην δική τους αξιόπιστη, αποτελεσματική και πρόθυμη εργασία στηρίζεται αφανώς ένα μεγάλο μέρος της διατριβής αυτής.

Η απλή συμπερίληψή του σε ένα κείμενο ευχαριστιών σίγουρα δεν αρκεί για να εκφράσω την μεγάλη ευγνωμοσύνη που νιώθω απέναντι στον Διδάκτορα Γιώργο Τσακίρη. Η επαφή που είχα μαζί του δημιούργησε μερικές από τις επιστημονικά ωραιότερες στιγμές που έχω να θυμάμαι από αυτή την περίοδο της ζωής μου.

Και φυσικά, ίσως τίποτα από όσα καταγράφονται στη διατριβή αυτή δεν θα μπορούσε να έχει υπάρξει δίχως τις ιδέες, τον σχεδιασμό, την καθοδήγηση και την απεριόριστη βοήθεια του Διδάκτορος Παρασκευά Τζάλλα. Φοβάμαι όμως πως αυτό ίσως να μην τον ευχαριστεί αρκετά. Σίγουρα θα τον χαροποιεί η επίγνωση πως έχει συμβάλλει τα μέγιστα στην ολοκλήρωση μιας ακόμα διατριβής. Πιστεύω όμως πως η χαρά του θα ήταν πολλαπλάσια αν θα μπορούσε να πειστεί πως έχει συμβάλλει πραγματικά στην διαμόρφωση ενός ολοκληρωμένου επιστήμονα.

Θα ήθελα, τέλος, μέσα από αυτές τις γραμμές να εκφράσω και την ευγνωμοσύνη μου στους ανθρώπους (τους άγνωστους σε εμένα) που εργάστηκαν για την παραγωγή του λογισμικού ανοικτού κώδικα OpenOffice, με τη χρήση του οποίου έχουν γεμίσει οι σελίδες του κειμένου που διαβάζετε. Η αρτιότητα στην εμφάνιση νομίζω πως είναι γι' αυτούς μια μικρή δικαίωση. Ό,τι παρακίνησε στη δημιουργία του OpenOffice στέκει ως αντιπαράδειγμα σε κυρίαρχες σήμερα διδασκαλίες που θέλουν να βρίσκουν πάντα το κέρδος πίσω από ο,τιδήποτε χρήσιμο. Θέλω πολύ να πιστεύω πως η ευγενής νοοτροπία των ανθρώπων του OpenOffice δεν είναι παρά ένα κλείσιμο του ματιού και ένα χαμόγελο από ένα μέλλον που βρίσκεται ante portas.

*εδίψησέ σε η ψυχή μου, ποσαπλώς σοι η σάρξ
μου εν γη ερήμω και αβάτω και ανύδρω*

Ψαλμός τω Δαυΐδ 62, 2

CONTENTS

Chapter 1: Introduction

1.1 Chronoscopy	13
1.2 In this Thesis	15

Chapter 2: Theory

2.1 Strong light-matter interaction	17
2.1.1 Strong Field Approximation, Volkov propagator and Ponderomotive Energy	17
2.1.2 Ionization of atoms in the strong field regime	19
2.2 High-Order Harmonic Generation (HHG)	21
2.2.1 The puzzle of HHG process	21
2.2.2 The Three-Step-Model	23
2.2.2.1 <i>The classical three-step-model</i>	24
2.2.2.2 <i>The semi-classical three-step-model</i>	27
2.3 Phase-matching conditions for high-order harmonics	33
2.3.1 The role of field-gradient forces	33
2.3.2 Generalized phase-matching conditions for high-order harmonics	35
2.3.3 Dispersion	39

Chapter 3: Revealing Quantum Path Details in high-field Physics

3.1 Introduction	43
3.2 The ion-imaging-detector	44
3.3 Experimental procedure	46
3.4 Results & Discussion	49
3.4.1 Computer Simulation	49
3.4.2 Focusing structures taken from the experiment by one-photon ionization process	55
3.4.3 Focusing structures taken from the experiment by two-photon non resonant ionization process.....	57
3.4.4 The “saw-type” structure	57

Chapter 4: A single-shot XUV autocorrelator

4.1 Introduction	63
4.2 The concept	64
4.3 Model calculation	66
4.4 Setup optimization	70
4.4.1 Calculation of the diffraction integral	70
4.4.2 Two-aperture mask	71
4.4.3 Two-slit mask	72
4.4.4 Beam splitter	72
4.5 Setup assessment	76
4.5.1 Efficiency comparison	76
4.5.2 Parameter selection	78
4.5.3 Ionization estimates	80
4.6 Summary	82

Chapter 5: A compact collinear polarization gating scheme for many-cycle laser pulses

5.1 The Gating Technique	85
5.2 Concept and description of the Collinear Many-cycle Polarization Gating Scheme	88
5.3 Experimental results and discussion	91
5.4 Computer simulation - Results and discussion	94
5.5 Conclusions	98

REFERENCES	101
-------------------------	-----

1st Chapter

Introduction

*“Mehr Licht!”
 (“More Light!”)*

*Johann Wolfgang von Goethe's last words
(1749-1832)*

1.1 Chronoscopy

For humanity, scientific research and knowledge have been the major means leading to mental and sentimental maturity. Legends have been overthrown from their high positions as sacred narrations which contain the True scenario of the Cosmogony and they are restricting themselves only to be considered as valuable sources of information about humanity's mental nature. Nature insists to exist separately from human will and does not reveal its secrets by mystic revelation in human minds. In order to keep satisfying the inherent need of understanding and controlling Nature, human societies have started to substitute mystic revelation and magic with, more effective means, research and technology. Humanity has started to accept the “humiliation” of the fact that they do not stand at the center of the Universe and they are not the unique reason why everything exist. They start even to understand that all the important facts in the Universe do not happen at the space and time-scales which are appropriate to the human ones. Nevertheless, these macro- or micro-events still are influential to human life and lots of aesthetic and practical benefits come out from the investigation of the Macrocosm and the Microcosm. And as human perception is built for the human-scale Cosmos, only Technology can help it to penetrate into the realms of the Macro and Micro.

In order to take a look inside the Microcosm, in space or time, one requires a physical quantity with a well-controlled spatial or temporal variation. In space such a gradient can be introduced by the radial profile of a light or electron focused beam or by a tip. The technique is called *microscopy*. Correspondingly, in the temporal domain a physical quantity which presents a rapid variation in time needs to be introduced. The use of such a sharp temporal gradient, for measuring and visualizing brief processes is often called *chronoscopy*, or *time-resolved metrology*.

Since the second half of the 19th century, it was already known that by using short flashes of light

rapid phenomena could be recorded which could not otherwise be perceived by the naked eye. Various techniques which allowed the recording of freeze-frame snapshots, were introduced just a few decades after the invention of the photography by Nicéphore Niépce and others in 1820's. The principles of the *Stop-Motion Photography* started to emerge. From 1859 to 1864, Toepler elaborated a pioneering method, managing to obtain with it a complete history of sound wave phenomena^[1]. He generated sound waves with a short light spark (pump) and subsequently photographed them with an electronically delayed second spark (probe). *Pump-probe spectroscopy* was born. In 1899, Abraham and Lemoine^[2] improved the resolution of pump-probe spectroscopy by introducing a simple optical synchronism between the pump and the probe flash, commonly used in nowadays. They derived the pump and probe flashes from the same spark with a variable optical path length between them. This way, the temporal resolution of the method was improved to the limit set by the flash duration, the nanosecond duration of pulses of incoherent light. Here was the point where the progress in time-resolved imaging reached a first halt. Further advance on this field was demanding a radical development of new sources of light and their concomitant new techniques.

Technological breakthroughs, which allowed a new boost, came almost half a century later. Transistors^[3] succeeded to control fast switching of the electric current in the sub-nanosecond scale regime, while the invention of the first LASER (**L**ight **A**mplification by **S**timulated **E**mission of **R**adiation), by Theodore Maiman in 1960^[4], opened the way to a huge number of applications based on light-matter interactions in unthinkable, up to that time, spatial, temporal and energy scales. The first pulsed lasers had durations of several hundreds of microseconds, but the invention of the Q-switch by Hellwarth in 1962^[5] offered to the pulse duration a four-order-of-magnitude decrease. Few years later, in 1966, DeMaria et al.^[6] proposed the Mode-Locking technique which, in combination with the use of broad-gain dye laser media, resulted in a further reduction of the pulse duration down to the sub-picosecond regime. Then, one had had to wait another ten to fifteen years until the moment when another 3-order reduction took place. The use of solid state lasers, especially the introduction of the Ti:Sapphire crystal as a gain medium^[7] in 1980's, in combination with the invention of intra-cavity group velocity dispersion compensation techniques, led to the production of laser pulses with duration of just a few femtoseconds^[8]. The road to Femtochemistry had just been built.

The atoms within molecules (reactants) rearrange themselves to form new molecules (products). Chemical bonds break, form, or geometrically change with awesome rapidity. Before the mature growth of the scientific direction of Femtochemistry, these atomic transformations, which involve ultrafast displacements of electrons and atomic nuclei, had never been observed in real time. In order to take an idea about the duration of these procedures, one has to consider that the speed of atomic motion in a molecule is around 1 km/sec. So, in order to record the dynamics over a distance of an angstrom, one requires a good time resolution within a time interval of around 100 femtoseconds. Femtochemistry, similar to the “stop-motion” photography, uses femtosecond lasers as stroboscopes and, hence, becomes able to “freeze”* atoms in motion in order to study the evolution of molecular structures during the reactions. The field began in the middle of 1980's with simple systems of a few atoms. However until the year 1999, when Ahmed Hassan Zewail (the “father of Femtochemistry”) was awarded the Nobel Prize in Chemistry, it had already reached the realm of biological systems such as proteins and DNA^[9].

The triumph of Femtochemistry pushed the scientific community to seek for techniques at smaller time-scales in order to observe, in real-time, processes that take place inside the atom. Scientists wished to give birth to a descendant of Femtochemistry; the Atto-physics**. At this new field, the goal would be to “freeze”* the motion of the electrons in the atoms. Taking into consideration that, according to the Bohr atomic model, an electron needs about 150 attoseconds in order to circle the

* By “Freezing” we mean that, for the pulse duration used, they do not have enough time to move far away.

** 1 attosecond = 10^{-18} sec

nucleus of an Hydrogen atom^{***}, one can take a rough idea about the range of pulse durations needed. They stand in the sub-femtosecond realm. At this point, the scientific community had come to an other halt. Given that a pulse of light should be at least one cycle long, the spectrum of a sub-femtosecond pulse has to be centered in the Extreme Ultraviolet (XUV) range. However, laser sources at such wavelengths did not seem to exist.

In early 1990's a scheme was slowly emerging that had the potential to break the "femtosecond barrier". In 1990, Theodor Hansch suggested^[10] that a pulse of a few attoseconds could be possibly generated from the Fourier Synthesis of a comb of equidistant frequencies in the spectral domain with controlled relative phases. Source of his inspiration had been of course the operation of the mode-locked laser. In 1992, Farkas and Tóth^[11], combining Hansch's idea with the remarkable features of the High-order Harmonic Generation (HHG) process which had been coming out from numerous experiments the past years, realized that the HHG plateau could be a possible relatively simple source of sub-femtosecond pulses. The key to go beyond the femtosecond barrier had just been provided.

The following 10-15 years (around the second millennium) was the period during which Attoscience^[54] developed its basic toolbox. Various techniques in order to generate and to characterize subfemtosecond pulses in trains, in pairs or single ones have been proposed and elaborated^[12,13,14,15,58,77,101,125]. Attosecond pulses emerge from a large number of coherent atomic dipole emitters. The coherence is the result of the atomic dipoles being driven by a (spatially) coherent laser field and the nature of the electronic response of the ionizing atoms.

An important feature of the attosecond science is that the XUV generation is associated with electron emission and recollision processes which are taking place during the non-linear interaction of the driving laser field with the medium (atom, molecule or solid). The duration of this process stands in the attosecond time scale while the wavelength of the re-collided electron can drop below the 1 Angstrom. This mechanism which combines the electron dynamics with the properties of the emitted XUV radiation, provides the possibility to reveal unique information in the atomic level with ultra high temporal resolution. Furthermore, the generation of intense attosecond pulses and the development of approaches with high degree of synchronization pushed the field of Attosecond science to perform experiments in all state of matter and study the dynamics with ultra high spatiotemporal resolution.

Since the early 2000's, experiments using attosecond technology gave answers to questions that a few decades ago physicists would hesitate even to ask. Uiberacker et al.^[18] experimentally examined how electrons escape from their atomic binding potential under the influence of a strong optical field and found that they are set free during a time window of less than 400 attoseconds near each field maximum of the ionizing few-cycle laser field. Drescher et al.^[19] succeeded to provide direct time-domain observation of the decay of an inner-shell vacancy in isolated atoms through Auger relaxation. A lot of other experiments of equal importance took place during the last decade making Attoscience a field where experimentalists do not let the theorists to get bored, challenging constantly their established theories and creating need for new ones.

1.2 In this Thesis

The work described in this present thesis is focused on the study of the recollision process in high order harmonic generation (chapter 3), the generation of intense isolated attosecond pulses by using high power multicycle driving laser field and the temporal characterization of these pulses by means of a single-shot autocorrelation approach. Briefly, the thesis is divided in 4 distinct parts.

Chapter 2 provides the necessary theoretical background of the high order harmonic generation

^{***} Assuming that it moves in a circular orbit of radius equal to the Bohr radius.

and attosecond pulse formation process while in Chapter 3 a unique method for revealing the quantum path details of the recollision process is demonstrated. This is done by mapping the electron wave-packet interferences which provide access to the intricacies of the generation of high order harmonics. This has been achieved by visualizing their EUV-spatial-amplitude-distribution interference pattern created by spatiotemporal overlapping the “*Short*” and “*Long*” trajectory harmonics. Due to high degree of accuracy that the present approach provides, the quantum nature of the recollision process has been demonstrated for the first time. This is done by quantitatively correlating the photoemission time and the electron quantum path length differences taking into account the energy-momentum transfer from the driving laser field into the system.

In Chapter 4 a novel single-shot second-order autocorrelation scheme for temporal characterization of the XUV radiation is presented. It is based on an ion imaging technique, which provides spatial information of the ionization products in the focal volume of the XUV beam. An evaluation towards selecting an optimum configuration has been performed, using simple analytical and detailed numerical modeling. The implementation of the concept is discussed and the proposed setups are assessed.

Finally, in Chapter 5 we present the implementation of a new collinear, compact, “user-friendly” and with long term stability Polarization Gating Apparatus. We demonstrate the generation of a broadband coherent continuum extreme-ultraviolet (XUV) radiation produced by the interaction of gases with a many-cycle infrared (IR) laser field elliptically modulated by this Gating Apparatus. An ultra-short temporal gate, with high energy content, is formed and the XUV emission is restricted therein. The gate width has been measured and is in agreement with the theoretical calculations. The spectral width of the emitted XUV radiation can support isolated pulses of 200 attoseconds duration.

2nd Chapter

Theory

2.1 Strong light-matter interaction

A great number of important physical phenomena associated with attosecond science originate from the strong light-matter interaction. In this chapter we will briefly describe the ones most relevant to our research.

When a laser field interacting with an atom or a molecule is weak*, conventional time-dependent perturbation theory^[20] allows us to understand and describe almost everything. But what can we do when the perturbation theory is no longer applicable? This is what happens when the laser field is comparable or stronger than the atomic field. Theoretical models based on the Strong Field Approximation (SFA) and pioneered by Keldysh, Reiss and Faisal^[21-23], provided an answer to this question.

2.1.1 Strong Field Approximation, Volkov propagator and Ponderomotive Energy

The time-dependent Schrodinger equation (atomic units are used):

$$i \frac{\partial}{\partial t} |\Psi\rangle = \hat{H}(t) |\Psi\rangle \quad (2.1),$$

has a formal solution:

* Here, “weak” means that the laser field strength [given by $E(\text{V/cm}) = 27.4 \cdot \sqrt{I(\text{W/cm}^2)}$] is much smaller compared to the atomic field “seen” by a valence electron ($\sim 10^9$ V/cm for the Hydrogen atom in the ground state).

$$|\Psi(t)\rangle = e^{-i\int_0^t \hat{H}(t') dt'} |\Psi(t=0)\rangle \quad (2.2).$$

In the end, we try to substitute the operator $\exp(-i \int_0^t \hat{H}(t') dt')$ with a number $\exp(-i \int_0^t E(t') dt')$ where $E(t)$ is energy. Such a substitution can be made rigorously for a free electron in the presence of an arbitrary polarized laser field. This is what the SFA intends to exploit.

Let's try to summarize the physical picture in a few lines. In a low-frequency field* the electron, still in the ground state, follows slow oscillations of the laser field. In other words, the atom cloud is polarized by the laser field. If the electron manages to escape from bound states to the continuum, its motion is mainly influenced by the oscillating laser field and the presence of the parent ion does not provide but a probability of rescattering or recombination. As a consequence, in equation (2.2), instead of the exact propagator $\exp(-i \int_0^t \hat{H}(t') dt')$ we will use an approximate propagator $\exp(-i \int_0^t \hat{H}_F(t') dt')$ which includes the laser field fully and exactly but completely ignores the field-free binding potential of the system \hat{V}_A :

$$\hat{H}_F \equiv \hat{H} - \hat{V}_A \quad (2.3).$$

This approximation is the essence of the SFA and takes advantage of the fact that the propagator of the free electron in the laser field, the so-called Volkov propagator^[24], is known analytically.

If the “free”** electron escapes in the continuum at an instant t' with velocity \vec{v}' , then its velocity \vec{v} at any later time t will be:

$$\vec{v} = \vec{v}' + \frac{q}{m} \vec{A}(t') - \frac{q}{m} \vec{A}(t) \quad (2.4),$$

where q and m are the electron charge and mass and $\vec{A}(t)$ is the vector-potential of the electric field. The conserved quantity $\vec{P} \equiv m\vec{v}(t) - q\vec{A}(t)$, in the formula (2.4), is **the canonical momentum**.

From (2.4) we can reason that the instantaneous energy during the oscillations is:

$$U(t) = \frac{1}{2} m [\vec{v}' - q\vec{A}(t') + q\vec{A}(t)]^2 \quad (2.5).$$

It is very important to note here that $U(t)$ is independent from the position of the electron. The force exerted on the electron by the laser field, at each moment, is considered to be the same everywhere in space.

According to the above, the Volkov propagator is given by:

$$e^{-i\int_{t'}^t \hat{H}_F(t'') dt''} |\vec{v}'\rangle = e^{-i\int_{t'}^t U(t'') dt''} |\vec{v}\rangle \quad (2.6),$$

where $|\vec{v}'\rangle$ and $|\vec{v}\rangle$ represent the plane waves $\exp[i\frac{m\vec{v}}{\hbar}\vec{x}]$.

It is very interesting also to check how easily one can extract the so-called ponderomotive energy U_p (i.e. the mean kinetic energy of the electron during its quiver motion away from the parent ion) from equation (2.5). We just have to consider $\vec{v}'(t'=0) = 0$, which means that the electron appears in the continuum with zero initial longitudinal velocity (component of the velocity parallel to the

* “Low” in comparison to the characteristic response frequency of the system

** The quotation marks are added because the electron is not really free. It remains exposed to the influence of the laser field.

direction of the electric field). We also have to remember that the electric field \vec{F} is connected to the vector-potential via the formula:

$$\vec{F}(t) = - \frac{\partial \vec{A}(t)}{\partial t} \quad (2.7).$$

Then, by calculating the mean value within one cycle of the laser field, we obtain the very important result:

$$U_p = \frac{q^2 F^2}{4m\omega^2} \quad (2.8).$$

2.1.2 Ionization of atoms in the strong field regime

When a strong laser field interacts with an atom, every bound electron starts to “feel” the presence of this external field by the periodic change induced to the potential well in which it is energetically located.

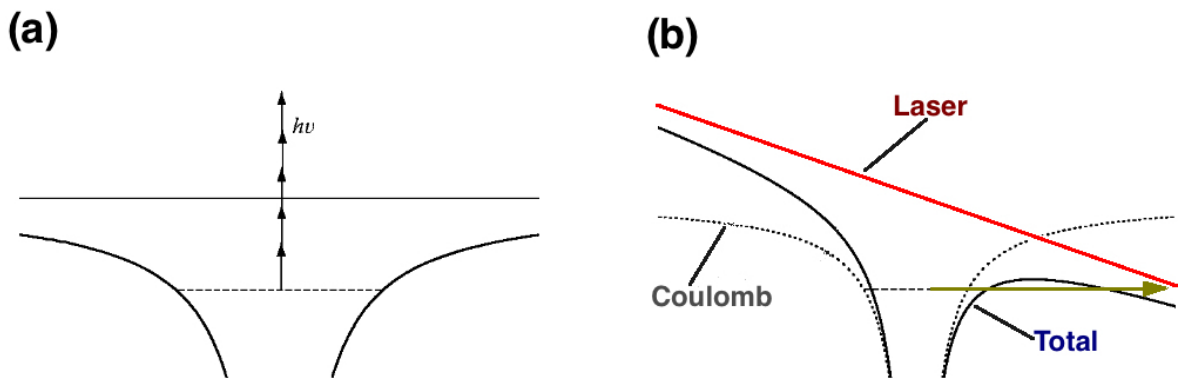


Figure 2-1: (a) Multiphoton ionization channel ($\gamma \gg 1$). (b) Tunneling ionization channel ($\gamma \ll 1$).

The potential well is being distorted and shaken in each laser cycle only if the well has a reasonable size*. Then, ionization can occur via multiphoton process or tunneling, leading to two different ionization channels which may coexist.

Following the first channel (multiphoton), ionization proceeds via the classically allowed region (as shown in Figure 2-1(a)). According to a simplified classical description^[25], the electron “heated” by the shaking walls of the potential well, may gain enough energy to slip out of the well. This mechanism becomes more probable as the size of the well is increased and as the laser frequency is not too low in comparison with the electronic response time. Consequently, for low-frequency** laser fields and for ground states, which means small and deep effective well size (i.e. atomic ground states), this “classical” multiphoton channel of ionization is not very likely*. In other words,

* There cannot be distortion of a delta-function potential.

** “Low” compared to the electronic response time.

* Unless a resonance with some excited state takes place, which slows down the electronic response time.

the MPI channel comes less significant as the laser frequency decreases and the ionization potential (I_p) increases.

On the other hand, the second channel (tunneling ionization) is based on the possibility of the electron to tunnel through the barrier which is created every half-cycle of the driving field [as shown in Figure 2-1(b)]. If the frequency of the laser is very low, which can be interpreted as the inverse of the frequency being much bigger than the time the electron needs to tunnel out through the distorted potential, the barrier can be considered as quasi-static. In this case, the ionization is dominated by electron tunneling. The whole process can be described quite well by using the essential formulas which describe an electron tunneling through a barrier distorted by a constant Coulomb potential. Consequently, tunneling becomes the prevailing ionization channel as the laser frequency decreases and the ionization potential increases.

There is also a third case which stands in between the two described above. If the laser frequency is not “so-low”, the barrier moves while the electron tunnels, leading to changes in the electron energy under the barrier. This last case consists practically of a mixture of the multiphoton and tunneling ionization already described. The electron is “heated” by the shaking walls and tunnels through the moving barrier as well. To deal theoretically with this problem is quite harder.

In 1964, Keldysh introduced^[21] his famous parameter γ [see the equation (2.9)] in order to identify quantitatively the contribution of each of the two ionization channels. In reality, this parameter expresses a comparison between the tunneling time τ^{**} and the laser period T .

$$\gamma \equiv \sqrt{\frac{I_p}{2 U_p}} \quad (2.9),$$

Keldysh has already proposed^[21] to define tunneling time as the time that a classical particle would have taken in order to traverse the barrier if the motion had been classically allowed. Let's consider a simple example. For a binding energy I_p and a short-range potential, the velocity of the particle travelling through a triangular barrier created by a constant electric field is given in time as: $v(t) = v_{max} - Ft$, with $v_{max} = \sqrt{2 I_p}$ being the velocity at the entrance into the “classically forbidden region”. Setting $v(\tau) = 0$, we obtain for the tunneling time τ :

$$\tau = \frac{v_{max}}{F} = \frac{\sqrt{2 I_p}}{F} \quad (2.10).$$

By taking into account expressions (2.8), (2.9) and (2.10), we see that:

$$\omega \tau = \frac{\omega \sqrt{2 I_p}}{F} = \sqrt{\frac{I_p}{2 U_p}} \equiv \gamma \quad (2.11),$$

ω being the angular frequency of the laser field.

For $\gamma \ll 1$, the barrier can be considered as remaining static during the motion of the electron through it. Nevertheless also for $\gamma > 1$, as mentioned before, we cannot say that tunneling does not take place. The difference here is that the electron absorbs energy while penetrating the barrier. As the electron increases its energy, the barrier is seen as “narrower” for it and the electron escapes more easily. This is the way the two channels of ionization, the classical multiphoton one and the tunneling one, are combined. Everything takes place inside the classically forbidden region.

For reasons of efficiency in the generation of High-order Harmonics [see section 2.2], the experimental conditions for the work in the present thesis are selected in such a way that condition

** The time that the electron needs to pass through the barrier [see figure 1-1(a)]

$\gamma \ll 1^*$ is fulfilled. For the rest of this Chapter we will focus in this region of γ values.

The ionization process, for $\gamma \ll 1$, is treated successfully by mainly two analytical approximations. The one is the Keldysh approximation^[21] and the other is the Ammosov-Delone-Krainov approximation (ADK approximation)^[26]. Both are based on the adiabatic approximation which considers the light field as practically static during the ionization process. A general and common feature of the above two approximations is the exponential law which rules the ionization rate. As an example, the rate provided by ADK for the hydrogen atom can be expressed as:

$$W_H \propto I_p \exp\left(-\frac{4 I_p}{3 \hbar \omega_t}\right) \quad (2.12),$$

where $\omega_t = \frac{e F(t)}{\sqrt{2m I_p}}$.

The probability of ionization of an atom is decreasing in time by:

$$P(t) = 1 - \exp\left[-\int_{-\infty}^t W(t') dt'\right] \quad (2.13).$$

From equation (2.13) can one extract the total ionization yield generated at each moment t by a laser pulse, taking into account its temporal profile.

2.2 High-Order Harmonic Generation (HHG)

2.2.1 The puzzle of HHG process

In 1987, Mcpherson et al.^[27] discovered high-order harmonic generation (HHG). In experiments seeking to characterize perturbative low-order harmonic generation, they unexpectedly observed a large number of odd harmonics of the fundamental driving laser (3rd, 5th, 7th, 9th, 11th, 13th, 15th and 17th harmonics). An additional surprising fact was that the intensity of successively higher harmonic orders did not decrease significantly, as it would be expected from perturbative nonlinear optics [see Figure 2-2(a)]. Within a very short time, Anne L'Huillier and coworkers observed high-order harmonic emission using infrared driving lasers^[28] that generated an even more remarkable comb of harmonic frequencies. Schematically, the harmonic spectrum depicted three characteristic regions [see Figure 2-3]:

- Low-order Harmonics are situated in the so-called “pertubative” part, where the amplitudes of the harmonics are decreased exponentially as expected from the old perturbative theories. Their photon energies stand below the Ionization Potential (I_p) of the genetating medium.
- The “plateau” which follows, is the spectral interval where is located a comb of high-order harmonics of more or less equal amplitude [see Figure 2-3(b)].
- The abrupt cut-off at the end of the “plateau” [see Figure 2-3(b)].

* An IR pulsed laser of 35 fs duration, with carrier wavelength 800 nm and intensity in the range of 10^{14} W/cm² is used.

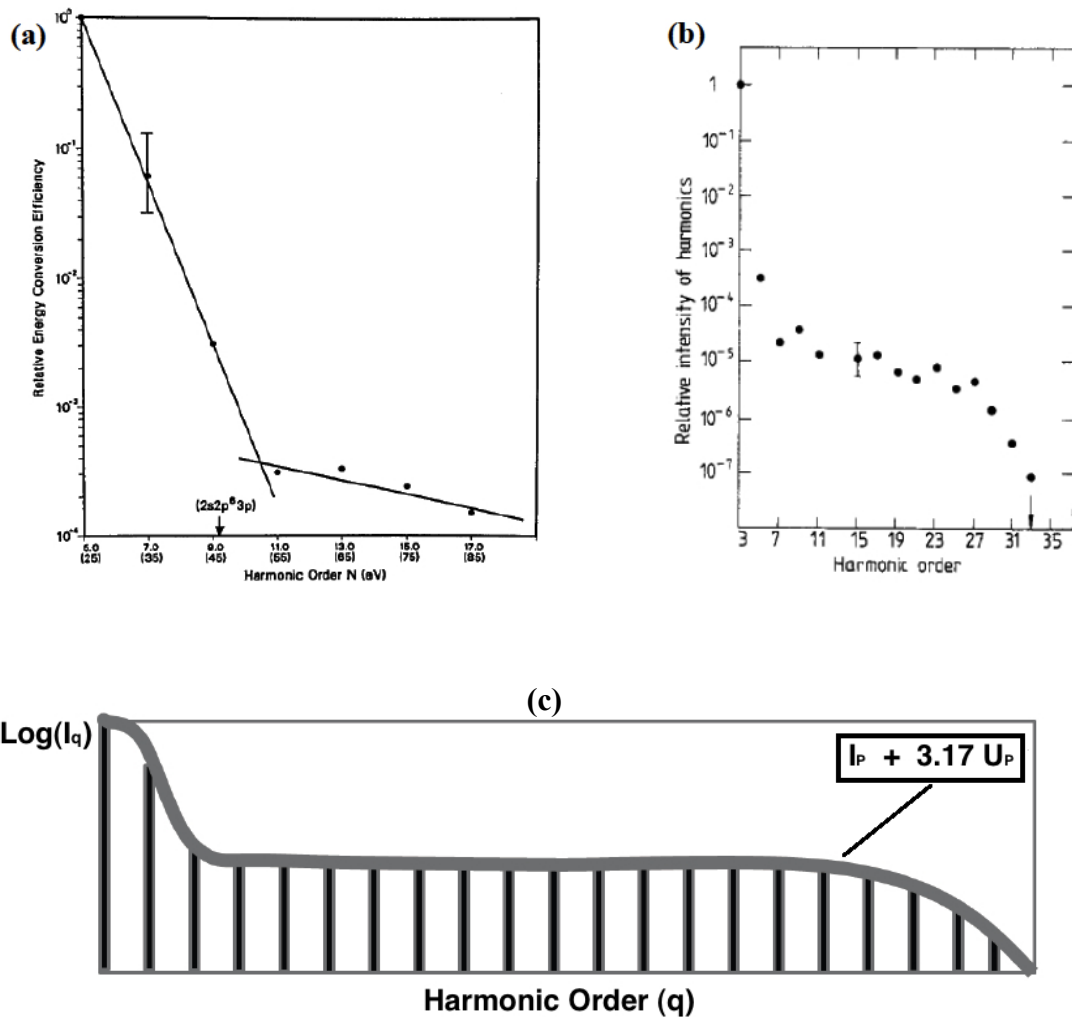


Figure 2-2: Discovery of HHG process in rare gases. Early figures in the scientific literature.

(a) A plot of the relative energy-conversion efficiency for harmonic generation in Ne shows a sharp change in slope between the ninth and eleventh harmonics. The arrow indicates the energy at which a 2s electron in the neutral becomes excited. For the seventh harmonic, the typical error bar is shown. The efficiency of the thirteenth harmonic is $\sim 2 \cdot 10^{-11}$. [Figure and caption from McPherson et al.^[27]]. (b) The relative intensity of the harmonics generated in Ar at a laser intensity of approximately $3 \cdot 10^{13} \text{ W cm}^{-2}$. The arrow indicates the highest harmonic order observed. The 13th harmonic is missing due to a strong absorption of the 81.9 nm radiation in the photoexcitation of a 5d state. [Figure and caption from Ferray et al.^[28]]. (c) A schematic diagram of a high-harmonic spectrum. The generic shape is shown as well as the associated cut-off energy provided by the three-step-model.

The above group of features gave a headache to the theorists who tried to give an explanation. The restriction to only odd-order harmonics which appear can be easily explained by taking symmetry reasons into consideration – the inversion symmetry of a gas medium precludes the generation of even-order harmonics. Nevertheless, the perturbative understanding of nonlinear optics could not

explain why many harmonics in the “plateau”, all of comparable intensity, are generated all together. This unique physics of the HHG process necessitated a new perspective and a new formalism.

The key to uncovering the physics underlying HHG is to understand how atoms respond to strong laser fields. This topic was appealing to a lot of scientists in the 1980s, when above-threshold multiphoton ionization was observed and studied^[29]. The time-dependent Schrodinger equation simulation of how a single electron is ionized from an atom by a strong laser field was already successfully used to explain the above-threshold multiphoton ionization. Kulander and coworkers used it again in order to reproduce the characteristic multiple harmonic spectra of HHG^[30]. Other groups tried to explain the basic HHG process, considering it to be a Raman-like process via continuum states^[31,32] and describing the recollision process in classical terms in the context of above-threshold multiphoton ionization^[33].

2.2.2 The Three-Step-Model

An intuitive picture of HHG appeared in the early 1990s. Based on simple classical considerations, explained well the universal form of the “plateau” and the “Cut-Off” region of the HHG spectrum. It was the so-called “three-step-model”^[34]. In this scheme, an electron is first liberated from an atom through strong field ionization (Step 1), is then accelerated by the laser field (Step 2), and finally recombines with the parent ion, emitting any excess energy as a high-energy photon (Step 3) [see Figure 2-3].

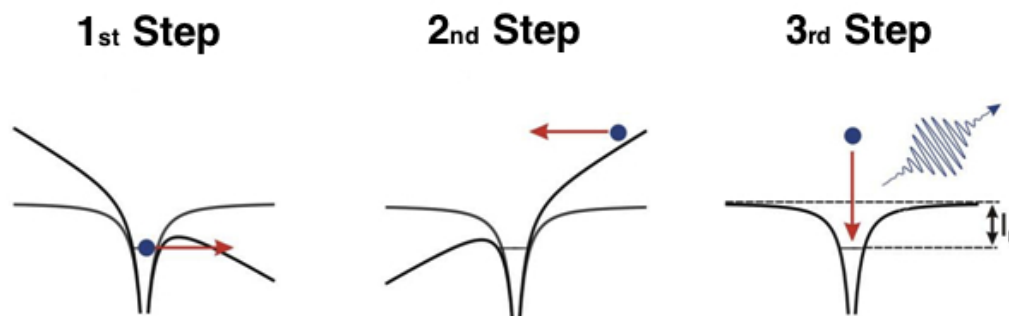


Figure 2-3: Schematic presentation of the three-step-model.

The three-step-model not only explained well the universal scheme of the HHG spectrum, but offered additionally a deep insight into the whole physical procedure revealing very important intrinsic features of the procedure. For instance, predictions like the dual contribution to each generated harmonic from two distinct classes (named later as “short” and “long”) of trajectories followed by the electron in the continuum (Step 2), or the inherent linear chirp of the harmonics, would be soon experimentally proved and consist until our days the most important guidelines concerned with the so-called “Atto-Science” and “pulse-engineering” in the attosecond scale.

Just a few months after the publication of the classical version of the “three-step-model” by Corkum^[34], a semi-classical (or semi-quantum) treatment* of the same basic concept appeared^[36]. Recovering the classical interpretations of Kulander et al^[35] and Corkum^[34], this work situated the ideas of the model in the quantum “linguistic” context of the Atomic Physics and revealed details not enough elucidated by the previous version. In particular, information about the phase of the

* “Semi-classical” has the sense here that the driving field is treated classically and not within a full quantum context.

harmonic emission -which is of utmost importance for our work (see Chapter 3)- is for the first time offered by this semi-classical description of the procedure.

Here, the classical model first and the semi-classical one second, will be briefly presented in order to introduce the reader into the core of the semantic frame in which is situated the work presented in this Thesis.

2.2.2.1 The classical three-step-model

By using the ADK tunnel ionization model^[7], one can show that the probability of ionization is a function of the laser electric field and is higher just after the peak of the oscillating field. As a result, a sequence of electron wave packets is formed, one near each peak of the laser electric field. This is the “first step” of the three-step-model.

The “second step”, that is to say the evolution of the electron wave packet under the influence of the oscillating laser field, is treated by using classical mechanics. For reasons of simplicity, we assume that the laser is a monochromatic light and we consider only its electric field:

$$\vec{F}(t) = F_0 \cos(\omega t) \vec{e}_x + \alpha F_0 \sin(\omega t) \vec{e}_y \quad (2.14).$$

Both the magnetic field of the laser and the electric field of the ion are ignored. The initial velocity at the time of ionization is taken as 0 and the initial position is supposed to be the position of the parent ion (also selected as position 0). Thus, by taking into account all the above assumptions, the electron motion after tunneling is described by the following differential equation:

$$\frac{d^2 \vec{r}}{dt^2} = - \frac{q_e}{m_e} \vec{F}(t) \quad (2.15),$$

the solution of which in cartesian coordinates, taking into account the initial conditions, gives the group of equations:

$$x(t) = x_0 [\cos(\omega t) - \cos(\omega t')] + \omega \sin(\omega t')(t-t') \quad (2.16),$$

$$y(t) = -\alpha x_0 [\sin(\omega t) - \sin(\omega t')] - \omega \cos(\omega t')(t-t') \quad (2.17),$$

$$v_x(t) = -v_0 [\sin(\omega t) - \sin(\omega t')] \quad (2.18),$$

$$v_y(t) = -\alpha v_0 [\cos(\omega t) - \cos(\omega t')] \quad (2.19),$$

where $\alpha = 0$ for linearly polarized light and $\alpha = \pm 1$ for circular polarization, $v_0 = q F_0 / m_e \omega$ and $x_0 = q F_0 / m_e \omega^2$. Let us take a numerical example. For light wavelength of 800 nm (typical for Ti-Sapphire laser systems) and intensity on target of $5 \cdot 10^{14}$ W/cm², $x_0 \sim 2$ nm. This value gives an idea about the distance from the parent ion reached by the electrons which at the end some of them will return to the core.

Here, we can already make a quick comment on the importance of the ellipticity of the driving field. As it can be immediately seen from equations (2.16) and (2.17), for circularly polarized light ($\alpha = \pm 1$) the electron never returns to the vicinity of the ion ($x = 0$ and $y = 0$ at the same time) and consequently the photon emission (“third step”) does not take place. The dependence of this photon emission on the ellipticity of the driving field is widely used in our days in “Atto-Science”. Particularly, consists the base for a numerous “gating” techniques, in which the change of the

ellipticity plays the role of a “switch” concerning the generation of the XUV radiation [see Chapter 5].

However, is not only the ellipticity which prevents electrons from returning back to the parent ion. Even with linearly polarized laser light ($\alpha = 0$), the probability of recombination of the electron with the parent ion depends on its time t' of ionization. As it can be seen from equation (2.16), electrons which are revealed during the temporal intervals: $\omega t' = \pi/2$ to $\omega t' = \pi$ and $\omega t' = 3\pi/2$ to $\omega t' = 2\pi$, will never return back to the ion. On the other hand, electrons revealed during: $\omega t' = 0$ to $\omega t' = \pi/2$ and $\omega t' = \pi$ to $\omega t' = 3\pi/2$, will return.

In the “third step” the electrons recombine with the parent emitting a photon, the energy of which is the sum of the kinetic energy gained during their travel away from the ion and of the ionization potential I_p of the atom. Thus, by using the equations (2.8) and (2.18), we obtain:

$$E_{ph} = I_p + \frac{1}{2} m v^2(t) = I_p + 2U_p [\sin(\omega t) - \sin(\omega t')]^2 \quad (2.20),$$

where I_p is the ionization potential of the atoms in target and U_p is the ponderomotive potential given in the equation (2.8). The energy E_{ph} depends only on t and t' . As the time t of the recombination depends only on t' [equation (2.16)], we conclude that the time t' predetermines the trajectory of the electron during its journey away from the parent ion. Predetermines also the energy of the emitted photon after recombination [see Figure 2-4].

By solving the equation (2.16) for $x(t) = 0$, one can obtain a simple analytical function^[37] which correlates one-to-one the recombination time t with the ionization time t' :

$$\frac{t}{T_L} = \frac{1}{4} - \frac{3}{2\pi} \sin^{-1} \left(4 \frac{t'}{T_L} - 1 \right) \quad (2.21),$$

where T_L is the period of the laser field. The graphic representation is shown in Figure 2-4(a).

As it is noted in the equation (2.20), the kinetic energy of the returning electron is an important parameter for the calculation of the harmonic spectrum predicted by this classical “three-step-model”. Using the equations (2.21), (2.18) and (2.8), one is able to obtain the dependence of the kinetic energy of the returning electron on its time of ionization t' [see Figure 2-4(b)], or the dependence on its time of recombination [see Figure 2-5]. The most valuable information provided by this simple model and its success, is based on the calculation of this kinetic energy.

The kinetic energy of the returning electron, as can be calculated from the equation (2.20) and shown in Figure 2-4(b), takes as a maximum value: $3.17 U_p$. So, depending linearly on the ponderomotive potential, imposes a maximum value on the photon energy emitted during the recombination:

$$E_{CutOff} = I_p + 3.17 U_p \quad (2.22).$$

This maximum value was immediately connected by Corkum with the highest order of efficient harmonic conversion $n_{CutOff} = E_{CutOff} / \hbar \omega$, i.e. with the already experimentally known abrupt “cut-off” of the High-order Harmonic Generation procedure. As it can be seen from equation (2.22), keeping in mind the expression for the U_p in (2.8), the position of the cut-off can be transposed to higher energy values either by increasing the ponderomotive potential U_p . This can be realized either by increasing the laser intensity, or by increasing the wavelength. The successful explanation of the cut-off law was one of the most notable successes of this model.

Another very important intrinsic mechanism of the HHG process, which was revealed by this semi-classical three-step-model, is the existence of two different classes of electron “trajectories”

which contribute to the generation of the harmonic spectrum. With just one glance on Figures 2-4(b) and 2-5, can be seen that for every value of kinetic energy corresponds to two different times of ionization and two different times of recombination. More specifically, one electron released at time $t'_{long} < 0.05 T_L$ returns to the parent ion with the same kinetic energy as the one revealed at time $t'_{short} > 0.05 T_L$. From (2.21) and Figure 2-6(a), one can realize that electrons released earlier in time will return later in time. We say that the electrons released before $0.05 T_L$ follow a “long” trajectory, while those which are released after $0.05 T_L$ follow a “short” trajectory.

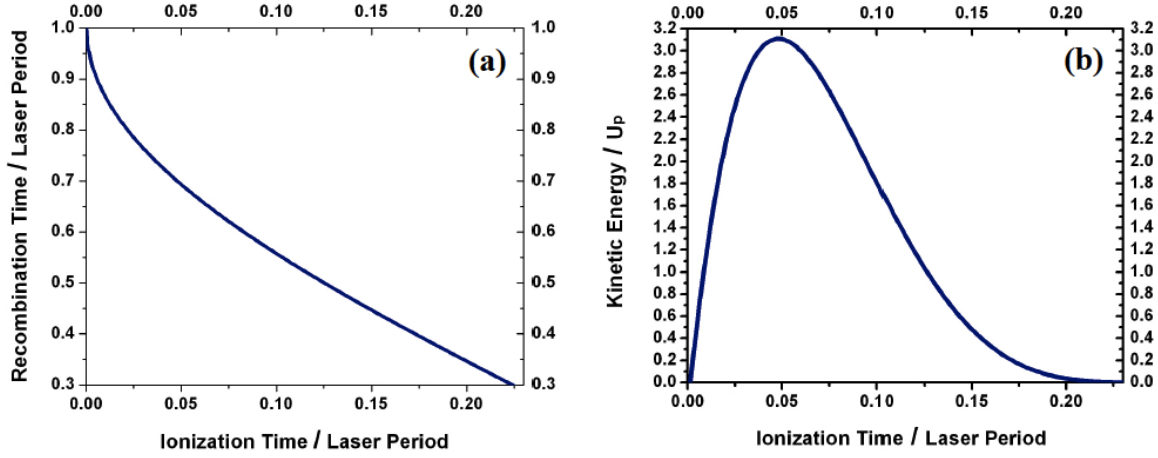


Figure 2-4 : (a) Dependence of the time of recombination t of an electron on its corresponding time of ionization t' (both are presented normalized by the laser period T_L). (b) The kinetic energy of a returning electron normalized by U_p as a function of its corresponding ionization time t' .

The importance of this dual contribution on the harmonic spectrum by “long” and “short” trajectories, first predicted by this simple semi-classical model, is enormous. For 20 years now, an unimaginable quantity of paper, ink and computing power has been consumed in order to be better understood the nature of these two classes of trajectories and their consequences on HHG. A big part of this Thesis is dedicated to such a study and, practically, for the rest of this chapter and for all along the following one, we will not stop on discussing about “short” and “long” trajectories.

For the moment let us examine a very characteristic and interesting feature of the HHG from “short” and “long” electron trajectories. Looking at Figure 2-5, it becomes clear that the energy of the emitted photon, at the recombination of the electron with the parent ion, depends on the time t of the recombination. This introduces a chirp $\propto dE_{ph}(t)/dt$ inside the bandwidth of each harmonic and between the constitutive harmonics (harmonic chirp). Figure 2-5 shows that this chirp is negative for the “long” trajectories and, contrarily, positive for the “short” ones. In both cases, seems to be almost linear over a broad photon energy range in the plateau spectral region.

Although in the HHG are always present contributions from both “short” and “long” trajectories, these contributions* are not equal. Electrons which travel in “long” trajectories, leave their atoms at ionization times t' closer to the peaks of the oscillating laser peak. Those which travel in “short” trajectories leave their atoms at later times, when the electric field gets smaller values. This difference influences the rate of ionization which results not to be the same for both cases. The

* Here we are not taking into account phase-matching effects from propagation inside the medium, which we will examine later in this Chapter.

“long” trajectories contribution is quite stronger than the “short” one, because there are more electrons which travel following “long” trajectories. This indirect prediction of the semi-classical three-step-model, very soon was experimentally verified^[38] and nowadays is considered as a common effect.

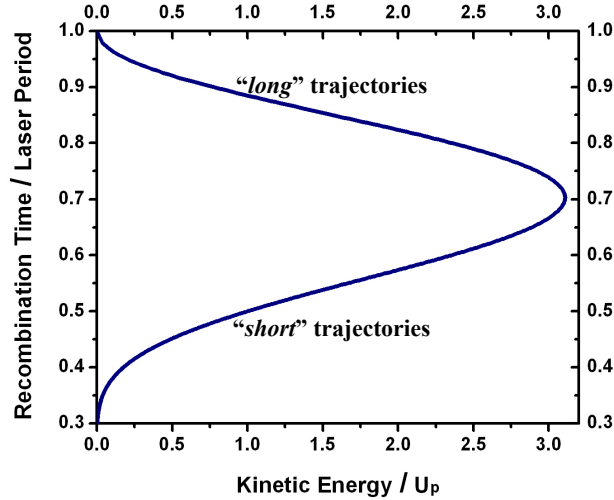


Figure 2-5: Graph of the kinetic energy of returning electrons (normalized by U_p) and of the corresponding recombination times (normalized by T_L) for each value. The branch above, with the negative slope, belongs to “long” trajectories. On the contrary, the branch below, with the positive slope, belongs to “short” trajectories.

The reader may be tortured by one bizarre question: The model has been presented in order to explain the high-order harmonic generation. But, up to now, where are the harmonics? The emitted spectrum shown in Figures 2-4(b) and 2-5 looks to be continuum. The answer is given by taking into account the $T/2$ periodicity of the process. The interference between spectra emitted successively every half-cycle, results in producing a spectrum which consists well confined odd harmonic frequencies as is shown in Figure 2-2.

Techniques are elaborated in order to modify the features of the generated spectrum by changing the periodicity of the “three-step”-procedure. If one imposes a periodicity of one cycle instead of half-cycle, then even-order harmonics will appear too^[39]. If, on the other hand, one restricts the periodicity of the procedure for only one or maximum two laser-cycles*, a large continuum spectrum will result. This is the main idea which triggered the development of the so-called Gating techniques [see Chapter 5].

2.2.2.2 The semi-classical three-step-model

The semi-classical version of the three-step-model, presented by Lewenstein et al.^[36], includes important quantum-mechanical effects such as quantum diffusion of wave packets and quantum interferences which are not included in the previous classical version. It allows us to get a better physical understanding of the harmonic generation in the tunneling limit. The model which is valid

* ...or, even better, if it is possible to cancel totally the periodicity by imposing on the “three-step”-procedure to take place only once. The feasibility of this idea starts to emerge slowly at the present time with the development of the very few-cycle femtosecond laser systems.

for harmonic photon energies higher than the ionization potential of the atom ($\hbar\omega > I_p$), is using the following three assumptions:

- (1) The contribution of all the bound states apart from the ground state $|0\rangle$ can be neglected.
- (2) The depletion of the ground state can be neglected (as the intensity of the driving field which provides the ponderomotive energy U_p is lower than the saturation intensity).
- (3) In the continuum, the electron can be treated as a “free” particle moving in the electric field with no effect of the atomic potential $V(\vec{r})$.

For an atom under the influence of the laser field $\vec{F}(t) = F \cdot \cos(t) \cdot \hat{e}_x$, of linear polarization in the x -direction, the Schrodinger equation using atomic units can be expressed as:

$$i \frac{\partial |\Psi(\vec{r}, t)\rangle}{\partial t} = \left[-\frac{1}{2} \nabla^2 + V(\vec{r}) - \vec{F} \cdot \vec{r} \right] |\Psi(\vec{r}, t)\rangle \quad (2.23).$$

After making the above three assumptions, the time-dependent wave functions can be expanded as:

$$|\Psi(t)\rangle = e^{iI_p t} \left(\alpha(t) |0\rangle + \int b(\vec{v}, t) |\vec{v}\rangle d^3 \vec{v} \right) \quad (2.24),$$

where $\alpha(t) \approx 1$ is the ground-state amplitude, and $b(\vec{v}, t)$ are the amplitudes of the corresponding continuum states $|\vec{v}\rangle$.

By substituting (2.24) to (2.23), one obtains the Schrodinger equation for $b(\vec{v}, t)$ which can be solved exactly and give:

$$b(\vec{v}, t) = i \int_0^t \vec{F} \cdot \vec{d}(\vec{v} + \vec{A}(t) - \vec{A}(t')) dt' * \exp \left[-i \int_{t'}^t \left[\frac{(\vec{v} + \vec{A}(t) - \vec{A}(t''))^2}{2} + I_p \right] dt'' \right] \quad (2.25),$$

$\vec{A}(t)$ being the vector potential which is related to the electric field \vec{F} via the formula:

$$\vec{F}(t) = - \frac{\partial \vec{A}(t)}{\partial t} \quad (2.26),$$

and $\vec{d}(\vec{v})$ the bound-free transition atomic dipole matrix element, which is a function of the momentum (in atomic units) \vec{v} . Explicitly: $\vec{d}(\vec{v}) \equiv \langle \vec{v} | \vec{r} | 0 \rangle$.

In order to calculate the time-dependent dipole moment, one needs to evaluate: $\vec{R}(t) = \langle \Psi(t) | \vec{r} | \Psi(t) \rangle$. By doing this and neglecting the contribution from the continuum-continuum transitions (only the transitions back to the ground state are considered), the final expression for the dipole moment of an atom in the time domain takes the form:

$$\vec{R}(t) = i \int_0^t dt' \int d^3 \vec{p} * \left[\vec{d}^*(\vec{p} - \vec{A}(t)) \right] * \left[\vec{F}(t') \cdot \vec{d}(\vec{p} - \vec{A}(t')) \right] * \exp[-iS(\vec{p}, t, t')] + c.c \quad (2.27),$$

where \vec{p} is the canonical momentum: $\vec{p} \equiv \vec{v} + \vec{A}(t)$ (2.28),

and S is the quasiclassical action that the electron acquires during its excursion in the laser field:

$$S(\vec{p}, t, t') = \int_{t'}^t dt'' \left(\frac{[\vec{p} - \vec{A}(t'')]^2}{2} + I_p \right) \quad (2.29).$$

A nice physical interpretation can be attributed to the equation (2.27). The term $\vec{F}(t') \cdot \vec{d}(\vec{p} - \vec{A}(t'))$ is the probability amplitude for the electron to make the transition from the ground state $|0\rangle$ to the continuum at time t' with the canonical momentum \vec{p} {Step 1}. The electronic wave function is then propagated until time t and acquires a phase factor equal to $\exp[-iS(\vec{p}, t, t')]$ {Step 2}. Finally, the electron recombines at time t with a probability amplitude equal to $\vec{d}^*(\vec{p} - \vec{A}(t))$ {Step 3}.

Equation (2.27) contains everything. The Fourier transform of $\vec{R}(t)$ provides the harmonic emission spectrum. Of course is not so easy to take it out. Nevertheless, during the procedure, one obtains a beautiful understanding of the physical process. This understanding and elucidation of the physical process, through the description of the calculation procedure, is the main goal of this introductory section. The extraction of the emitted harmonic spectrum and its comparison with the experimental results is out of the scope of this thesis. Such details can be found in the scientific literature, which is quite rich on this topic^[36,37,41,42].

The equation (2.27) inspired Lewenstein et al.^[36] to use the so-called Saddle-Point Method, introduced by Peter Debye^[43], in order to seek solutions with a very good approximation. The Saddle-Point Method is applicable here, because it is clear that the major contribution to the integral comes from the stationary points of the quasiclassical action $S(\vec{p}, t, t')$.

Let us start with the stationary points of the action $S(\vec{p}, t, t')$ in respect to \vec{p} . These points correspond to the quantum paths for which is valid the following equation:

$$\vec{\nabla}_{\vec{p}} S(\vec{p}, t, t') = 0 \Rightarrow \vec{p}_{st} = \frac{1}{(t-t')} \int_{t'}^t \vec{A}(u) du \quad (2.30)$$

since $\vec{\nabla}_{\vec{p}} S(\vec{p}, t, t') = \vec{r}(t) - \vec{r}(t')$, it can be concluded that the stationary points of the $S(\vec{p}, t, t')$ in respect to \vec{p} correspond to those canonical momenta for which the electron born at time t' returns to its “birth-position” at time t . This means that the dominant contribution to the harmonic emission comes from the electrons which, after their oscillation in the laser field, finally return to the parent ion. Here, is interesting to note that this was one of the basic assumptions made by Corkum et al.^[34] in the description of the semiclassical version of the model.

Using the Saddle-Point Method and taking into account the above stationary points, one can perform with a good approximation of the integral over \vec{p} in equation (2.27). This results in the following expression for the dipole moment:

$$\begin{aligned} \vec{R}(t) = & i \int_0^{+\infty} d\tau \left[\frac{\pi}{\varepsilon - i \cdot \tau/2} \right]^{3/2} * [\vec{d}^*(\vec{p}_{st} - \vec{A}(t))] * \\ & * [\vec{F}(t-\tau) \cdot \vec{d}(\vec{p}_{st} - \vec{A}(t-\tau))] * \exp[-i \cdot S(\vec{p}_{st}, t, \tau)] + c.c. \end{aligned} \quad (2.31),$$

where is introduced the so called return (or traveling) time $\tau \equiv t - t'$, as a new parameter, taking values from 0 to $+\infty$. The factor $[\pi/(\varepsilon - i \cdot \tau/2)]^{3/2}$ in the integral in (2.31), comes from the regularized Gaussian integration over \vec{p} around the saddle-point and expresses the effects of quantum diffusion*. This term makes the contributions from return times τ much larger than a laser

* According to the previous assumption (3), the effects of the atomic potential are assumed to be small between t' and t , so that S practically describes the motion of an electron “freely” moving in the laser field with a constant momentum \vec{p} .

* The spread of the electronic wave packet during the return time τ in the continuum.

cycle to be negligible.

In equation (2.31) the integral over τ can also be calculated using the Saddle-Point Method. As it can be seen from equation (2.29), substituting t' with $t - \tau$, the action S is stationary in respect to τ if:

$$\frac{\partial S(\vec{p}, t, \tau)}{\partial \tau} = 0 \Leftrightarrow \frac{[\vec{p} - \vec{A}(t - \tau)]^2}{2} + I_p = 0 \quad (2.32).$$

Here we can notice that if I_p were equal to zero [or if $U_p \gg I_p$ — as U_p is connected to the strength of the electric field expressed by \vec{A} in (2.32)], then the equation above states that the dominant contribution to the harmonic emission comes from electrons which leave the nucleus with an initial velocity equal to zero. This is another basic assumption of the classical version of the three-step model justified in the limit by this new quantum one. Nevertheless, in reality I_p is not equal to zero and so the condition imposed by (2.32) cannot be fulfilled for any real value of τ . In this case τ needs to be a complex number, the imaginary part of which can be interpreted as a tunneling time^[26].

There is a third “saddle-point equation” which can be obtain after the Fourier transform on $\vec{R}(t)$ given in equation (2.31):

$$\vec{R}(\Omega) = \int_{-\infty}^{+\infty} \vec{R}(t) \cdot e^{i\Omega t} dt \quad (2.33).$$

Here, Ω is a frequency which corresponds to any given photon energy $\hbar\Omega$. Via the Fourier transform given by the equation (2.33), the amplitude of the emitted field with frequency Ω can be found. The total emission spectrum (of the radiation emitted by one single recombination) is obtained by performing the integral in (2.33) for every frequency Ω . On the other hand, in order to obtain the harmonic emission spectrum one has to take into account the interference of emitted radiations from recombinations which happen within every half-cycle of the driving laser. In a similar way as the one we described in the discussion of the semiclassical version of the three-step-model [see paragraph 2.2.2.1].

In equation (2.33) [keep in mind the expression of $\vec{R}(t)$ from (2.31)], the exponential term contains also the term Ωt which comes from the Fourier transform. Consequently, the application of the Saddle-Point method in this case, in order to perform the integral over t , needs the stationary points for:

$$\Theta(\vec{p}, t, \tau) = \Omega t - S(\vec{p}, t, \tau) \quad (2.34).$$

From the equation (2.34), by substituting $t' \rightarrow t - \tau$, differentiating with respect to t and by taking into account the integral in the equation (2.29), it can be obtained that:

$$\frac{\partial \Theta}{\partial t} = 0 \Rightarrow \frac{\partial S}{\partial t} = \Omega \Rightarrow \frac{[\vec{p} - \vec{A}(t)]^2}{2} - \frac{[\vec{p} - \vec{A}(t - \tau)]^2}{2} = \Omega \quad (2.35).$$

According to the equation (2.32), So, the equation (2.35) can be rewritten in the form:

$$\frac{[\vec{p} - \vec{A}(t)]^2}{2} + I_p = \Omega \quad (2.36).$$

Equation (2.36) expresses simply the energy conservation law. Gives the final kinetic energy of the recombining electron that generates a photon with frequency Ω .

The combination of the three “saddle-point equations”, namely (2.36), (2.32) and (2.30), is very fruitful from the point of view of theoretical predictions. The Cut-off law can be obtained by finding the maximum value of the left part of the equation (2.36), taking into account the equations (2.32) and (2.30). The result is close to the one provided by the classical version of the model [see paragraph 2.2.2.1]. The small deviation from the result provided by the classical model is due to the quantum tunneling and quantum diffusion effects which were not taken into account in the frame of the previous classical model^[36].

$$E_{Cut\ Off} \approx 3.17U_p + 1.32I_p \quad (2.37).$$

Another very important result comes out when one tries to solve the equation (2.36) for a certain value $\Omega < \Omega_{max}$ (Ω_{max} is the photon energy at the Cut-Off). Using the equations (2.32) and (2.30), it can be found that there is always at least a pair of solutions for (t, τ) [i.e. $(t_1, \tau_1), (t_2, \tau_2)$] which satisfies the boundaries given by the the Saddle-Point equations. These solutions reflect the different trajectories that an electron can follow in the continuum. Depending on the time that an electron spends in the continuum, these trajectories are named “*Long*” and “*Short*”, in case that the traveling time of the “*long*” is longer than that of the “*short*” (i.e. $\tau_L > \tau_S$). This is also in fair agreement with the predictions of the classical model described in the paragraph 1.2.2.1.

In our days, twenty years after the publication on the quantum (semi-classical) three-step-model^[36], it is clear that the most important contribution of this model on the study of the High-order Harmonic Generation was the information provided on the phase of each component of the harmonic emission. Equation (2.27) shows that the phase of the induced atomic dipoles is determined by the value of the action acquired along the most relevant saddle-point trajectories. This quasiclassical action is given by equation (2.29) and, as it is shown by Lewenstein et al. in Ref [36], its stationary values are primarily determined by the ponderomotive energy U_p and the corresponding stationary return time τ_{st} .

$$S(p_{st}, \vec{t}_{st}, \tau_{st}) \approx U_p \cdot \tau_{st} + \dots \quad (2.38).$$

The ponderomotive energy, as we remember from equation (2.8), depends linearly on the intensity of the driving laser. So, equation (2.38) predicts that, in High-order Harmonic Generation, harmonics are not in phase with the driving laser. They exhibit phase shifts that depend strongly on the laser intensity.

These phase-shifts of the induced atomic dipole moments play a crucial role in the propagation of the driving field through the generating medium and have a major influence on the structure of the final outcome. Experimental evidence concerning the angular distributions of the emitted harmonic field or the strong dependence of the generated radiation on the focusing geometry^[38], could not have been interpreted properly without having taken into account these phase-shifts and examined them using the theoretical tools offered by the semi-classical three-step model.

In the work for this PhD Thesis, calculations based on the Lewenstein et al. 's semi-classical model^[36] have been performed and used in simulation processes [read chapter 3]. A computational solution of the model, provided by Emmanouil Skantzakis^[82], has been incorporated in the simulation computer algorithms which accompany the experimental results presented in this work.

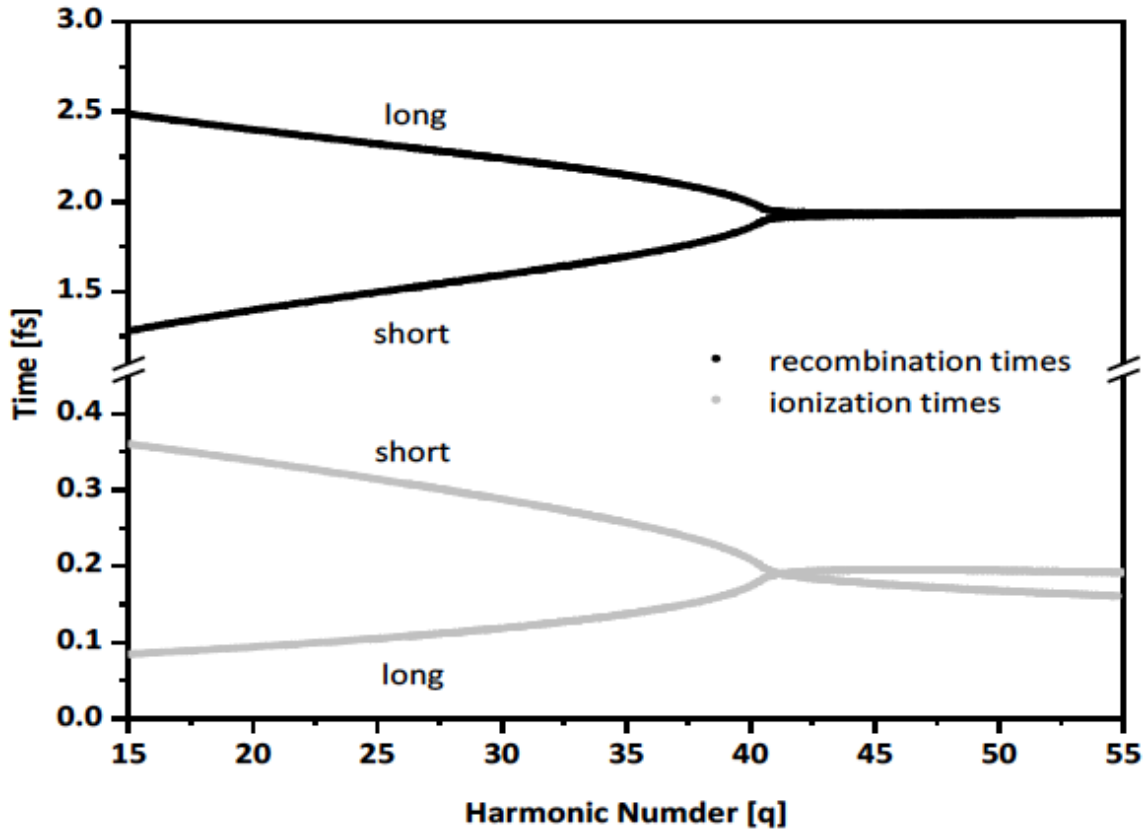


Figure 2-6: (Light Grey) Real part of the ionization times and (Black) recombination times for the “short” and “long” quantum paths, respectively. Parameters used in the calculations: laser central wavelength 800nm, pulse peak intensity $2.5 \cdot 10^{14} \text{W/cm}^2$, Xenon. [Figure and caption reprinted from “Emmanouil Skantzakis' PhD Thesis, University of Crete (2011)”^[82]].

The system of the three Saddle-Point equations consists of the equations (2.30), (2.32) and (2.36) with the same set of variables (Ω, t, τ) . Within each cycle of the driving field, the system is solved and all the possible triplets (Ω, t, τ) are obtained. This means that to every single component of the generated radiation of frequency Ω , the algorithm reveals all the possible electron recombination t and return τ times [see Figure 2-6 where instead of the return time variable τ , E. Skantzakis preferred to use the ionization time variable $t' = t - \tau$]. The amplitude for each spectral component is given by the emission rate^[82]:

$$W(\Omega) = \Omega^3 |\vec{\mathcal{R}}(\Omega)|^2 \quad (2.39),$$

calculating the Fourier component $\vec{\mathcal{R}}(\Omega)$ of the dipole moment from the equations (2.33) and (2.31). By adding the spectra (taking into account the amplitude and the relative phase of each spectral component) of the generated radiation from every single cycle of the driving field, results the total outcome of the computer simulated generation process.

2.3 Phase-matching conditions for high-order harmonics

2.3.1 The role of field-gradient forces

According to the discussion in the previous paragraph, the phase of each component of the harmonic radiation results from the phase acquired by the electron wave function in the continuum and from the phase due to the time delay between the recombination time t and the reference time of the laser period.

$$\Phi_{at} = q\omega t - \frac{1}{\hbar} S(p_{st}, t, \tau) \quad (2.40).$$

In (2.40) ω stands for the laser angular frequency, q for the harmonic order, p_{st} is the stationary action value of the canonical momentum and S is the semiclassical action along the stationary action trajectory considered.

Now, if one examines the spatial gradient of Φ_{at} , a useful tool for the profound understanding of the phase-matching in strong laser fields will emerge. Is the, so-called, effective wave vector \vec{K} which is introduced by P. Balcou et al.^[44] as the gradient of the atomic phase expressed in the equation (2.40). Namely:

$$\vec{K} \equiv \vec{\nabla} \Phi_{at}(\vec{r}) \quad (2.41),$$

which, from the equation (2.40), results to:

$$\hbar \vec{K} = -\vec{\nabla} S(\vec{r}, t, \tau) \quad (2.42).$$

The great importance of \vec{K} will be completely understood in the next paragraph (2.3.2) where we will discuss in detail about the generalized phase-matching conditions inside the generating medium. In this paragraph we will focus on what happens to the harmonic radiation which is emitted from one and a single atom. But, what does it represent the spatial gradient of the action? Action and angular momentum have the same dimensions. Consequently, $\hbar \vec{K}$ represents a physical quantity with the dimensions of momentum. In what follows we will examine what is really the meaning of this quantity.

Let us consider an atom being at the position \vec{r}_0 and let us first examine the dependence of the semiclassical action S on the atom position. Using the definition of S provided by (2.29), we obtain:

$$\begin{aligned} \hbar \vec{K}(\vec{r}_0) &= -\vec{\nabla} S(\vec{r}_0, t) = \\ &= -\int_{t-\tau}^t \left[\vec{\nabla} \cdot \vec{p}_{st}(\vec{r}_0, t') - \vec{\nabla} \cdot \vec{A}(\vec{r}_0, t') \right] \cdot \left[\vec{p}_{st}(\vec{r}_0, t') - \vec{A}(\vec{r}_0, t') \right] dt' \end{aligned} \quad (2.43).$$

In writing (2.43) we have made a few approximations which can be well justified. In reality, the ionization and recombination times, $t-\tau$ and t , depend on the electric field amplitude. However, in Ref [41] is shown that they can be considered as almost constant. Also, the spatial derivatives of \vec{A} are taken at the atom position \vec{r}_0 as the typical electron excursion with respect to the atom is much smaller than the scale of variation of the laser intensity.

Now, if we take into account that $\left(\vec{\nabla} \cdot \vec{p}_{st}(x_0) \right) \int_{t-\tau}^t \vec{v}(t') dt' = 0$, since the initial point coincides with the final point of the trajectory [remember the 3-step-model in section 2.2.2], and also that:

$$\begin{aligned}
\frac{d\vec{p}}{dt} &= \frac{d\vec{v}}{dt} + \frac{d\vec{A}}{dt} \Rightarrow \\
\Rightarrow \frac{d\vec{p}}{dt} &= -\frac{\partial\vec{A}(\vec{r}_0, t)}{\partial t} + (\vec{\nabla} \cdot \vec{A}) \vec{v} + \frac{\partial\vec{A}(\vec{r}_0, t)}{\partial t} \Rightarrow \\
&\Rightarrow \frac{d\vec{p}}{dt} = (\vec{\nabla} \cdot \vec{A})(\vec{p} - \vec{A})
\end{aligned} \tag{2.44}$$

then the expression in (2.44) gives:

$$\hbar \vec{K} = \int_{t-\tau}^t \frac{d\vec{p}}{dt} dt' = \vec{p}(t) - \vec{p}(t-\tau) \tag{2.45}$$

Equation (2.45) says that the momentum $\hbar \cdot \vec{K}$, which results from the gradient of the action S on the atom position, is nothing more than the canonical momentum gained by the electron in the continuum. Of course this gain is possible only if we consider the electric field, “seen” by the electron during its excursion, as slightly inhomogeneous (otherwise $\vec{\nabla} \cdot \vec{A} = 0$ everywhere) in order to be able to produce the so-called field-gradient forces which change the canonical momentum \vec{p} during the return time τ . From equation (2.38) we know that the dominant contribution to S is $U_p \cdot \tau_{st}$. Thus, we can write (2.44) also in the form:

$$\delta\vec{P}_{elec} \equiv \hbar \vec{K} = -\left[\vec{\nabla} U_p(\vec{r}_0)\right] \cdot \tau_{st} = \vec{p}(t) - \vec{p}(t-\tau) \tag{2.46}$$

Momentum and energy are left as an inheritance from the recombining electrons to the harmonic photons. Thus, the very important conclusion which came out from all this reasoning is that the momentum of an harmonic photon is not solely due to the sum of momenta of the incident laser photons. It is due also to this excess momentum $\delta\vec{P}_{elec}$ borrowed by the laser beam to the ionizing electron. That is to say:

$$\hbar \vec{k}_q = q \hbar \vec{k}_1 + \delta\vec{P}_{elec} \tag{2.47}$$

where q is the harmonic order and $\hbar \vec{k}_1$ the momentum of the driving laser photons.

Since $|\hbar \vec{k}_q| = |q \hbar \vec{k}_1|$, one realises that $\delta\vec{P}_{elec}$ offers some angular deviation to $\hbar \vec{k}_q$ with respect to $\hbar \vec{k}_1^*$. This deviation, examined here in the single atom level, plays a very important role in forming the very interesting angular distribution of the harmonic radiation generated by the driving field in a generating medium. This will be the subject of the following section. However, before leaving the single atom level, is very important to note that $\delta\vec{P}_{elec}$ is expected vary between the “Short” and the “Long” trajectories. Specifically, since the “Long” electron trajectories are longer than the “Short” ones, the canonical momentum in the first case tends to be more sensitive to the inhomogeneities of the driving field. Thus, the deviation caused by $\delta\vec{P}_{elec}$ tends to be bigger for the harmonics which come from “Long” trajectories than the ones which come from the “Short”. This tendency in the atomic level leads to distinct angular distributions, between the “Long” and “Short” contributions, in the macroscopic level. That is to say, when propagation through a generating medium takes place.

* Note that in perturbative low-order harmonic generation, where the harmonic dipole moment does not exhibit any intrinsic phase, $\hbar \vec{k}_q = q \hbar \vec{k}_1$.

2.3.2 Generalized phase-matching conditions for high-order harmonics

In order to provide a complete theoretical description of the harmonic generation process, one needs to divide his work into two parts:

- To calculate the single atom emission spectrum.
- To take into account the propagation of the generated harmonic field in the nonlinear medium. Here, has to be taken into consideration the integral on the interaction volume of the harmonic field generated at each point \vec{r} in space and time^[137].

$$E_q(\vec{r}') = \left(\frac{q\omega}{c}\right)^2 \int \frac{\exp[ik_q|\vec{r}-\vec{r}'|]}{|\vec{r}-\vec{r}'|} P_q(\vec{r}) d^3r \quad (2.48),$$

Up to this point, we have discussed a lot about the first part, the single atom response, and we sketched out the procedure that the calculation has to follow. We showed how it is possible to calculate the amplitude and the phase of the atomic dipole moment for each harmonic frequency [see section 2.2.2.2]. In order to deal with the second part now, one has to solve the propagation equations inside the generating medium using these dipole moments as source terms at each point in space.

In high-order harmonic generation (HHG) the spatial and temporal coherence properties of the incident laser, in high-order case, are not transmitted to the generated fields, like it happens in the “perturbative” case. This is due to the fact that the dipole moment d_q at the q_{th} -harmonic frequency, in HHG, does not vary simply as the q_{th} -power of the incident electric field. The dipole moment in HHG, as already shown in section 2.2.2.2, is a complicated function of the laser electric field. Depends on whether the harmonic belongs on the plateau or the cut-off of the harmonic spectrum. Also, in case that it belongs on the plateau, depends on whether it is produced from an electron recombination after traveling along a “Long” trajectory or a “Short” one. If one takes also into account that the intensity and the direction of the driving field (usually produced by a focusing laser beam) usually varies throughout the generating medium, the problem on introducing propagation effects in HHG starts to reveal its complexity. Nevertheless, the problem has to be faced since there is no other way to interpret the numerous experimental results on the angular distributions of the HHG radiation in rare gases^[38,45,46,47].

In the following section the harmonic phase matching conditions and their influence in the properties of the outgoing from the medium harmonic radiation is going to be discussed. The approach which will be followed has been suggested by Balcou^[44] and consists the modification of the traditional phase-matching conditions by incorporating in them the gradient of the intensity dependent phase of the atomic dipole moments.

In a region of space where the harmonic radiation is generated, optimal phase matching for the q_{th} -order harmonic will be obtained in direction \vec{k}_q , if at any two points \vec{r}_1 and \vec{r}_2 in this direction the harmonic field generated interfere constructively^[44]:

$$\arg\left[P_q(\vec{r}_1)\exp(i\vec{k}_q\cdot(\vec{r}_2-\vec{r}_1))\right] = \arg\left[P_q(\vec{r}_2)\right] \quad (2.49),$$

P_q being the q_{th} -Fourier component of the atomic polarization in the medium. It is proportional to the atomic density and the corresponding Fourier component of the atomic dipole moment provided by the 3-step-model in equation (2.33).

The infinitesimal version of the equation (2.49), i.e. for \vec{r}_1 and \vec{r}_2 close enough, becomes:

$$\vec{k}_q = \vec{\nabla}\arg(P_q) \quad (2.50).$$

For harmonics generated in a perturbative regime from a driving laser wave with plane wavefronts, the phase of the polarization is just q times the phase of the incident wave. Thus, the condition for the perfect phase matching is simply: $k_q = qk_1 \equiv q\omega/c$. However, in the case we examine here, there are two additional factors that need to be taken into account:

1. The phase induced by the focusing of the generating (let us suppose Gaussian) beam. This is the so-called Gouy phase which in cylindrical coordinates can be expressed as^[48]:

$$\Phi_{Gouy}(r, z) = \arg \left[\frac{1}{b + 2iz} \exp \left(-\frac{k_1 r^2}{b + 2iz} \right) \right] \quad (2.51),$$

b being the confocal parameter and $(r, z) = (0, 0)$ being associated to the “geometrical” focal point.

2. The intensity-dependent part of the atomic phase Φ_{at} [see equation (2.40)], discussed already in detail in sections 2.2.2.2 and 2.3.1.

The total wave vector \vec{k}_1 , which is not any more space independent, can be expressed as:

$$\vec{k}_1(r, z) = k_1 \vec{e}_z + \vec{\nabla} \arg \left[\frac{1}{b + 2iz} \exp \left(-\frac{k_1 r^2}{b + 2iz} \right) \right] \quad (2.52),$$

where \vec{e}_z is the unit vector in the z direction.

On the other hand, the spatial dependence of the atomic phase Φ_{at} can be characterized by means of the effective wave vector \vec{K} , already introduced in section 2.3.1:

$$\vec{K}(r, z) = \vec{\nabla} \Phi_{at}(r, z) \quad (2.41).$$

So, considering the equations (2.51) and (2.41), one can rewrite the equation (2.50) in the form:

$$\vec{k}_q = q \vec{k}_1 + \vec{K} \quad (2.52).$$

According to the equation (2.41) and because of the dependence of the Φ_{at} on the driving field intensity [see equations (2.40) and (2.38)], $\vec{K}(r, z)$ obtains a star-like form around the focal point ($r = 0$ and $z = 0$), which is the point of maximum intensity. Everywhere, $\vec{K}(r, z)$ points at a direction away from the focal point [see Figure 2-7(a)]. On the other hand, $\vec{k}_1(r, z)$, as it describes a focusing gaussian beam, is mostly directed along the z -direction. It converges for $z < 0$ and diverges for $z > 0$ [see Figure 2-7(b)]. Consequently, the addition of these vector fields, $\vec{k}_1(r, z) + \vec{K}(r, z)$, with so different distributions to each other, results in a complicated and asymmetric sum. Asymmetric between the parts before ($z < 0$) and after ($z > 0$) the focus.

Now it will be examined how the optimal phase matching depends also on the type of the trajectory (“*Long*” or “*Short*”) followed by the electron before its recombination. As already mentioned, the intrinsic atomic phase Φ_{at} depends on the trajectories and the “*Long*” contribution in it is, in the “plateau” part of the spectrum, different from the “*Short*” one. This means that the equation (2.41), in which is defined the effective wave vector \vec{K} , has to be splitted in two parts. Namely:

$$\vec{K}_{short}(r, z) = \vec{\nabla} \Phi_{at}^S(r, z) \quad \text{and:} \quad \vec{K}_{long}(r, z) = \vec{\nabla} \Phi_{at}^L(r, z) \quad (2.53).$$

At the points of the generating medium where the intensity of the driving field imposes on the specific harmonic q to stand in the “cutoff” region of the spectrum, the above two distinct vector functions coincide with each other. However, everywhere else in the medium (the generated harmonic q standing on the “plateau”), $\vec{K}_{long}(r, z)$ and $\vec{K}_{short}(r, z)$ are different to each other.

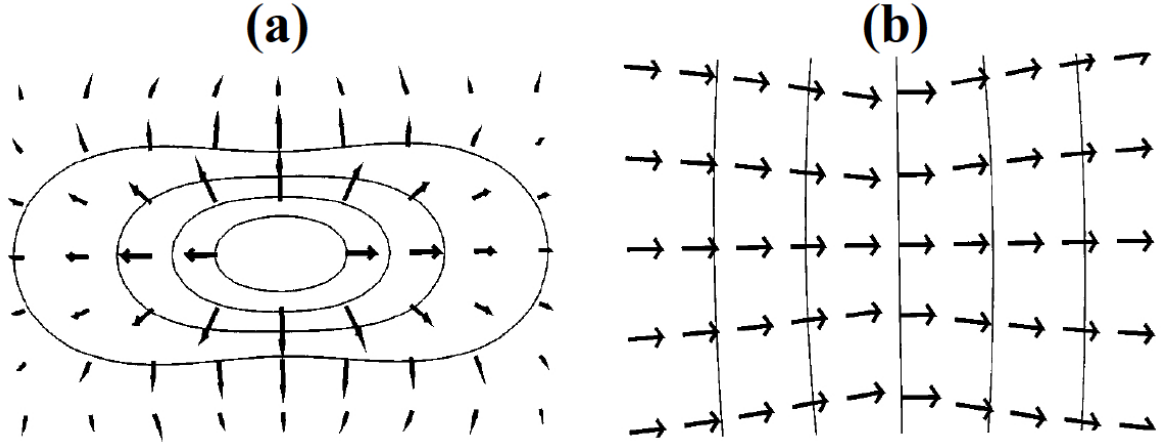


Figure 2-7: (a) Distribution of the effective wave-vector \vec{K} in the focal region. (b) Distribution of the generating field wave-vector \vec{k}_1 .

The most characteristic difference between $\vec{K}_{short}(r, z)$ and $\vec{K}_{long}(r, z)$ is that, for reasons explained in the section 2.3.1, the transverse components of the vectors in $\vec{K}_{long}(r, z)$ tend to be bigger than those in $\vec{K}_{short}(r, z)$. This feature is crucial for the optimum phase-matching conditions and leads to notable differences in the angular distribution between the “Long” and the “Short” contributions in the total harmonic radiation.

Let us first consider what is happening close to the focusing axis ($r = 0$), or close to it. For points located on the axis and after the focus ($z > 0$) the “Short” effective wave-vector \vec{K}_{short} presents a big component parallel to the axis and compensates for the focusing phase mismatch. In other words, in the on the axis and after the focus ($z > 0$) case, \vec{K}_{short} makes the difference between \vec{k}_q and $q\vec{k}_1$ to be small. As a result, the collinear phase-matching in this spatial region becomes efficient for the “Short” harmonics* [see Figure 2-8(a)]. Conversely, for points located on axis but before the focus ($z < 0$), the effective wave-vectors \vec{K}_{short} and \vec{K}_{long} make things worse with the phase-matching [see Figure 2-8(c)]. As a consequence, the harmonic generation is very inefficient in the region close to the axis and before the focus ($z < 0$). Inefficiency of the harmonic generation is also realized at points close to the focus ($r = 0$ and $z = 0$). There, the effective wave-vectors are almost zero [see Figure 2-8(b)], as the intensity gradient is almost zero, and again the phase-matching conditions are not fulfilled.

Nevertheless, in the area before the focus ($z < 0$) there are points off-axis ($r > 0$) for which noncollinear phase-matching is achieved [see Figure 2-8(d)] due to the transverse component of the \vec{K}_{long} . These points will form a large ring around the laser axis yielding an annular structure to the emitted harmonic field. So, this case is favorable to harmonic emission dominated by “Long” trajectories contribution. In this region ($z < 0$, $r > 0$) of the generation, it is very interesting also to

* Also for the “cutoff” ones.

notice the transverse components of \vec{k}_q and $q\vec{k}_1$ are opposite to each other. As a consequence, even if the driving laser field is convergent, the generated harmonic field results to be divergent.

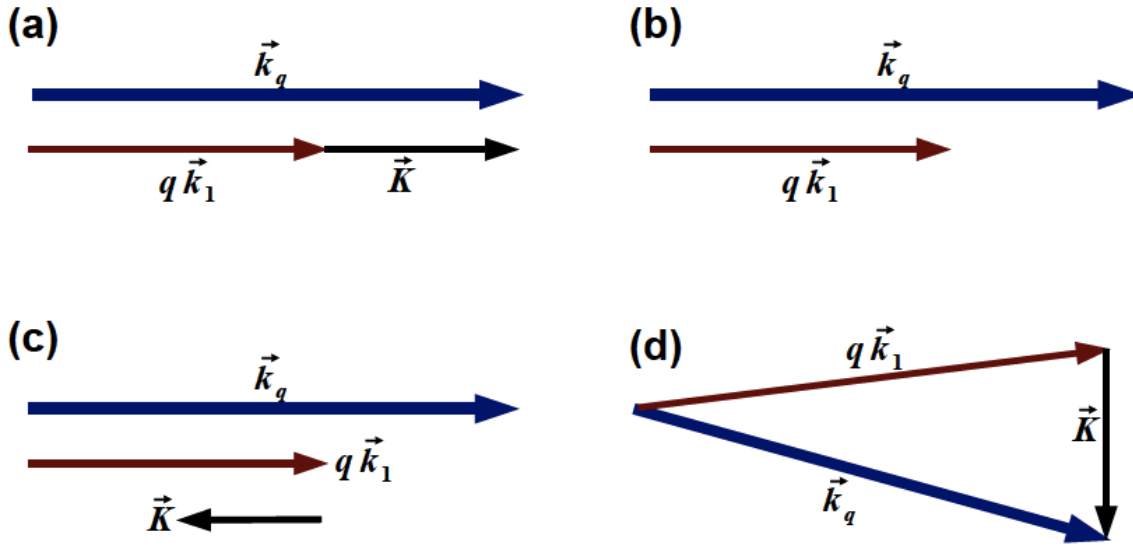


Figure 2-8: (a) Example of phase-matching diagram at a point located on axis ($r = 0$) after the focus ($z > 0$). Collinear phase-matching is efficient, mainly for the “Short” or the “Cutoff” harmonics. (b) Example of phase-matching diagram at the focus ($r = 0$ and $z = 0$). The effective wave-vectors \vec{K}_{short} and \vec{K}_{long} are zero, as the intensity of the driving field there takes the maximum value. Phase-matching is inefficient. (c) Example of phase-matching diagram at a point located on axis ($r = 0$) before the focus ($z < 0$). Collinear phase-matching is very inefficient. (d) Example of phase-matching diagram at a point located off-axis ($r > 0$) and before the focus ($z < 0$). Non-collinear phase-matching can be achieved, mainly for the “Long” harmonics.

The previous just presented makes clear the great importance of the focusing geometry during the process of the high-order harmonic generation. As it is shown, many important features of the generated radiation (like the total energy, the angular distributions, the spatial and spectral coherence^[49], the phase difference in comparison to the driving field) depend on the relative position between the generating medium and the focus, in combination with the confocal parameter of the focusing fundamental beam. The possibility to tune main features of the generated harmonic radiation by selecting, in each case, the proper focusing geometry, has been a lot appreciated since mid-late 1990s. Numerous techniques have been based on it, like the ones which use the phase-matching conditions offered by the focusing geometry in order to select one^[50] between the two contributions, from “Long” trajectories or “Short”.

Before closing this section, we would like to refer to the first experiment^[51] which demonstrates, in a simple way, the above mentioned theoretical predictions. In this experiment, Bellini et al., imitating the famous Young's “two-slit experiment”, produced the interference pattern in the far field by generating two separated harmonic sources. In accordance to what is mentioned before about the importance of the focusing geometry, we have to note here* that, during Bellini 's et al.

* Even if Bellini et al. do not state it clearly in their published article^[51], although it can be extracted from the informations given about the focal length used and by making an assumption about the aperture of their gas jet.

experiment, the generating medium seems that was covering an area extended before and after the focus. The length of this area of generation was much bigger than the confocal parameter. As a consequence, all the possible phase-matching schemes discussed before [see Figure 2-8] used to take place at the same time.

What Bellini et al. discovered was an interference pattern exhibiting two clearly distinct regions [see Figure 2-9]. Namely:

- (i) an intense inner one, where the “*Short*” contribution seems to prevail,
- (ii) an extended outer one (containing about 80% of the total energy) which seems that hosts mainly harmonics generated from “*Long*” trajectories.

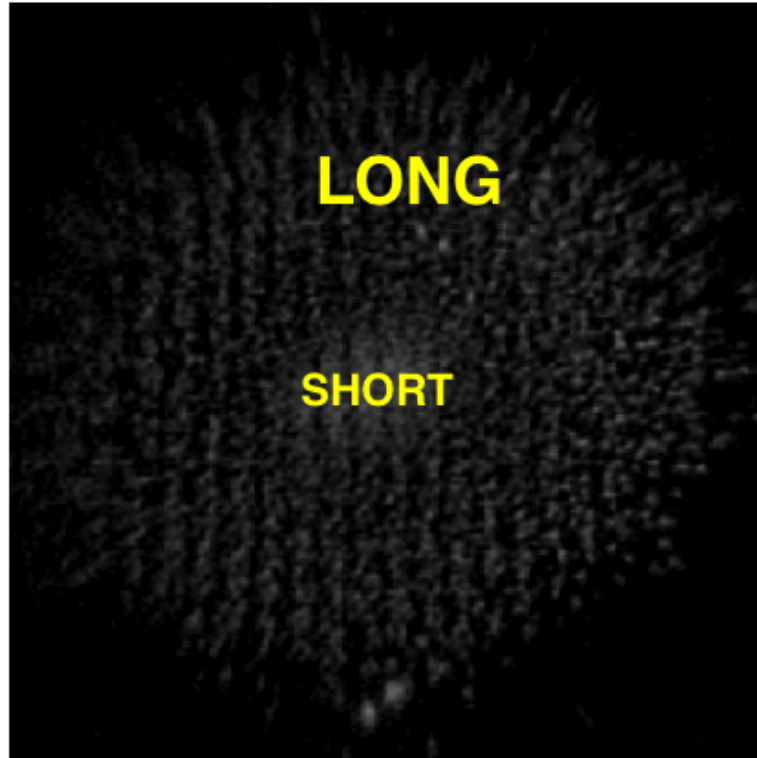


Figure 2-9: XUV beam profile showing the different divergence between the shot and long trajectories. The interference fringes shown on the profiles have been used in order to measure the coherence times of the long and short trajectories. More detail description of the experiment can be found in the Reference [51].

Bellini 's et al.^[51] work depicts experimentally in an ideal way a lot of important conclusions from the theoretical description we have been providing all along this Chapter.

2.3.3 Dispersion

Up to this point we have not written any single word about the impact of the dispersion on the propagation of both the fundamental and the harmonic field through the generating medium. We preferred first to focus on the interplay between the two parameters (i.e. the Gouy phase shift and the, intensity dependent, atomic dipole moment phases) which are mainly responsible for the

characteristic structure of the profile exhibited by the generated harmonic radiation. Nevertheless, for one who desires to offer the least description of the procedure of high-order harmonic generation (HHG), it is unthinkable not to mention the dispersion effects which take place.

Dispersion of both the neutral and of the ionized medium has to be taken into account^[52]. However, the dispersion of the ionized medium (i.e. plasma) results to be the dominant one in most cases where even a small fraction of atoms is ionized in the generating medium. Thus, for most of the high-order harmonic generation experiments, plasma dispersion has to be carefully considered.

If the laser intensity is high enough to ionize the generating medium, plasma is formed in the focal volume and presents a refractive index which depends on the radiation frequency as:

$$n_p(\omega) = \sqrt{1 - \left(\frac{\omega_p}{\omega}\right)^2} \quad (2.54),$$

where ω_p is the so-called *plasma frequency** and is given by^[52]:

$$\omega_p^2 = \frac{e^2 N_e}{m_e \epsilon_0} \approx 3.18 \cdot 10^9 N_e \quad (2.55),$$

where m_e is the electron mass, e the electron charge and N_e is the electron density. In the case of HHG, because of the relatively low gas densities used, $\omega_p \ll \omega$. As a result, equation (2.54) can obtain the following simpler form:

$$n_p(\omega) \approx 1 - \frac{\omega_p^2}{2\omega^2} < 1 \quad (2.56),$$

Incorporating into the phase-matching theory presented in Section 2.3.2 the phase-mismatching between the fundamental and its generated harmonics, due to their propagation through the medium with different velocities, is not at all an easy work. Too much complication comes from the fact that harmonics which are generated at a certain point of the medium do not necessarily propagate collinearly with their generating field [see Section 2.3.2]. The full treatment of this topic exceeds by far the goals of the present introductory chapter. Nevertheless, in order to sketch out the procedure and to present a few very interesting and useful results, we will be restricted here to discuss a rather simplified hypothesis of collinear propagation between the fundamental and its q -order harmonic. As mentioned in Section 2.3.2 this collinear co-propagation of the two, is close to what really happens at points of the medium located not far from the axis ($r \sim 0$) and after the focus ($z > 0$). Remember that the harmonic generation there comes out to be efficient mainly for the “*Short*” or the “*Cutoff*” harmonics [see Figure 2-8(a)].

In this case of collinear propagation, the phase lag between the q -order harmonic field E_q and the q -order polarization P_q driven by the fundamental at a certain axial point z (its distance from the focus), can be expressed as^[52]:

$$\begin{aligned} \Delta\varphi(z) &\equiv \varphi(E_q) - \varphi(P_q) = \varphi(E_q) - q \cdot \varphi(E_1) \Rightarrow \\ \Delta\varphi(z) &= [k_q z - \arctan(2z/b)] - [q k_1 z - q \cdot \arctan(2z/b)] \end{aligned} \quad (2.57),$$

where k_1 and k_q are the wavenumbers at frequency ω and $q\omega$ correspondently, b is the confocal parameter of the IR focusing, and the “arctan”-terms are the Gouy phase shift considered, at point

* Plasma frequency expresses the resonance frequency for collective oscillations of the freed electrons, the much more massive ions being assumed as stationary.

z , for the fundamental and the q -order harmonic field*.

Perfect phase-matching would be perfect at points z where $\Delta\varphi(z) = 0$. According to the equation (2.57), this would necessitate: $[k_q z - \arctan(2z/b)] = [q k_1 z - q \cdot \arctan(2z/b)]$. Now, we can go on by using the approximation $\arctan(2z/b) \approx 2z/b$, which is valid when $2z/b$ small, and the equations: $k_1 = n_1 \omega / c$ and $k_q = n_q q \omega / c$. In this way, we conclude that:

$$\Delta\varphi(z) = 0 \Leftrightarrow n_q - n_1 = \frac{2c(1-q)}{q\omega b} < 0 \quad (2.58).$$

But, as is shown from equation (2.56), in typical high-order harmonic generation from gases (where, as told before, plasma dispersion is the prevailing), the difference $n_q - n_1$ cannot be but positive. Consequently, perfect phase-matching cannot take place. $\Delta\varphi(z)$ remains positive for every z in this region. This means that harmonics generated at consecutive axial points z close to the focus, will interfere constructively only for a finite distance inside the generating medium, the so-called *Coherence Length* (L_{coh}). Harmonic generation from a medium longer than L_{coh} will not result in a further enhancement of the generated field. In contrary, will lead to a certain reduction in the total number of “harmonic” photons.

* The reader may ask about what is going on with the intensity dependent phase-shifts of the induced atomic dipole moments. The answer is that for $z \ll b$, they remain almost constant as the intensity of the laser remains almost constant and as the “*Short*” and “*cutoff*” harmonics, which are favorable in this specific region, depend weakly on the intensity. Consequently, it can be omitted in good approximation from a phase-difference equation like the (2.57).

3rd Chapter

Revealing Quantum Path Details in high-field Physics

3.1. Introduction

The tunnelling of an electron through a suppressed atomic potential followed by its motion in the continuum and finally by its re-collision with the atomic core, is the fundamental mechanism underlying strong-field laser-atom interactions. Due to the quantum nature of the process, the properties of the electron wave-packet strongly correlate with those of the emitted radiation.

The two main contributions (from “*Long*” and “*Short*” electron trajectories) to the “*plateau*” part of the HHG spectrum emitted by a single atom, depend on the driving field intensity. They interfere to the total atomic polarization with different laser induced phases. These phases are related to the action accumulated along the orbit in each case and affect strongly the angular distributions of the emitted harmonic field [See Chapter 2]. Since 1996, Antoine et al.^[50] reported that is feasible the distinction between the parts, of the driven XUV radiation, which are due to different electronic trajectories (“*Long*” or “*Short*”). Needed only to take advantage of the fact that under certain geometrical conditions only one of these two contributions gets phase matched^[44,50].

In this work, information is extracted about the phase difference $\Delta\varphi(I_L)=\varphi_q^L(I_L)-\varphi_q^S(I_L)$ between the two parts of the XUV radiation which correspond to different electronic trajectories. Taking into consideration the profile of the generated XUV beam, on which appears a spatial separation between the two distinct contributions (“*Long*” or “*Short*”) [see Section 2.3.2], the main idea is to focus together the two parts and to take pictures of the focal area under conditions which assure the interference of the contributions. These pictures are taken for a long series of values of the intensity I_L of the driving pulse and consist the main tools we use in our study.

As will be shown in the following [see paragraph 3.4], the analysis made on this series of pictures offers us a direct measurement of the difference in harmonic emission times (Δt_e) and in electron quantum paths (ΔL_e) between the “*Long*” and “*Short*” trajectories. Although the harmonic generation mechanism has been extensively studied in the past^[36,51,54-58], is the first time that takes

place a measurement which reveals directly this kind of intricacies in the fundamental mechanism of the strong-field laser-atom interactions.

Only the use of a detector able to provide a detailed spatial resolution of the focal area could make feasible our project. The ion-imaging-detector (I-ID)^[59,60], which allows us to monitor the focal area by means of ions, generated on the way of the XUV beam through the detecting medium, is the most valuable instrument during this experiment.

3.2. The ion-imaging-detector

The limit of vision of the unaided human eye is about 0,1 mm. This limit was pushed downwards by a factor of 1000 (to about 1000 Angstroms) by 300 years of work on the optical microscopy. However, within the short time of a few decades, the electron microscope has been able to further extend this limit of human vision by another 1000 times. Starting as an unexpected child of high voltage cathode ray oscilloscope, the development of the apparatus has been very rapid. The basic principle of the instrument is to use electrons as the image-forming beam and symmetrical electrostatic or electromagnetic fields as lenses^[61] [see Figure 3-1].

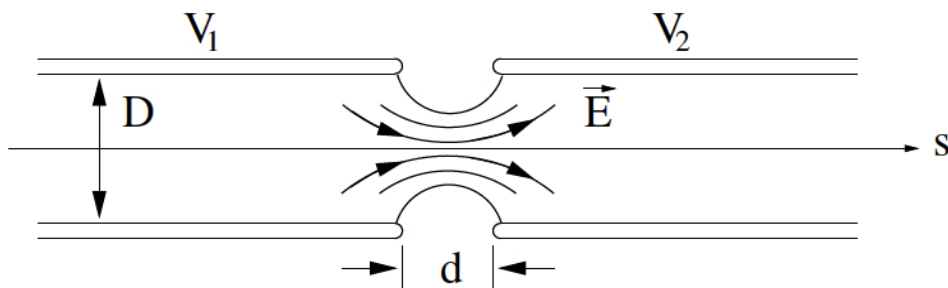


Figure 3-1 : Scheme of an accelerating tube lens^[74]. The voltages V_1 and V_2 denote the potential differences with respect to the ion source. The electric field acts at the entrance of the accelerating gap as a focusing lens and at the exit as a defocusing lens.

The history of the charge particle optics starts with the discovery of the cathode rays. Hittorf^[61], Goldstein^[62], Crookes^[63], Hertz^[64], Lenard^[65], Perrin^[66], Thomson^[67], and Wiechert^[68], during the last quarter of the nineteenth century, established the corpuscular nature of these rays and showed further that these could be concentrated by the use of long solenoids, producing axial magnetic fields. The electron microscope was a direct descendant of the high voltage cathode-ray oscilloscope. Busch^[69,70] was the first who developed basic theories about the lens action of symmetrical magnetic fields and may, therefore, be said to be the real founder of geometrical electron optics.

Shortly after Busch 's work on the focusing action of symmetrical magnetic and electrostatic fields, Davisson and Calbick in the U.S.A.^[71] and Bruche and Johannson in the A.E.G. laboratories in Berlin^[72] embarked on systematic investigations on electrostatic focusing devices. Davisson and Calbick showed theoretically that a hole in a charged plate would act as a lens so far as a charged particle beam was concerned [see Figure 3-2]. The development of electrostatic lenses and of electron microscopes using such lenses proceeded at first almost side by side.

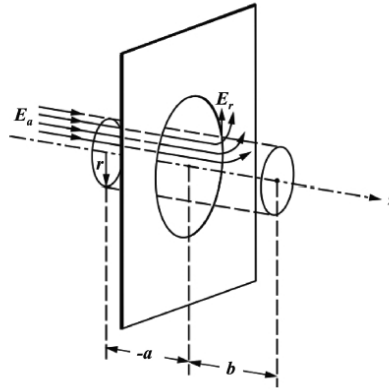


Figure 3-2 : Derivation of lens action of an aperture terminating an acceleration field.

The Ion-imaging-detector we use in this work, which is developed by Max-Planck-Institut für Quantenoptik* in collaboration with Stefan Kasdorf**, is a member of the big family of the charge-particle-Microscopy. A combination of electrostatic lenses of the type of Einzel^[74] provide magnification without modifying the energy of the charged particles [see Figure 3-3]. This feature gives the possibility to use the Ion-imaging-detector also as a mass spectrometer^[59].

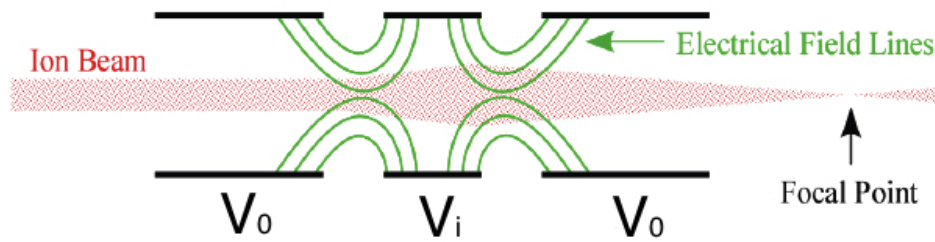


Figure 3-3 : The Einzel lens geometry. The outer cylinders are at potentials V_0 and the inner cylinder is at potential V_i . As an example, for $V_0 = -10V$ and $V_i = -100V$, are drawn with green colour the electrical field lines inside the lens and with red colour is drawn the shape of the beam of ions as passing through.

A schematic view of the device, is presented in the Figure 3-4. Ions generated in the laser focus are first accelerated by an electric field applied between repeller and extractor electrodes. The first electrostatic lens, images the spatial extent of the ion cloud into the ion microscope with a small magnification factor. This intermediate image is located in the focal plane of a second electrostatic lens, which projects a further magnified image onto the detector consisting of a pair of MCPs and a phosphor screen. The image of the ion cloud that appears on the phosphor screen is recorded by a CCD camera and represents a magnified orthogonal projection of the focal ion distribution under scrutiny.

* Max-Planck-Institut für Quantenoptik, Hans-Kopfermann-Strasse 1, D-85748 Garching, Germany

** Kaesdorf S Geräte für Forschung und Industrie, Gabelsbergerstr. 59 D-80333 München, Germany.

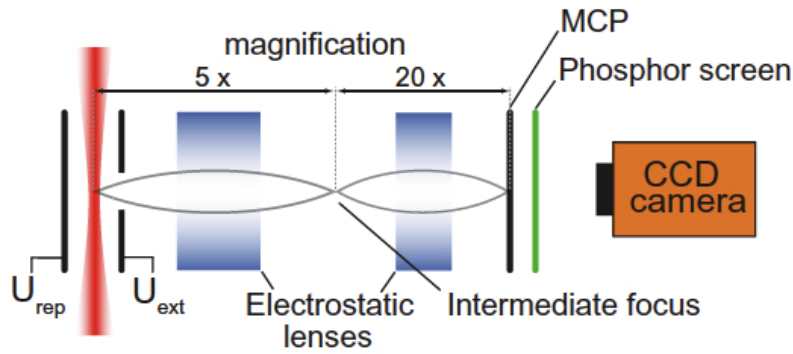


Figure 3-4 : Schematic view of the ion-imaging-detector^[59].

As it will become apparent in the following of this chapter, Ion Microscopy is a really powerful method to characterize focal geometries.

3.3. Experimental procedure

The experiment is performed by utilizing a 10 Hz repetition rate Ti:sapphire laser system delivering pulses of up to 170 mJ energy, $\tau_L = 33\text{fs}$ duration and wavelength at 800nm (IR). The experimental setup can be seen schematically in Figure 3-5.

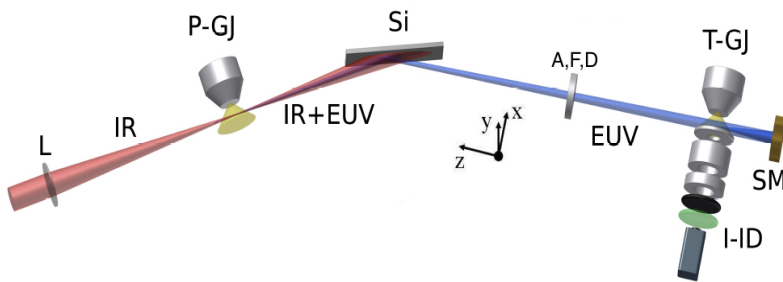


Figure 3-5 [Apparatus used for imaging of the EUV-phase-distribution] : Intense EUV radiation^[76, 77] is generated in Xenon gas by focusing, with a spherical lens (L) of 3m focal length, an 800nm centered 33 fs long laser pulse onto a Xenon gas jet (P-GJ). The EUV radiation is reflected towards the interaction region by a Silicon plate (SP) which has been used for the elimination of the IR beam. “F”, “A” and “D” are the filter, aperture and the calibrated EUV photodiode, respectively. The transmitted harmonics 11th, 13th and 15th are focused by an unprotected gold spherical mirror (SM), of focal length $f=5\text{ cm}$, onto a second gas jet with Argon or Helium as target gas (T-GJ). The images of the EUV focus are monitored by means of a high spatial resolution ion-imaging-detector (I-ID), the Ion-Microscope^[59].

An annular laser beam (formed using a super-Gaussian beam stop) with outer diameter of $\approx 2.5\text{ cm}$ and energy of $\approx 15\text{ mJ/pulse}$ is focused with an $f=3\text{m}$ lens onto a pulsed gas jet (P-GJ), filled with Xe. In our experiment, the generation of the harmonic radiation takes place with the focus of

the IR beam fixed up to the Xe gas jet. After the area where is generated the XUV radiation, a Si-plate is placed at Brewster's angle for the fundamental (75°). This Si-plate reflects the harmonics^[75] towards the detection area and in parallel reduces substantially the IR field. The residual outer part of the IR beam is blocked by a 5mm diameter aperture (A), which on the contrary lets the EUV radiation passing through.

Subsequently, the EUV beam is focused onto the target gas jet (T-GJ) by a spherical gold mirror (SM) of 5cm focal length. Great care has been taken in fixing the angle of incidence of the EUV beam on the gold mirror at zero degrees. The EUV images are monitored by means of a high spatial resolution ($1\mu\text{m}$) ion-imaging detector (I-ID), the Ion Microscope^[59], which records the spatial distribution of the ionization products resulted by the interaction of the EUV light with the target gas.

Additionally, the spectrum of the EUV radiation in the interaction area is determined by measuring the energy-resolved, single-photon ionization, photoelectron spectra of Ar gas. The electron spectra are recorded using a μ -metal shielded time-of-flight (TOF) ion/electron spectrometer, attached to a second EUV beam-line brunch, as it appears in the Figure 3-6. In order to have the same experimental conditions in both, the TOF and the I-ID set-ups, the branch of TOF, is constructed in an identical way as the one of the I-ID. This is done by using another Si-plate (mounted on a translation stage) placed also at Brewster's angle for the fundamental (75°). The length of the second branch, the metal filter, the aperture and the spherical gold mirror are the same as those in the I-ID branch. For the measurement of the photoelectron spectrum, in the interaction region of the second branch, the focused EUV beam is tilted by ≈ 1.5 deg with respect to the incoming beam. This is done in order to avoid measuring the photoelectrons generated by the incoming EUV beam.

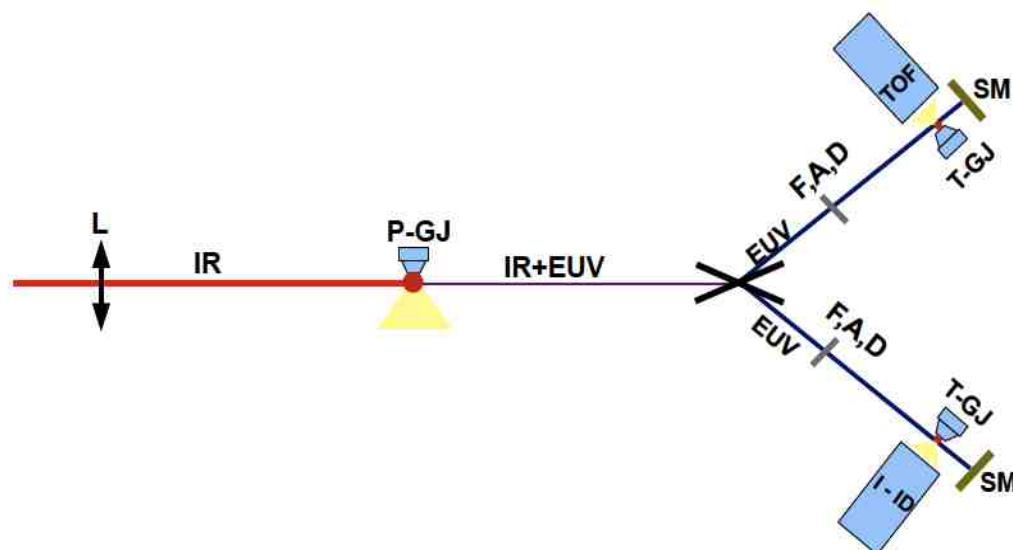


Figure 3-6 [Experimental set-up] : (L): Spherical lens which focuses the IR beam into the Xe gas jet (P-GJ). (SP): Silicon plate which reflects the EUV beam towards the interaction area. (F, A): Sn filter and Aperture used for the spectral and spatial filtering. (D): EUV-calibrated photodiode used for the measurement of the EUV energy. (SM): Unprotected spherical gold mirror which focuses the EUV beam into a second gas jet filled with the target gas (T-GJ). (I-ID): Ion-Imaging-Detector which monitors the EUV images. (TOF): Time of flight electron spectrometer used for the measurement of the EUV spectrum.

For the two-photon ionization images (see Figure 3-16), as well as for certain single-photon ionization images, an 150 nm thick Sn filter which transmits only the harmonics 11th, 13th and 15th is placed after the aperture. The amplitudes of the harmonics 11th, 13th and 15th in the interaction area are measured to be in arbitrary units 0.9, 1 and 0.7, respectively. Contrarily, in order to obtain the series of images showing the power dependence of the ion distribution from which is extracted the important structure presented in the Figure 3-9 and the Figure 3-17, the Sn filter is taken out of the EUV beam line. This way, any influence introduced by the filter on the properties of the EUV beam is avoided. With the filter removed, while all the generated harmonics are entering into the interaction area only the harmonics above the 11th can ionize the Ar gas by single-photon absorption.

Photoelectron spectra of the generated Harmonics, for various intensity values I_L of the driving field, are extracted by using the Time-Of-Flight spectrometer mounted on the first branch (as depicted in the Figure 3-6) of the Experimental Setup. The peak heights of the harmonics 11th, 13th and 15th, after the reflection on the spherical gold mirror, are shown in arbitrary units in the Figure 3-7. These experimental data, which reveal the dependence of the harmonic signal on the intensity I_L , have been used in order to determine the cut-off region of every single harmonic.

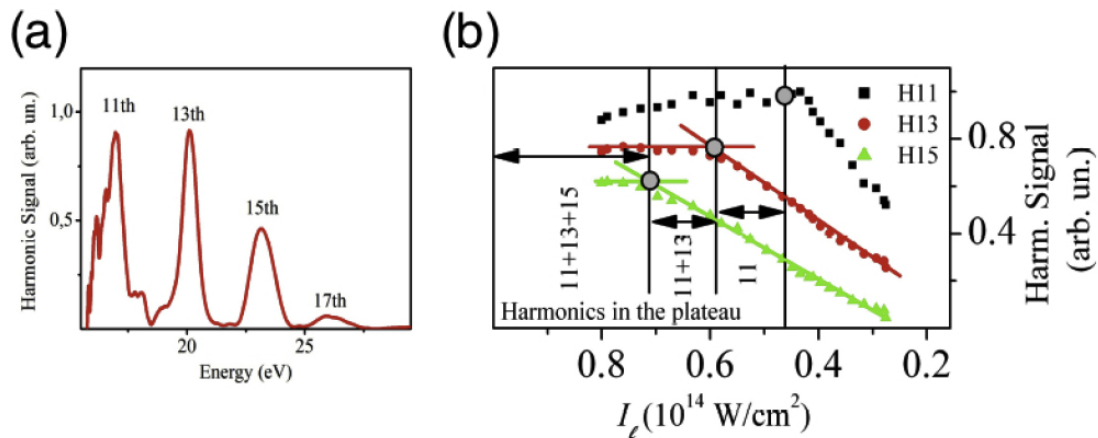


Figure 3-7 : (a) Harmonic spectrum recorded for $I_L \sim 7 \cdot 10^{13} \text{ W/cm}^2$. The harmonic signal has been recorded as a photoelectron spectrum by using a Time-Of-Flight spectrometer (TOF). (b) Dependence of the harmonic signal on I_L . The intensity I_L during the measurement started from values where all the harmonics are in the “plateau” region. The vertical black lines depict the cut-off intensity values for each one of the harmonics.

For the driving field intensity values that we use in this experiment, we find that the contribution of harmonics of order higher than 15 is not important in comparison to the contribution of the 11th, the 13th and the 15th. The 17th harmonic has been measured (for the maximum laser intensity values $I_L \sim 10^{14} \text{ W/cm}^2$) to be of an amplitude of one order of magnitude smaller than that of the 11th harmonic. All harmonics higher than the 17th are of even smaller amplitudes and thus give the right to neglect them. This is because, for the intensity values in discussion, they stand deep inside the “CutOff” region of the harmonics’ spectrum.

In order to measure the total energy of the EUV radiation we make use of an XUV calibrated photodiode which has been placed after the aperture (A) [See Figures 3-5 and 3-6]. This measurement on the total energy of the EUV radiation, combined with the photoelectron spectra extracted from the Time-Of-Flight spectrometer, can give information about the energy content

within each harmonic envelope.

The highest possible values of energy of the EUV radiation are used in order to obtain EUV-focusing images resulted by the 2-photon-ionization of He (see Figure 3-16). For this purpose, the EUV energy has been maximized and is found to be ~ 120 nJ in the interaction area. Taking into account this energy value, the measured focal spot diameter, and assuming the average EUV pulse duration to be ~ 15 fs, the intensity of the EUV pulse on target is estimated to be $\sim 5 \cdot 10^{14}$ W/cm².

3.4. Results & Discussion

As mentioned already (see section 3.1), the key point of the present study is the experimental observation of the interference pattern between the inner part of the XUV beam (which contains mainly radiation resulted by the “*Short*” electron trajectories) and the outer one (which mainly contains radiation resulted by the “*Long*” electron trajectories). This interference pattern depends on the phase difference between the two parts (between the outer and the inner part) $\Delta\varphi(I_L) = \varphi_q^L(I_L) - \varphi_q^S(I_L)$, for any given intensity I_L of the driving field.

As shown in Figure 3-10, to each value of the phase difference between the outer and the inner part of the XUV beam, can be attributed a very characteristic focusing structure. Taking this into account, for the analysis of our experimental data we followed the opposite way. The characteristic focusing structures observed in the pictures provided by the Ion Microscope (I-ID) are treated as the trace of the $\Delta\varphi(I_L)$.

3.4.1 Computer Simulation

In parallel with the experimental procedure, a computer simulation of the experiment is elaborated. Images of the XUV distribution at the focus are calculated taking into account the special features of our setup, the intensity distributions on the profile of the generated XUV beam, as well as the relative phases of the field between different parts on this beam profile.

The calculated XUV images of the focus are obtained by the Debye integral^[80], after applying the Huygens–Fresnel principle on a spherical mirror with 10 cm radius of curvature [for a more detailed description about this technique of calculation, read Section 4.4.1 in the next chapter]. The profile of the XUV beam on the spherical mirror is selected taking into consideration relevant references^[38,52] in the scientific literature [see Figure 3-8 and the caption under it], as well as direct experimental measurements with our setup [see Figure 3-12]. In any case, a structure consisting of two parts is chosen. An inner central area with a gaussian intensity distribution simulating the “*Short*” trajectories contribution and an outer annular area, with a gaussian intensity distribution as well, simulating the “*Long*” trajectories contribution. In both areas, the amplitudes of the harmonics in the plateau are considered as equal (which is a good approximation according to the literature^[27,89,90]).

In the Figure 3-8 we give an example of intensity distribution of the XUV beam profile on the spherical mirror which is in accordance with the literature^[38,52]. Structures of the XUV distribution at the focus calculated taking into account this profile are shown in the Figure 3-9 and the Figure 3-10. For the sake of simplicity and clarity, and in contrary to how we proceed in the rest of our study, for this example the relative phases for the “*Long*” and the “*Short*” contributions of the harmonics are not obtained from the single-atom three-step model. Here, we only consider one and a single phase difference $\Delta\varphi$ between the outer and the inner part of the profile and we give the focusing structures for the most characteristic values of $\Delta\varphi$. These structures and their correlation with $\Delta\varphi$, are of great importance for this study.

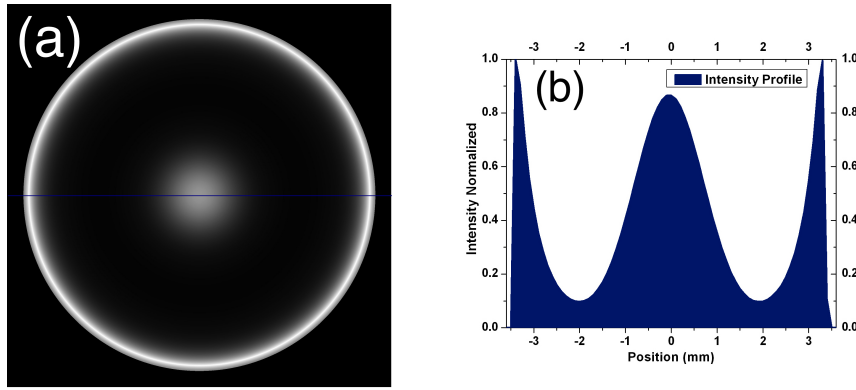


Figure 3-8 : In (a) appears the intensity profile (dark-bright in linear scale), as it appears on the “virtual” spherical mirror, used for the calculation of the exaple foci images presented in the Figure 3-9. The XUV beam is taken with a diameter of 6.4 mm and consisted of two distinct parts. The inner part represents the contribution from the “Short” trajectories and is simulated by the radial function: $I_s(r) = \exp[-r^2/r_s^2]$, for $0 < r < 3.2\text{mm}$ and $r_s=1\text{mm}$. The outer part represents the contribution from the “Long” trajectories and is simulated by the radial function: $I_L(r) = 1.6 * \exp[-(r-r_0)^2/r_L^2]$, for $0 < r < 3.2\text{mm}$, $r_0 = 3.1\text{mm}$ and $r_L = 1.5\text{mm}$. In (b) is depicted the intensity as a function of the position of each point on the blue line drawn in (a). The intensity profile as simulated here is based on the XUV profiles detected by Salieres et al.^[38] and the divergence law given by Protopapas et al.^[52], taking into account the special geometry of our experimental setup. The harmonics used for this example are the 11th, the 13th and the 15th. In contrary to how we proceed in order to simulate our experimental data in the rest of this chapter, here the relative phase for each harmonic (“Long” or “Short”) is not obtained by the numerical solution of the three-step-model [M.Skantzakis, PhD Thesis, 2011]^[82]. All the harmonics within each one of the two parts (inner or outer) are supposed to be in phase.

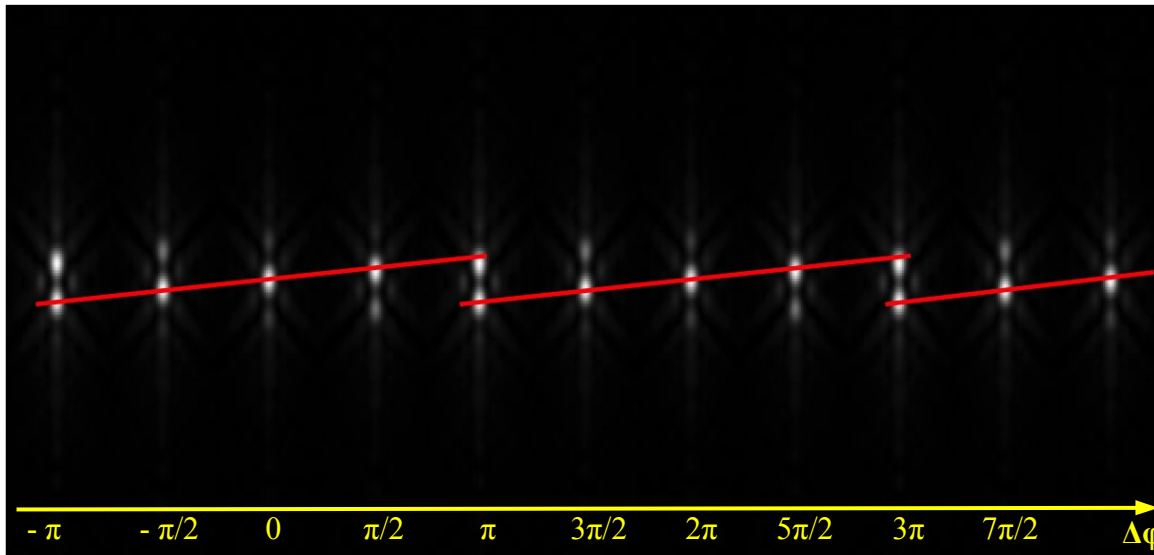


Figure 3-9 : The Saw-Type structure

A series of XUV distribution structures simulated using the XUV beam profile shown in the Figure 3-8. Between successive images, $\Delta\phi$ increases of $\pi/2$. A “saw-type” structure appears to be formed by the maxima in intensity. Compare with the line-outs shown in Figure 3-17. In the next figure (Figure 3-10), the reader can find a more detailed description of the focusing structures shown here in series.

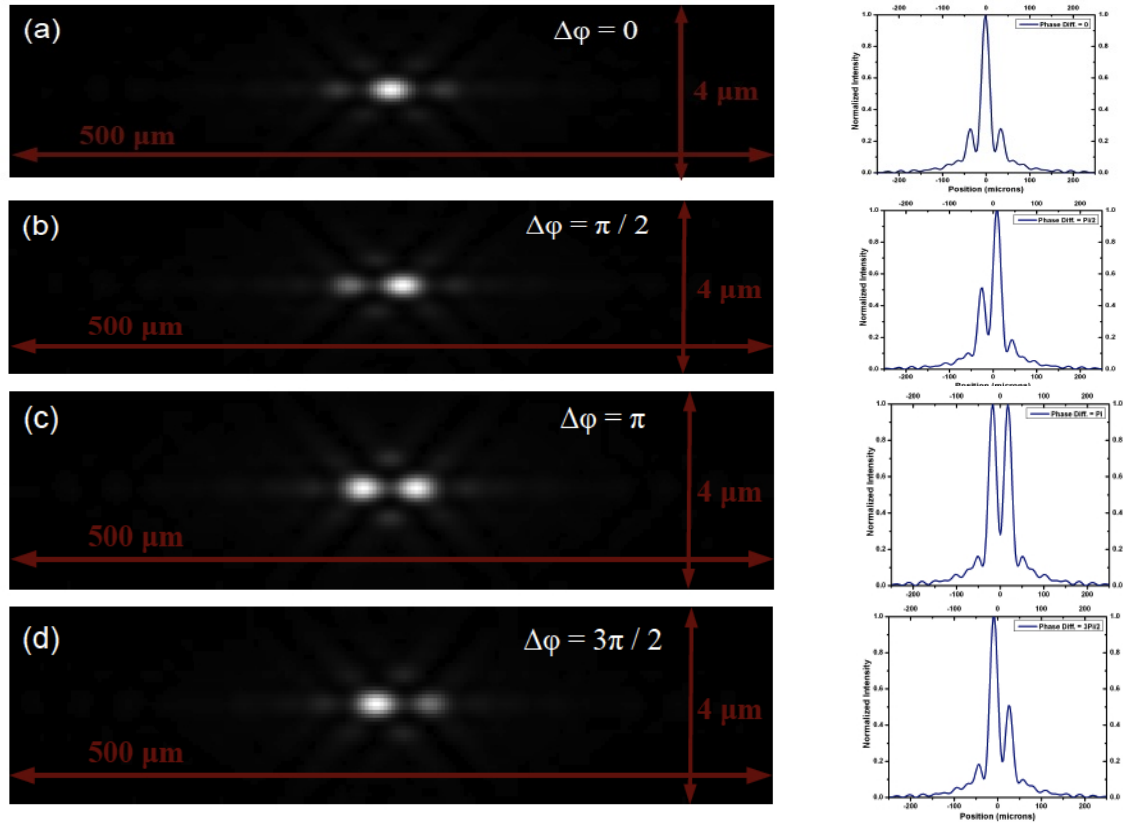


Figure 3-10 : By using the XUV beam profile shown in the Figure 3-8, the structure is simulated for four characteristic values of the phase difference $\Delta\varphi$ between the “Long” and the “Short” harmonics. In the images above, is depicted the normalized intensity distribution (in dark-bright linear scale) for every plane which contains the beam focusing axis (z -axis). The cylidrically symmetrical geometry of the focusing setup induces a cylidric symmetry to the focusing structure. The graphs on the right side of every picture represent the intensity distribution along the z -axis. It is very interesting to notice the characteristic single-maximum structure for $\Delta\varphi = 2n\pi$ and the characteristic double-maxima structure for $\Delta\varphi = (2n+1)\pi$, n being integer in both cases. For other values of $\Delta\varphi$, an asymmetric double-maxima structure can be observed. It is very interesting also to notice that the maximum value of the intensity “moves” away from the point of the geometrical focus ($z = 0$) for every $\Delta\varphi$ different than $2n\pi$, n being integer. One final remark concerns to the brightness of the four simulated images above. The intensity distribution, in each one of the figures above, is normalized. So, the maxima appear equally bright. In reality, the maxima of the double-maxima structures are less intense than the maximum in the case of the single-maximum structure (“Long” and “Short” contributions being in phase).

In order to ascertain the coincidence between the computer simulation and the experimental conditions, we need a direct measurement of the diameter of the XUV beam on the spherical mirror of our experimental setup [see Figure 3-5]. This measurement is performed with two different methods. The first one is to use pictures already recorded by the Ion-Imaging-Detector in order to extract from them the angle of convergence of the focusing XUV beam. Taking into account the 5cm focal length of the spherical gold coated mirror, we can estimate the XUV beam diameter to be ~ 5 mm [see Figure 3-12.(e)]. The second method is to apply a direct Knife-Edge technique [see Figure 3-12.(d)]. Such an application on the 11th harmonic, offers an estimation of the beam diameter ~ 4.5 mm. Both methods can also reveal elements from the internal structure of the beam. These experimental evidences became an additional guide to computer simulate the profile of the XUV beam on the spherical mirror. This is a crucial point concerning to the whole simulation. The assumption about the size and the intensity distribution of the XUV beam profile on the spherical mirror has implications on the size of the peaks and the distance between them in the various

structures [shown in the Figures 3-9 and 3-10].

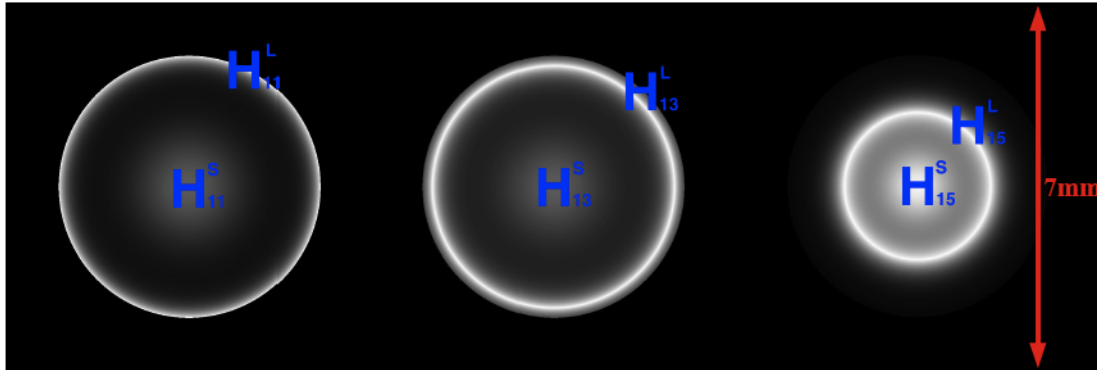


Figure 3-11 : Normalized calculated profiles of the 11th, 13th and 15th harmonics on the surface of the EUV focusing mirror, at $I_L = 3 \cdot 10^{13}$ W/cm². The relative amplitudes and phases of the inner and outer EUV beams were determined from the three-step model. The beam diameters on the surface of the mirror for the “Short” and “Long” trajectory harmonics are taken in such a way as to be in accordance with our experimental data shown in the Figure 2-11. The diameter found to be approximately the same for all the harmonics in the “plateau”.

Here a simple way to simulate the XUV beam profile is chosen, which approximates the real profile to a reasonable extend. We use two gaussian radial distributions. The one, simulating the “Short” contribution, is expressed by: $I_S(r) = \exp[-r^2/r_S^2]$, with $r_S = 1.25$ mm. The second, simulating the “Long” contribution: $I_L(r) = 2 \cdot \exp[-(r-r_0)^2/r_L^2]$, with $r_0 = 2.5$ mm and $r_L = 1$ mm. For harmonics being in the cut-off spectral area, an exponential decay of the harmonic field amplitude is considered. In addition to this, is introduced a reduction of both the radii of the “Long” and the “Short” part of the profile according to a law of inverse square root in respect to the order of the harmonic. The relative field amplitudes of the harmonics inside the detection area are simulated by taking also into account the reflectivity of the spherical golden mirror for each one of them. Explicitly, the manufacturer gives the following reflectivities: 13,4% for the 11th, 12,5% for the 13th, and 7% for the 15th. Finally, the relative phases for each harmonic and for each contribution (“Long” and “Short”), for a certain intensity value I_L of the driving field, are calculated from the single-atom three-step semi-classical model^[36] as it is computationally solved by E. Skantzakis^[82].

Two characteristic structures calculated by using the above assumptions are shown in the Figure 3-13. A double-peak structure for $I_L = 7,3 \cdot 10^{13}$ W/cm², and a single-peak-structure for $I_L = 6,7 \cdot 10^{13}$ W/cm². In comparison with those shown already in the Figure 3-10, we can immediately notice that these new ones (in the Figure 3-13) seem to be more blur. This happens because the difference in phase, between the “Long” and the “Short” contribution for each harmonic, are now calculated via the Three-Step-Model computational solution^[82] and not “put by hand”. For all the three harmonics considered here and for a certain value I_L , the Three-Step-Model does not predict the same phase difference $\Delta\phi$ between their “Long” and their “Short” contribution. For the double-peak-structure shown in the Figure 3-13.(a) we can just say that $\Delta\phi \sim \pi$, meaning that each one of the three $\Delta\phi_q$ is close to π . The same is valid for the single-peak-structure shown in the Figure 3-13.(b). There, $\Delta\phi \sim 0$ means that each one of the three $\Delta\phi_q$ is close to 0. One can also notice that the focusing structures presented in Figure 3-13 are larger in size than those in the Figure 3-10. This is due to the “blurring” just mentioned and discussed, but also to the smaller diameter of the XUV beam profile [see Figure 3-12] used for this calculation in comparison to the one [see Figure 3-8] used

previously.

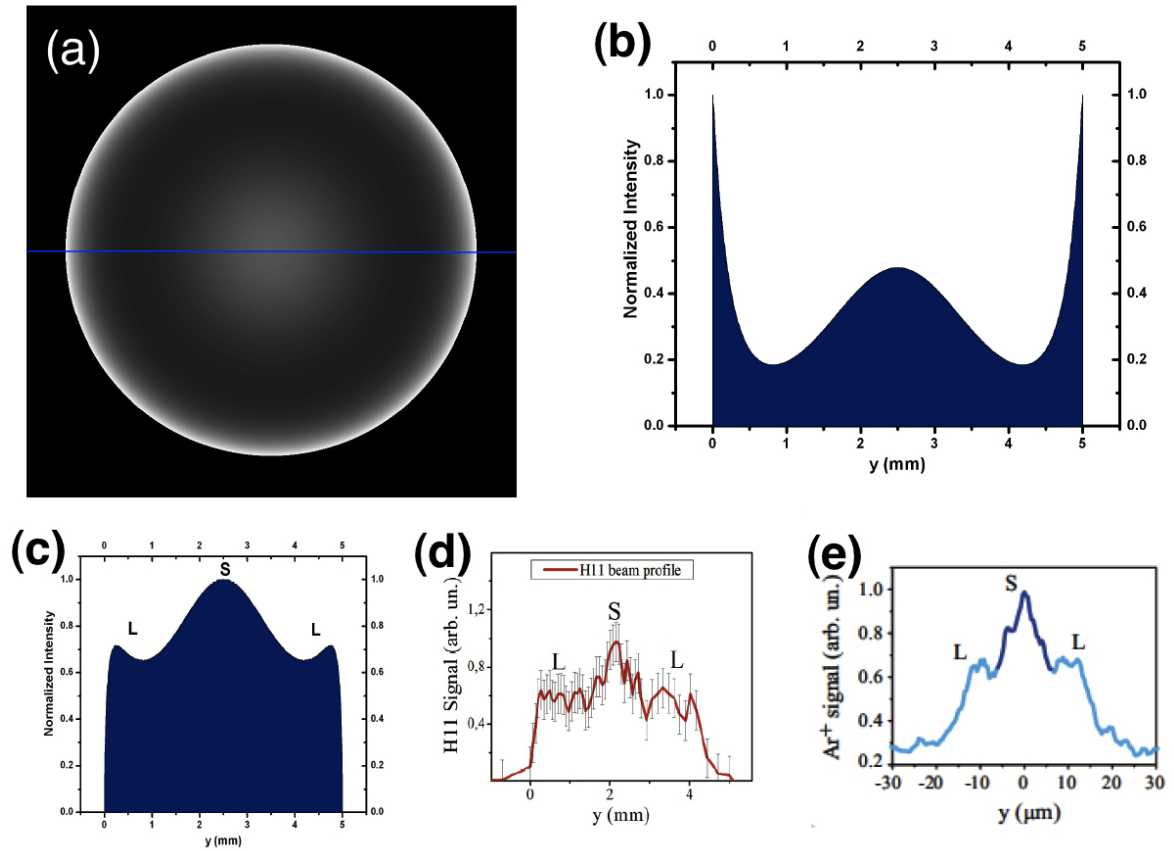


Figure 3-12 : (a) shows the intensity profile (dark-bright in linear scale), as it would appear on the spherical mirror, used for the calculation of the foci images presented in the Figure 3-13. The XUV beam is taken with a diameter of ~ 5 mm and consists of two distinct parts. The inner part represents the contribution from the “Short” trajectories and is simulated by the radial function: $I_S(r) = \exp[-r^2/r_S^2]$, with $r_S = 1.25$ mm. The outer part represents the contribution from the “Long” trajectories and is simulated by the radial function: $I_L(r) = 2 \exp[-(r-r_0)^2/r_L^2]$, with $r_0 = 2.5$ mm and $r_L = 1$ mm. In (b) is depicted the intensity as a function of the position on the blue line drawn in (a). The intensity profile as simulated here is based on the XUV profile structures detected by Salieres et al.^[38], as well as on information obtained by the experiment. The harmonics used for this example are the 11th, the 13th and the 15th. In order to depict the intensity distribution on the profile, the “Long” and the “Short” contributions are supposed to be in phase. In (c) is shown the projection, of the profile shown in (a), on the horizontal axis. For each point of the horizontal axis, we take the integral of the signal along the vertical line which passes from it. In (d) is shown the horizontal intensity distribution of the 11th harmonic on the surface of the golden spherical mirror determined by means of knife-edge technique. The beam profile and the diameter of the 13th and 15th harmonics (for simplicity are not shown in the figure) are approximately the same with the 11th. (e) shows the measured, by the Ion-Imaging-Detector, EUV ionization signal along a direction transverse to the propagation. Clearly are depicted the on-axis (S-trajectories contribution) and off-axis (L-trajectories contribution) distinct parts. From this Figure we can extract information about the XUV beam profile on the surface of the mirror by taking into account the focal length of the mirror and the measured angle of convergence of the focusing beam.

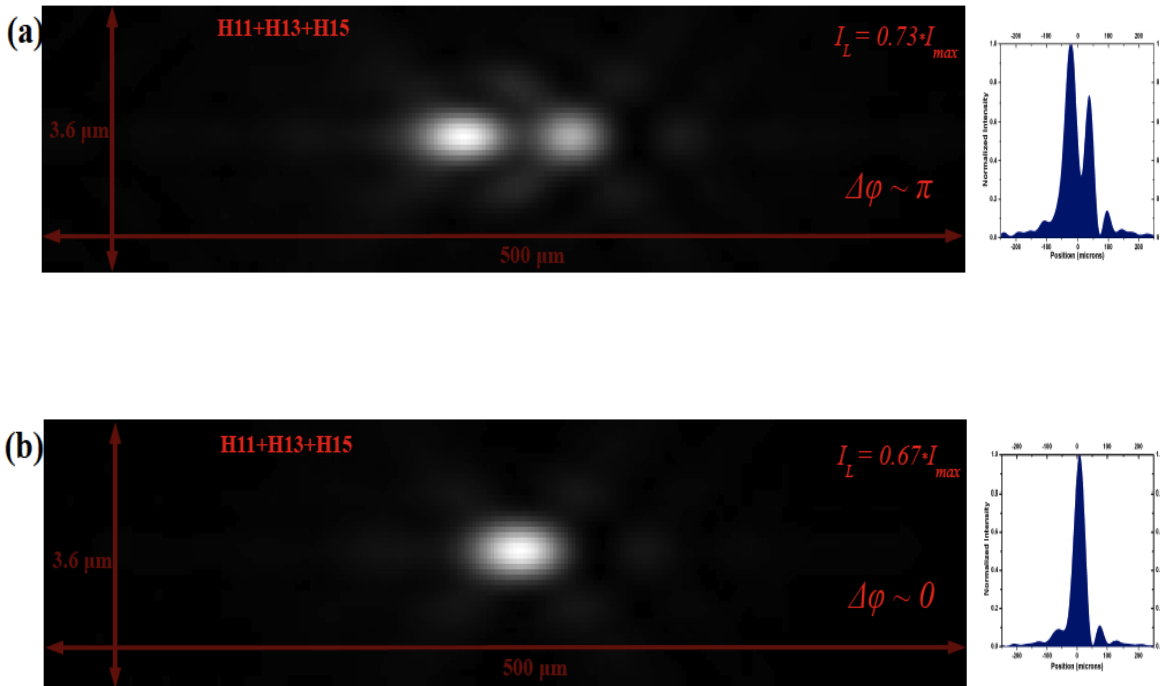


Figure 3-13 : Panels (a) and (b) show the calculated images of the focused EUV beam at two different values of I_L : $I_L = 0,73 \cdot 10^{14}$ and $I_L = 0,67 \cdot 10^{14}$ respectively. At these intensities, the phase distribution of the EUV beam lead to on axis (z) destructive (a) and constructive (b) interference at the focus position with a double- (maxima at $z = \pm 30 \mu\text{m}$) and single- (maximum at $z = 8 \mu\text{m}$) peak structure, respectively. On the right side of each panel the intensity distributions along the propagation axis (z) are shown. Similar but sharper features appear in the image of the focal area for each individual harmonic. The interference pattern appearing in the blue shaded areas is the fingerprint of the spatial phase distributions of the beam along the z (propagation) axis. The phase distribution of the harmonics, for each I_L , has been calculated by using the three-step quantum mechanical model [see Emmanouil Skantzakis PhD Thesis, 2011 University of Crete]. For the considered values of I_L , harmonics 11th, 13th and 15th are lie in the “plateau” spectral region having approximately equal relative amplitudes.

It would be very interesting to make an effort now to estimate how these focusing structures would be imaged by the detector [The Ion-Imaging-Detector (I-ID), see section 3.2.]. For this purpose we need to project, on the plane of the MCP of the Detector, the total signal from the ions which are produced inside the focal space. The simplest way to deal with this is to take profit of the cylindrical symmetry of the focusing structures and to integrate, in respect to the vertical axis (-y), the simulated signal on panels (a) and (b) in the Figure 3-13. This signal corresponds to the ion-signal coming from 1-photon ionization, because in this case the intensity distribution coincides with the ion-distribution. By doing so, we obtain the total ion-signal as it would be projected along the central horizontal axis of the plane of the MCP.

In the Figure 3-14 appear the projections of this kind which correspond to the focusing structures presented in the Figure 3-13. It becomes clear that the “projected” picture of a certain focusing structure is “smoothed” in comparison to the “not projected” one. These “projected” pictures are expected to be much closer to what the experiment will show [See Figure 3-15].

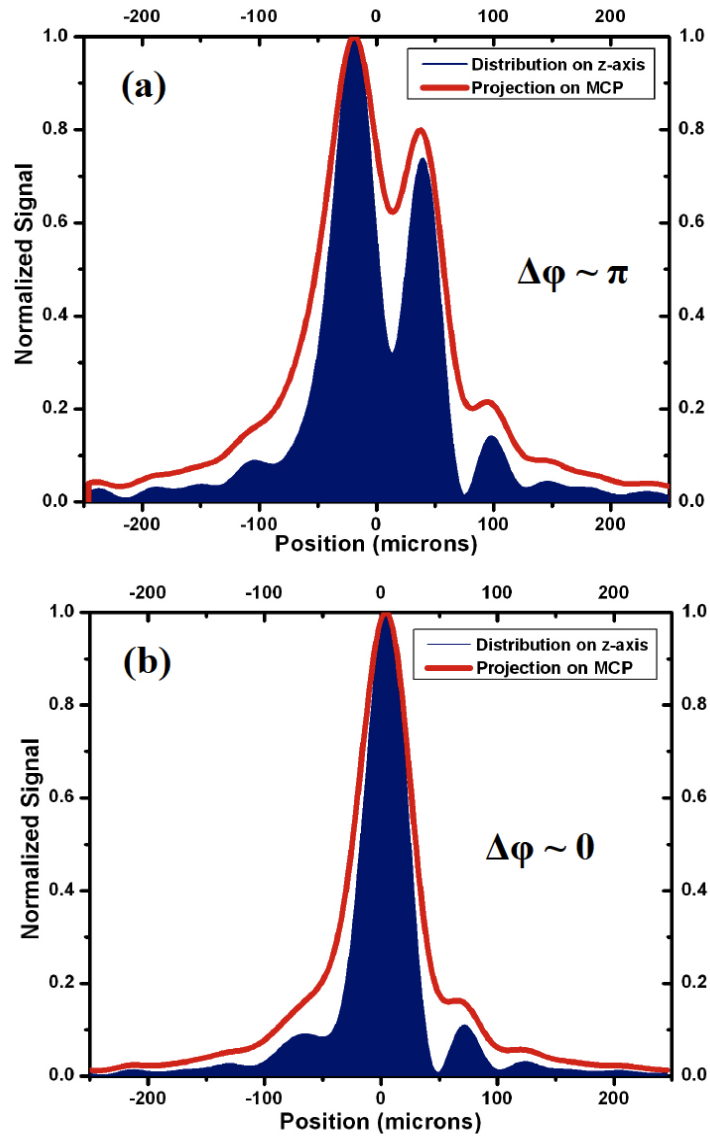


Figure 3-14 : (a) Projection of the intensity distribution along the central horizontal axis (the projected “focusing” axis) on the plane of the MCP of the Ion-Imaging-Detector (red line) for the double-peak focusing structure presented in the Figure 3-13.(a). The blue-shaded area, showing the intensity distribution along the z-axis of propagation of the beam, is taken from the Figure 3-13.(a) and is added here for reasons of easier comparison. (b) Projection of the intensity distribution along the central axis (the projected “focusing” axis) on the plane of the MCP of the Ion-Imaging-Detector (red line) for the single-peak focusing structure presented in the Figure 3-13.(b). The blue-shaded area, showing the intensity distribution along the z-axis of propagation of the beam, is taken from the Figure 3-13.(b) and is added here for reasons of easier comparison.

3.4.2. Focusing structures taken from the experiment by one-photon ionization process

Up to this point, we have shown only various focusing structures calculated by the simulation program. We have discussed also the physics behind these structures and the connection of their features to the phase difference between the two distinct parts of the XUV beam. Nevertheless, the

experimental observation of the interference pattern described above is the necessary point connecting Theory and Experiment in our study. In the Figures 3-15(a) and 3-15(b) are shown ion distributions recorded at the EUV focus, for two different values I_L of the driving field, using Argon as a target gas. The characteristic interference patterns, exhibiting a double- [Figure 3-15(a)] and a single- [Figure 3-15(b)] peak structure around the focus, are in agreement with the characteristic distributions which appear in the Figure 3-14(a) and the Figure 3-14(b), respectively.

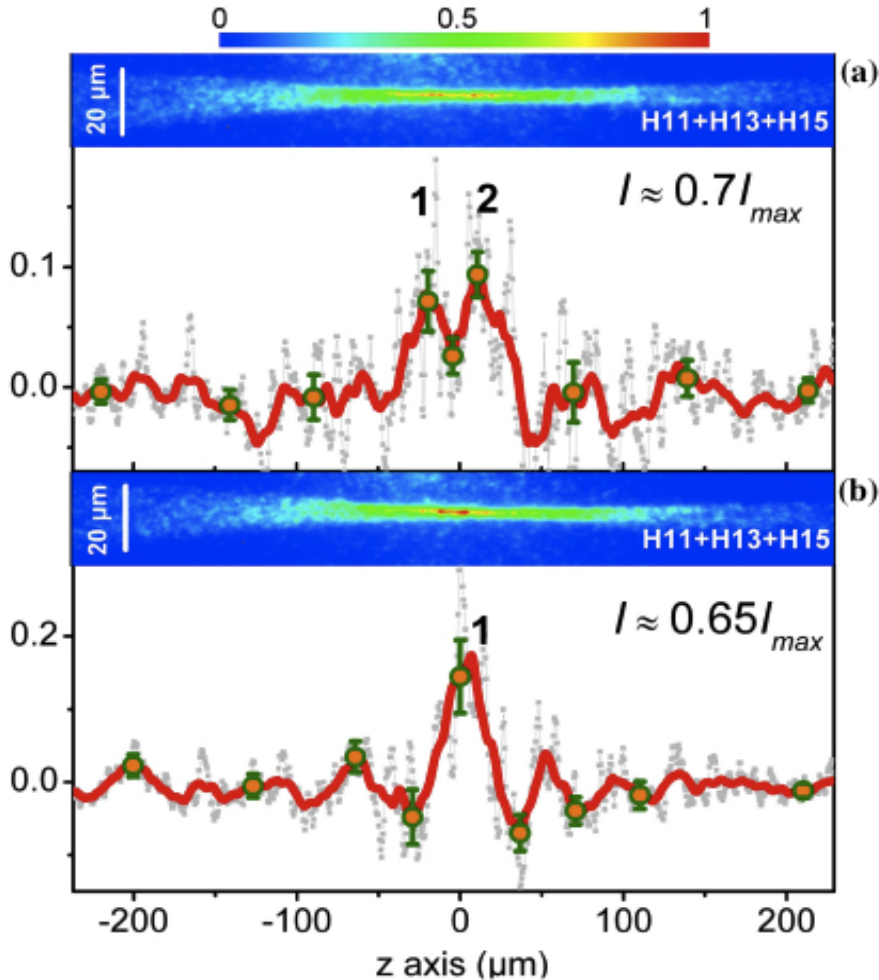


Figure 3-15: The interference pattern created experimentally at the focus of the EUV beam

EUV focus images produced by the single-photon ionization signal of Argon at two different drive-laser intensities I_L , I_{max} being $\sim 10^{14}$ W/cm². The relative amplitudes of the harmonics in the interaction region were approximately equal for both images [see Figure 3-7]. The images show a characteristic interference pattern along the z-axis, with a double and single peak structure around the focus, respectively. The red lines are the 30-points running average of the raw data and the error bars represent one standard deviation from the mean value. 600 shots are accumulated for each image. To make the trend clearer, the interference pattern in both cases is retrieved after subtraction of the smoothed part of the signal (background signal). Reasons which are limiting the modulation depth of the interference pattern in the images, is (I) the existence of a background signal which is coming from the contribution of the out of plane signal in the projected focus image, (II) the ion signal which is produced by the incoming (unfocused) EUV beam, and (III) the finite resolution of the I-ID. The fringe visibility of the interference pattern is reaching almost its optimum value after subtracting the background signal.

3.4.3. Focusing structures taken from the experiment by two-photon non resonant ionization process

In order to take more experimental information about the structures presented in the Figure 3-15, pictures produced by two-photon non resonant ionization process have been recorded. Using Helium as a target gas, filtering the XUV beam by using an 150 nm thick Sn metal filter, and increasing for many times the exposure time of the recording apparatus in order to accumulate up to 15000 shots for each recorded image, we obtained the pictures which appear in the Figure 3-16. A clear difference between the single- and two-photon ionization images, which is associated with the different order of non-linearity of the involved processes, is the overall width of the contrast of the ion distribution pattern. The width of the profile along the z axis is found to be of a factor of ~ 1.4 narrower in Helium (2-photon process ionization) than in Argon (1-photon process ionization). Although the signal-to-noise ratio in these pictures is poor, the high fringe contrast supports the claim that the observed structures are real and according to the expectations.

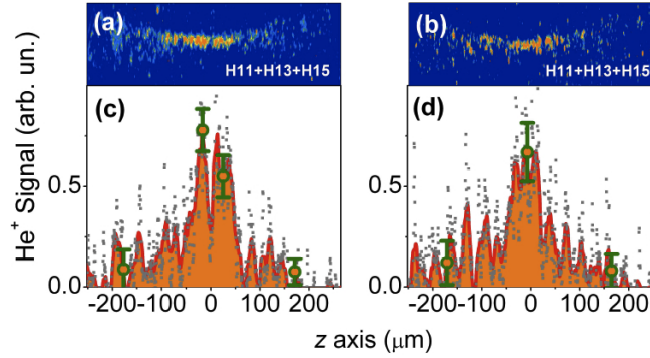


Figure 3-16 : Non-linear visualization of the EUV-amplitude-distribution. **a)** and **b)** EUV focus images recorded by monitoring the two-photon ionization signal of Helium, at intensity values of $I_L \approx 10^{14}$ W/cm² and $I_L \approx 0.9 \cdot 10^{14}$ W/cm². The EUV radiation is spectrally filtered by using an 150 nm thick Sn metal filter. For each image 15000 shots have been accumulated. **c)** and **d)** Intensity line-outs along the propagation axis (z). The red lines are the 30-points running average of the raw data and the error bars represent one standard deviation from the mean value.

3.4.4. The “saw-type” structure

As the electron quantum path interference is strongly dependent on I_L , we perform a systematic recording of the ionization focus images at different driving intensities. This dependence is shown in the contour plot of Figure 3-17(a). In this measurement, an intensity dependent interference pattern along the z -axis is observed. The dependence is clearly shown as a modulation from a single- to a double-peak structure in the normalized contour plot of Figure 3-17(b), which clearly confirms the statistical relevance of the structures shown in Figures 3-15(a) and 3-15(b). The **“saw-type” structure** is the result of the phase angular distribution of the harmonics. This structure is strongly pronounced at high I_L values, for which most of the harmonics, in the group of the 11th, the 13th and the 15th, lie in the “plateau” region. As the intensity of the driving field decreases, at different I_L values for each harmonic, becomes observable the transition which occurs from the “plateau” to the “cut-off” region. A clear and intensity independent single peak structure appears

only for very low I_L values. There, all the harmonics lie clearly in the deep “*cut-off*” region. The measured structures are found to be in fair agreement with those retrieved from the simulation program [see Figure 3-17(c)].

An advantage of the present approach in comparison to interferometric approaches^[78] is that any dispersion effect, which may be introduced by the ionization in the harmonic generation region is physically absent here. This is because the whole information about the harmonic emission time differences is obtained by measuring the phase differences between the contributions of “*Short*” and the “*Long*” trajectories to the same harmonic. These contributions, which interfere here, are generated “together”. They come from one and a single EUV source and they do not emerge from two distinct EUV sources, like in previous experiments^[51,86,87]. Also the influence of any transient phase-matching effect, which results to the spectral broadening of the “*Long*” trajectory harmonics^[79], has negligible influence in these measurements. This is because the present study is based on the observation of extremes (maxima and minima) in the constructive and destructive interference pattern resulting by the overlap of the same carrier frequency of “*Short*” and “*Long*” trajectory harmonics.

The values of $\Delta\varphi^{S,L}$ can be deduced from the “saw-type” structure by using the following three considerations:

- (a) $\Delta\varphi^{S,L} = 0$ for the very low values of I_L , where an intensity-independent single peak structure can be observed. This element is in agreement with the harmonic generation theory according to which, in the “*cut-off*” region, the two trajectories degenerate into one.
- (b) The $\Delta\varphi^{S,L}$ is increasing monotonically with I_L ^[58].
- (c) The $\Delta\varphi^{S,L}$ is increasing by π when we go from a single to the following double peak and vice versa.

Taking into account the above three considerations we are able to use the experimental data of the “saw-type” structure, shown in the Figure 3-17, in order to extract the dependence of $\Delta\varphi^{S,L}$ on I_L . In the Figure 3-19(a), are shown the values of $\Delta\varphi^{S,L} = n\pi$ ($n = 0, 1, 2, \dots$) as a function of I_L .

The phase acquired by the electron wave function in the continuum can be given (see Chapter 2), in a rough approximation, as :

$$\varphi_q^{S,L} \approx \frac{t_e^{(q)S,L} \cdot U_P}{\hbar} = -\alpha_q^{S,L} \cdot I_L \quad (3.1),$$

where $\alpha_q^{S,L}$ is the phase coefficient of the q^{th} harmonic emitted by “*Short*” and “*Long*” trajectories respectively, $t_e^{(q)S,L}$ is the emission time of the q^{th} harmonic photon for the “*Short*” and “*Long*” trajectories respectively, U_P is the ponderomotive potential^[41].

From the measurements [see Figure 3-19.(a)] it can be shown that for the Xenon gas, which is used for the generation of the Harmonics here, can be obtained:

$$\Delta\alpha_q^{S,L} = \alpha_q^S - \alpha_q^L \approx 44 * 10^{-14} \frac{\text{rad cm}^2}{\text{W}} \quad (3.2),$$

for $q = 11, 13, 15$.

Although, the value $\Delta\alpha_q^{S,L}$ has been already demonstrated for Argon, Krypton and Neon^[78,79,41,83-85], for Xenon until now there has been a lack of information. The value of $\Delta\alpha_q^{S,L}$ which is obtained here, is in fair agreement with the theoretical predictions for the dominance of the two “shortest” (“*Short*” and “*Long*”) electron trajectories^[57,41,84,85] and the recent experimental findings^[79], while is larger by factor of ~ 3 compared to previously reported experimental values in Argon and Krypton^[79].

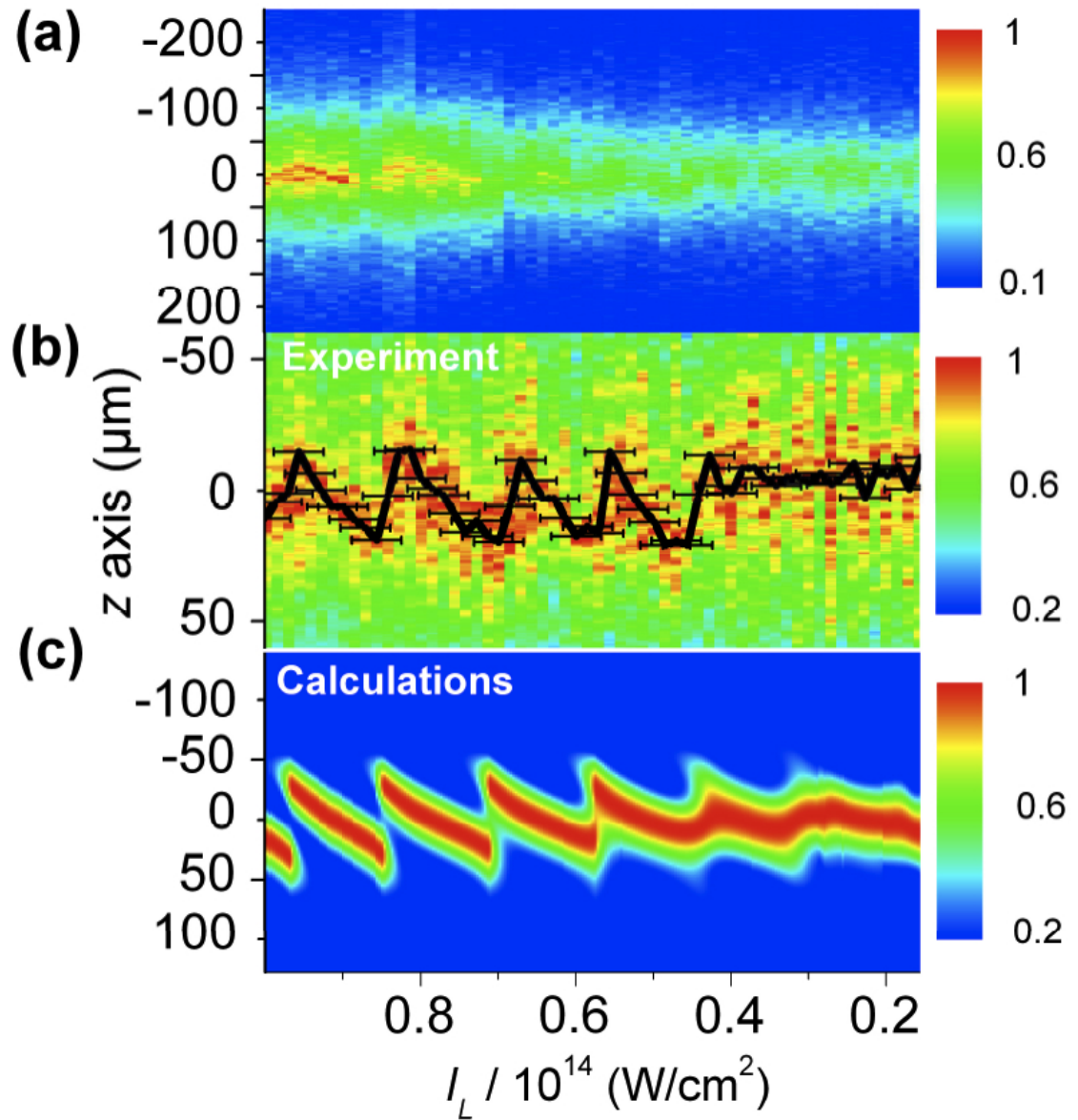


Figure 3-17: Visualization of the intensity dependant spatial EUV-yield-distribution.

a) Contour plot which shows the dependence, on the I_L , of the interference pattern (induced by single-photon ionization of Argon) along the z axis. For each value of I_L , 600 shots are accumulated. The focus position of the IR field is placed on the Xenon gas jet. In order to avoid any influence on the EUV beam that may be introduced by the filter, a spectrally unfiltered EUV radiation has been used. The relative amplitudes of the harmonics 11th, 13th and 15th in the interaction region are those already shown in Figure 3-7. **b)** Contour plot retrieved after normalization of the plot (a). The black line depicts the maxima of the ion distribution. The error bars represent the standard deviation from the mean value resulted by taking into account the accuracy on measuring the laser intensity. **c)** Normalized calculated contour plot which shows the dependence on I_L of the interference pattern along the z -axis. We have to keep in mind that even if the “saw-type” structure and the positions of the maxima on the z -axis are in agreement with the measured values, these calculations are meant to show only the general features of the measurements. They do not provide the possibility of a quantitative comparison with the data extracted from the Experiment.

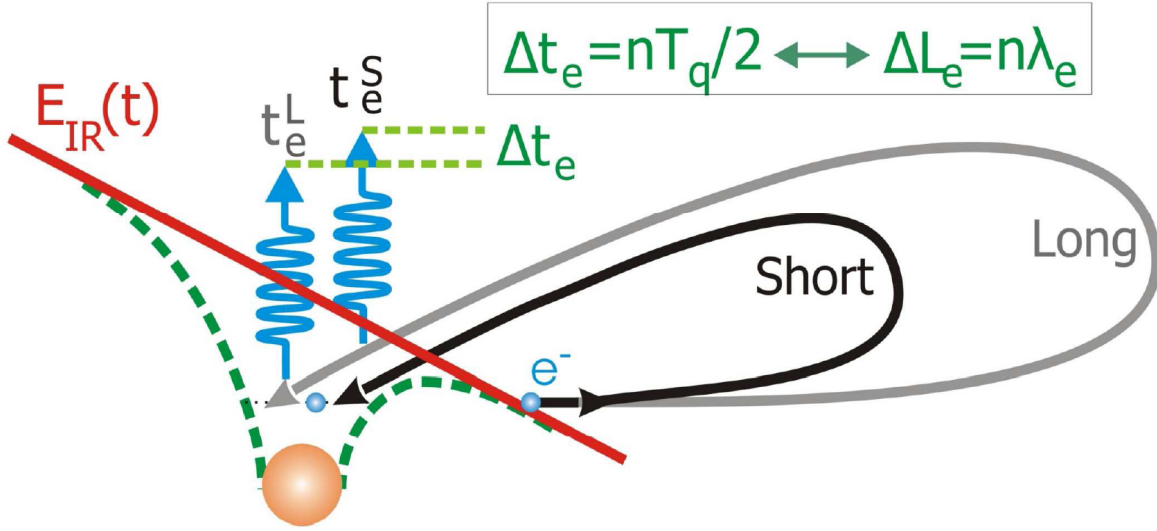


Figure 3-18: High-order-harmonic generation mechanism shown in the spirit of the “three step model” [34,36, 81]. The IR field suppresses the atomic potential and allows the valance electron to tunnel through. The electron moves almost freely in the driving field gaining kinetic energy, which is converted to photons upon its recombination.

A characteristic time value Δt_e can be associated to every phase difference value $\Delta\varphi^{S,L}$:

$$\Delta t_e = \frac{\Delta\varphi}{\omega_{average}} \quad (3.3)$$

where $\omega_{average}$ reflects the average value of the harmonic angular frequency weighted by the harmonic amplitude E_q . Namely:

$$\omega_{average} = \frac{\sum_q E_q \cdot \omega_q}{\sum_q E_q} \quad (3.4)$$

By using the experimental data (pairs of values $\Delta\varphi^{S,L} = n \cdot \pi$, $\{n = 0, 1, 2, \dots\}$ and the mean intensity values I_L) shown in the Figure 3-19(a), the corresponding characteristic time value Δt_e can be deduced [see Figure 3-19(b)]. One just needs to take into account that differences in phases $\Delta\varphi^{S,L} = n \cdot \pi$, $\{n = 0, 1, 2, \dots\}$, correspond to differences $\Delta t_e \approx \Delta t_e^q = n(T_q/2)$ in characteristic time values. Where T_q is considered to be the time period of the q -order harmonic.

In addition to the characteristic time value Δt_e , a characteristic length value ΔL_e can also be defined as:

$$\Delta L_e = \sqrt{2 \cdot \hbar \omega_{average} / m_e} \Delta t_e \quad (3.5),$$

where $\hbar \omega_{average} = E_e + I_p$. E_e stands for the return kinetic energy of the recolliding electron and I_p is the binding energy of the atom [36,55].

We know that for a single recollision: $0 \leq E_e \leq 3U_p$ [36] and, as a result, the above formula (3.5) can be approximated by:

$$\Delta L_e \approx \sqrt{2(1,5U_p + I_p)} / m_e \Delta t_e \quad (3.6).$$

Extracting the ratio $f(I_L) = \Delta L_e / \lambda_e$, of the characteristic value ΔL_e to the mean De Broglie electron wavelength:

$$\lambda_e = h / \sqrt{2m_e(1,5U_p + I_p)} \quad (3.7),$$

is found [see Figure 3-19.(c)] that for $\Delta t_e \sim n \cdot T_q / 2$, $\Delta L_e \sim n \cdot \lambda_e$. This is clearly shown in the intensity dependence of the differences $\Delta f(I_L) = f(I_L^{(i)}) - f(I_L^{(i+1)})$, $\{i = 1, 2, \dots\}$ [see Figure 3-19(d)]. There, easily can be seen a characteristic change between the “plateau” and the “cut-off” areas. Between every two consecutive values of $f(I_L)$, in the plateau area, one obtains $\Delta f(I_L) \sim 1$. The small drift of $\Delta f(I_L)$ from the mean value 1, is mainly due to a deviation of E_e from the value of 1,5 U_p . On the other hand, inside the I_L interval where all the three harmonics stand on the “cut-off” part of the spectrum, one obtains $\Delta f(I_L) \sim 0$.

These results provide motivation to seek for a new understanding of the high-order harmonic generation in the context of the quantum information processing^[88].

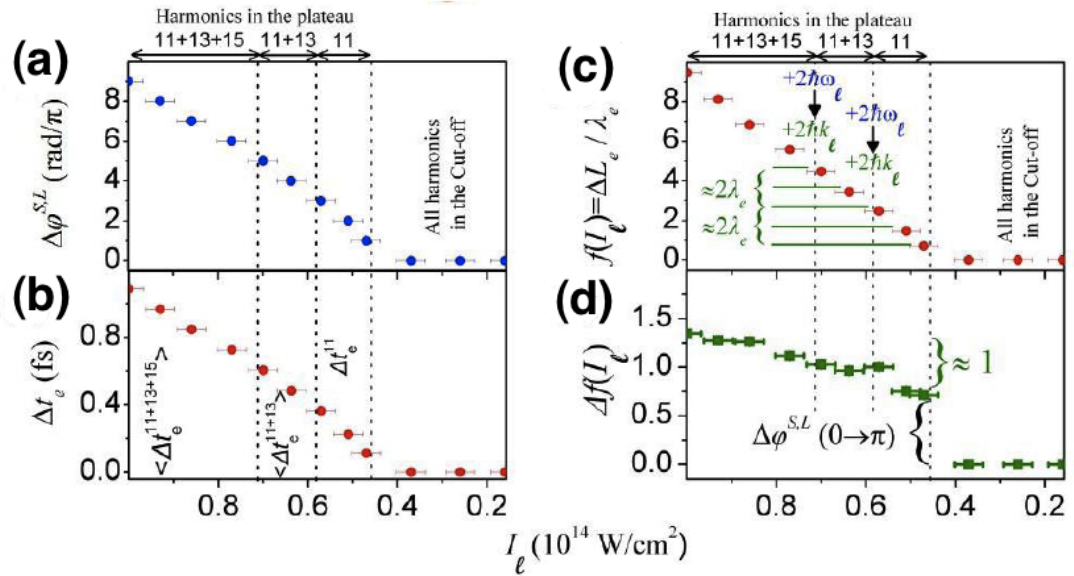


Figure 3-19 : (a) Measured phase difference between the “Short” and “Long” trajectories as a function of I_L . (b) Characteristic time values Δt_e as a function of I_L . (c) Characteristic length values ΔL_e normalized by the mean DeBroglie electron wavelength λ_e . $\Delta t_e \sim n \cdot T/2 \Rightarrow \Delta L_e \sim n \cdot \lambda_e$. (d) Difference between two consecutive values of $f(I_L)$. In all graphs, the vertical black-dotted lines depict the harmonic “cut-off” points and the error bars represent one standard deviation from the mean value.

4th Chapter

A single-shot XUV autocorrelator

4.1. Introduction

The availability of attosecond pulses is now rather common in a number of laboratories. Spurred by the rapid progress in modern laser systems, different methods of generation have been developed. They are all based on producing a quasi or pure spectral continuum in the XUV spectral range, which in the time domain corresponds to a train or even isolated attosecond pulses^[91,92,54]. However, the readily accessible quantitative characterization of the attosecond pulse is still a challenge^[93]. A complete measurement would provide information on the number of as-pulses produced, on their duration and ultimately about the temporal shape and spectral phase of the individual pulses. The common techniques used up to now can be divided into two main categories: (a) cross-correlation and (b) auto-correlation techniques. In the first category is the so called RABITT (**R**econstruction of **A**ttosecond **B**eating by **I**nterference of **T**wo-photon **T**ransitions) method for a train of attosecond pulses^[14,58,94,95] and the "streaking" or the XFROG method for isolated pulses^[96-99]. The second category includes the IVAC (**I**ntensity **V**olume **A**uto-**C**orrelation)^[100-103] and the XUV-FROG techniques^[104,105]. All these methods have been frequently applied, but are in fact relatively cumbersome. They typically require acquisition over many (up to several millions) laser pulses, thus can only be utilized in conjunction with a high repetition rate laser or low repetition with good stability so that accumulation of single events is feasible.

For the various applications of the as-pulses envisioned, it is highly desirable to have a quick and reliable characterization of the attosecond source before launching an extensive experimental series. Furthermore, in case of poor laser parameter stability (pulse energy, carrier envelope phase (CEP), duration), it is important to be able to periodically optimize the as-pulse duration. This is of particular importance for non-linear applications of as-pulses^[104,77,106,107]. Consequently, an approach in which a single-shot or at the most a few-shot measurement can reveal the necessary information in a routinely used fashion would be very helpful^[108]. A technique for single-shot characterization of attosecond pulses based on spectral phase interferometry is the XUV-SPIDER^[109, 110]. In this

scheme, the two interfering beams are produced by splitting and manipulating the IR beam, which is used to generate the XUV photons. Although this characterization method is under certain conditions appropriate for XUV sources using atomic media, it is not in general applicable to every XUV source.

Here, we propose a scheme in which the conventional method commonly used in fs-pulse metrology of the single-shot second-order intensity autocorrelation technique is extended by appropriate modifications to operation in the XUV spectral range. In the visible and IR part of the spectrum, the technique consists of crossing two pulses in a non-linear crystal and measuring the second-harmonic light beam produced when the temporal delay between the two initial pulses is varied^[111–114]. As no crystals are available for the wavelength range of the harmonic emission (10–80 nm), a replacement has to be found that will produce a two-photon signal. The second-order non-linearity is a necessary condition to deduce the as-pulse duration. As it has been demonstrated in the first autocorrelation experiment of as-pulse trains^[101], the two-photon ionization process in gas is an appropriate alternative for this purpose^[115]. In the case of laser pulse, the region of the spatial overlap between the pulses is straightforward to image using an optical system from which the sought after information on the pulse duration can be extracted. In the scheme we propose, the corresponding signal that needs to be recorded with spatial resolution stems from the ions produced by two-photon ionization in the overlap region. The practicability of such a scheme has been demonstrated by Schultze et al.^[59], who used an “ion microscope” to retrieve the spatial distribution of ions generated in the laser focus via ionization of a target gas. In their study, the authors demonstrate a magnification of 100 for a field-of-view of 200x100 micrometers and a spatial resolution better than 4 micrometers. It should be emphasized that the resolution reported in Ref. [59] is the resolution of the particular experiments presented by the authors and does by no means represent an intrinsic limitation of the ion microscope resolution, which can, in principle, reach a sub-micron level. The reported 4 micrometer resolution rather results from the fact that the ion distribution shown in Ref. [59] was integrated over many laser shots and thus affected by beam-pointing fluctuations. Such beam pointing fluctuations, however, would play no role in the single-shot autocorrelation scheme presented here. Furthermore, by adjusting the appropriate voltages in the ion optic section, the field-of-view of the instrument and the corresponding spatial resolution can be optimized to meet the requirements of a specific measurement.

Although the proposed scheme requires high XUV pulse energies to produce an analyzable signal, it has in principle the great advantage of deducing the most pertinent information in a single shot. This makes it more suitable for use with sources delivering intense XUV fluxes such as the XFEL or harmonic emission from gas or solid targets in which TW laser systems and high conversion efficiency schemes are employed.

4.2 The concept

The method relies on the same principle employed in single-shot auto-correlation (SSAC) of pulses produced by lasers in the picosecond and subpicosecond time domains. The basic idea is to transform the temporal shape of the pulse into a spatial profile, which can be readily recorded and analyzed. The main differences here are that the setup has to be appropriate to handle XUV radiation and also capable of discerning a train of pulses. Therefore, the non-linear crystal should be replaced by an atomic gas where two-photon ionization processes can take place and the ionization products must be recorded in two dimensions. Analogous to alloptical setups, we assume that two non-collinear XUV beams comprising a group of harmonics of the fundamental laser frequency cross each other in the plume of a gas jet. For illustration, we assume that the two beams

are replicas of each other and emanate from two small openings at a distance d on the surface of a spherical mirror having focal length f (see Figure 4-1). Assuming that the harmonics in the group are in phase, the temporal profile of the XUV pulse will generally have strong modulations and form a train of sub-laser-cycle duration pulses. In space, this translates to narrow regions where the electric field is confined, as illustrated in Figure 4-1. The regions where the attosecond pulses of the train cross each other will propagate through the gas jet volume as long as the two XUV pulses overlap both spatially and temporally. A detector with imaging capabilities looking at the interaction region along a line of sight perpendicular to the plane defined by the two openings and the focus will record a series of lines parallel to the z -axis. Simple geometrical considerations lead to an expression for the distance a between these lines as:

$$\alpha = \frac{\lambda_0}{4 \sin \theta} \quad (4.1),$$

where $\theta = \arctan[d/(2f)]$ and λ_0 the wavelength of the fundamental laser frequency. In deriving this expression it was assumed that the harmonic emission emanates from an atomic medium. In this case only the odd harmonics are generated and as a consequence the sub-cycle pulses appear twice in every cycle of the fundamental frequency. For the plasma medium, the distance between the sub-cycle pulses would be λ_0 ^[16].

Let N_{ions} be the number of ions produced at the point x, y, z of the interaction region where the two incident pulses coincide both spatially and temporarily. If the ionization process of the gas atoms is occurring via two-photon transitions, N_{ions} is proportional to the square of the instantaneous total intensity $I_{tot}^2(x, y, z, t) = |\varepsilon_A(x, y, z, t) + \varepsilon_B(x, y, z, t)|^4 = |\varepsilon_{tot}(x, y, z, t)|^4$ prevailing at this point. Here ε_A and ε_B are the amplitudes of the interfering fields from the two sources on the spherical mirror. To obtain the auto-correlation signal from the number of ions produced, we follow the same intuitive picture presented in Reference [114], in conjunction with the second harmonic generation in a nonlinear crystal. This is depicted in the lower left inset of the Figure 4-1. For the present discussion, we assume that the two incident pulses have planar wavefronts and the gas density is spatially uniform. At each crossing of the sub-cycle pulses, the instantaneous number of ions $N_{ions} \approx I_{tot}^2 = |\varepsilon_A(t-\tau) + \varepsilon_B(t+\tau)|^4$ at a distance y_0 from its bisector depends on the delay between two different parts of the overlapping pulses (see lower left inset in Figure 4-1). The delay τ is related to the physical distance y_0 by $\tau = (y_0/c) \sin \theta$, where c is the velocity of light in the medium. The ion signal integrated over the XUV pulse width is proportional to the interferometric autocorrelation function S_{AC} of the incident pulse:

$$S_{AC}(x, y, z) \approx \int_{-\infty}^{\infty} |\varepsilon_A(t-\tau) + \varepsilon_B(t+\tau)|^4 dt \quad (4.2)$$

A spatially resolved ion signal of the interaction region with sufficient resolution reveals the most pertinent information about the XUV pulse in a single event. For example, provided the field-of-view encompasses the whole interference pattern, the number of attosecond pulses can be immediately deduced. Furthermore, all the information from an interferometric AC trace in the case of visible wavelengths is also available here, most importantly an estimate of the duration and possibly of the chirp of the generated attosecond pulses. Namely, if the spatial width of the fringe-averaged signal in the overlapping regions shown in Figure 4-1 is $\Delta y = c \cdot \tau_{AC}$, then the duration of the attosecond pulse would be:

$$\tau_{as} = \tau_{AC} \sin \theta \quad (4.3)$$

There is, nevertheless, a fundamental difference between this AC scheme and that employed in the

visible range using crystals. Because of momentum conservation, the second harmonic emission that is generated using crystals is produced along the bisector (observation) direction only in the regions where the beams cross each other in temporal coincidence inside the crystal, i.e., each beam by itself does not produce any signal in this direction. This gives the possibility of measuring the background-free single-shot AC signal. In the case of two-photon ionization, signal is produced wherever sufficient intensity is available, and therefore also in regions where only one beam is present. The background signal is indicated in Figure 4-1 and it will be quantified for specific cases in Paragraph 4.3.

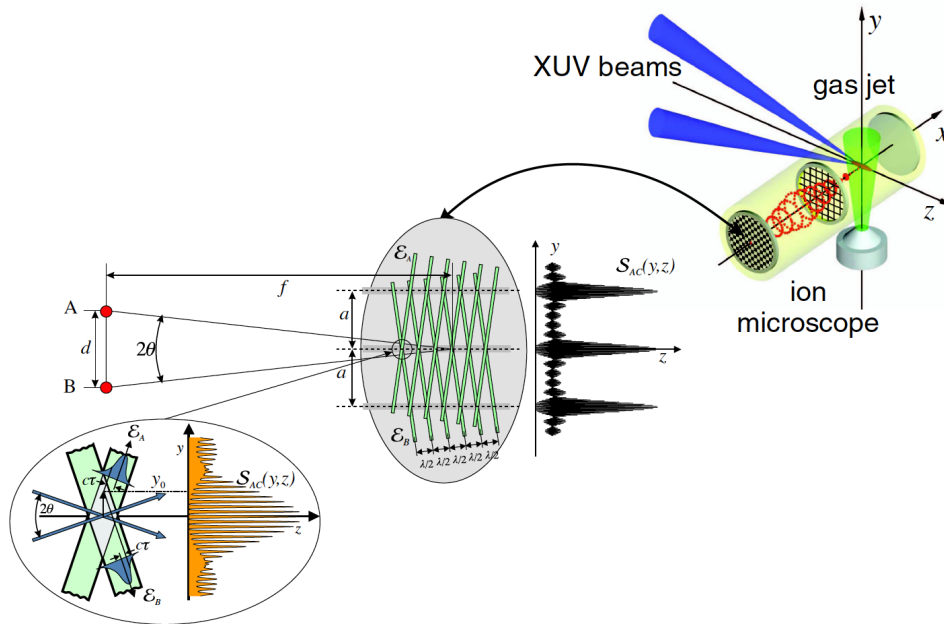


Figure 4-1 : Concept of the proposed SSAC scheme. In the upper right inset a schematic of the proposed setup is shown. The imaging ion microscope provides an image of the ionization products around the common focal spots of the intersecting XUV beams. In the lower left inset, the analogy to Single Shot AC using fs-laser pulses and crystals is indicated. Provided that a two-photon ionization occurs, the fringe pattern shown schematically is the second-order AC trace to be analyzed.

4.3 Model calculation

In this section, a simplified model is used to analytically investigate the main features of the interferometric auto-correlation function given in Equation (4.2). Two XUV beams consisting of N harmonics of the fundamental laser frequency ω_0 are assumed, each emanating from an aperture of diameter D on a spherical surface with focal length f . Due to focusing of the spherical mirror, they interfere within an angle θ at the focus (see Figure 4-2). To make the calculation tractable, first two plane waves are considered interfering at the focus of the spherical surface. The effect of focusing is taken into consideration in an ad hoc manner in the second step.

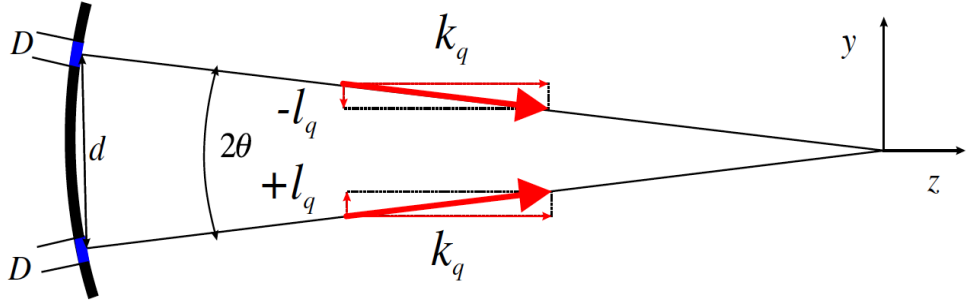


Figure 4-2 : Geometry considered in the model calculation.

Given the difference in the propagation vectors of the two plane waves indicated in Figure 4-2, the combined field due to the q_{th} harmonic from the two sources $E_q(y, z, t)$ at y - z plane is:

$$\varepsilon_q(y, z, t) = E_q [e^{j(l_q y + k_q z - \omega_q t)} + e^{j(-l_q y + k_q z - \omega_q t)}] = 2 E_q \cos(l_q y) e^{j(k_q z - \omega_q t)} \quad (4.4),$$

where E_q is the amplitude of the q_{th} harmonic, $k_q = q \frac{2\pi}{\lambda_0} \cos \theta$, $l_q = q \frac{2\pi}{\lambda_0} \sin \theta$, $\omega_q = q \omega_0$ and λ_0 is the fundamental wavelength. In the expression in Equation (4.4), the time delay τ between the two beams is indirectly included by the geometry via the dependence on the coordinate y . The total instantaneous intensity $I_{tot}(y, z, t)$ at the region where there is complete overlap will be:

$$\begin{aligned} I_{tot}(y, z, t) &= \sum_q \varepsilon_q(y, z, t) * \sum_p \tilde{\varepsilon}_p(y, z, t) = \\ &= \sum_q 2 E_q \cos(l_q y) e^{j(k_q z - \omega_q t)} * \sum_p 2 E_p \cos(l_p y) e^{-j(k_p z - \omega_p t)} = \\ &= 4 \sum_{q, p} E_q E_p \cos(l_q y) \cos(l_p y) e^{j[(k_q - k_p)z - (\omega_q - \omega_p)t]} \end{aligned} \quad (4.5).$$

The 1st order AC signal is proportional to the time-average intensity, i.e. to $\hat{I}_{tot} \propto \int_t^{t+T_0} I_{tot}(y, z, t) dt$, with T_0 the period of the fundamental wave. It is easily seen that terms containing the integral $\int e^{\pm j(q-p)\omega_0 t} dt$ will average to zero unless $q = p$. Retaining only the surviving terms one obtains:

$$\begin{aligned} \hat{I}_{tot}(y) &= 4 \sum_q E_q^2 \cos^2(l_q y) = \\ &= 4 \sum_q E_q^2 \cos^2\left(q \frac{\pi}{2} \frac{y}{\alpha}\right) \end{aligned} \quad (4.6).$$

As expected the time-average intensity pattern becomes independent of z . This justifies the picture presented in Figure 4-1, i.e., in a 2-D ion image of the interaction region by a time integrating detector, the lines along which the crossing points of the attosecond pulses propagate would appear as stripes.

The 2nd order AC signal is proportional to the average value of the square of the time dependent intensity. Therefore, the intensity should be squared before the time average value is calculated, i.e., one should start from the following expression:

$$\begin{aligned}
I_{tot}^2(y, z, t) &= \left[\sum_q 2E_q \cos(l_q y) e^{j(k_q z - \omega_q t)} * \sum_p 2E_p \cos(l_p y) e^{-j(k_p z - \omega_p t)} \right]^2 \\
&= 2^4 \left[\sum_{q,p} E_q E_p \cos(l_q y) \cos(l_p y) e^{j(k_q - k_p)z - (\omega_q - \omega_p)t} \right]^2 = \\
&= 2^4 \sum_{q,p,n,m} E_q E_p E_n E_m \cos(l_q y) \cos(l_p y) \cos(l_n y) \cos(l_m y) e^{j(k_q - k_p + k_n - k_m)z - (\omega_q - \omega_p + \omega_n - \omega_m)t}
\end{aligned} \tag{4.7}$$

Using the multiple sum in the last expression of Equation (4.7), the time average of each term can be calculated. Again taking into consideration that terms now containing the integral $\int e^{\pm j(q-p+n-m)\omega t} dt$ will average to zero unless $q-p+n-m = 0$, one obtains for the 2nd order AC signal as:

$$\begin{aligned}
\hat{I}_{tot}^2(y) &= 2^4 \sum_{q,p,n,m} R_{q,p,n,m} E_q E_p E_n E_m \cos(l_q y) \cos(l_p y) \cos(l_n y) \cos(l_m y) = \\
&= 2^4 \sum_{q,p,n,m} R_{q,p,n,m} E_q E_p E_n E_m \cos\left(q \frac{\pi y}{2 \alpha}\right) \cos\left(p \frac{\pi y}{2 \alpha}\right) \cos\left(n \frac{\pi y}{2 \alpha}\right) \cos\left(m \frac{\pi y}{2 \alpha}\right)
\end{aligned} \tag{4.8}$$

where $R_{q,p,n,m} = 1$ for $q+p-n-m = 0$ and $R_{q,p,n,m} = 0$ otherwise. The factor $R_{q,p,n,m}$ is introduced to take into consideration the effect of time averaging. It is interesting to note that the last result is not obtained by simply squaring the time average intensity in Equation (4.6).

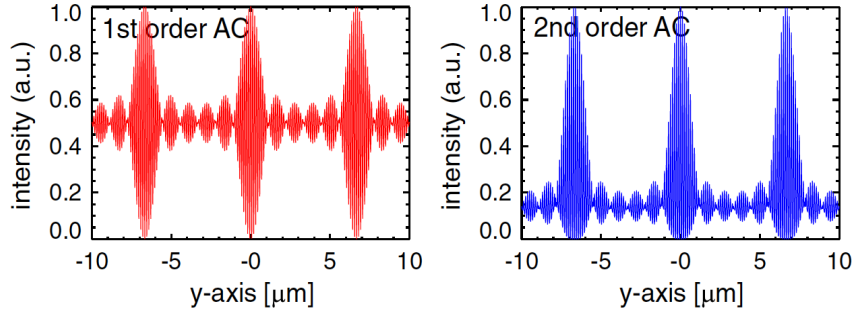


Figure 4-3: Plot of the expression in Equation (4.6) and Equation (4.8) for a group of equal amplitude odd harmonics between $q=101\dots111$ and for $f=5$ cm, $d=0.3$ cm and $\lambda=800$ nm.

To illustrate the behavior of the interference pattern and the form of the 1st and 2nd AC trace we consider a specific example. For a group of odd harmonics in the range $q_a = 101$ to $q_b = 111$ and for $f = 5$ cm, $d = 0.3$ cm and $\lambda = 800$ nm the last expressions in Equation (4.6) and Equation (4.8) are plotted in Figure 4-3. For these parameters the distance between the crossings of the attosecond pulses is $a \simeq 6.7 \mu\text{m}$. It is seen that while the 1st order AC is symmetric around an average value, the 2nd order AC exhibits the typical auto-correlation behavior with a signal-to-background ratio of $\sim 8 : 1$ as in the case of single frequency interferometric AC. The fine structure inside each peak is due to the interference of the individual harmonics. It is to be noted here that the choice of the specific group of harmonics (H101-H111) is judicial to better demonstrate the features of multi-frequency AC traces. In the following paragraphs a more realistic case of lower harmonics in the range H9-H15 is considered.

Up to now the diffraction due to the apertures on the mask has not been taken into account. We now assume uniform illumination over the area of the opening having radius $R = D/2$. As each source is located on the surface of a focusing mirror, the focal spot will then be an Airy pattern. For waves having a wavelength λ_0 the pattern at the focal plane is (see Reference: [80]):

$$I(y) = \left[\frac{2 J_1(v)}{v} \right]^2 \quad (4.9),$$

where $v = \frac{2\pi}{\lambda_0} \frac{R}{f}$ with $r = \sqrt{x^2 + y^2}$. Thus, the timeaverage intensity for a group of harmonics in Equation (4.6) is modified as follows:

$$\hat{I}_{tot}(y) = 4 \sum_q \left[E_q \frac{2J_1(v_1)}{v_1} \cos(u_q) \right]^2 \quad (4.10),$$

where $u_q = q \frac{2\pi}{\lambda_0} y \sin \theta = q \frac{\pi}{2} \frac{y}{a}$ and $v_q = q \frac{2\pi}{\lambda_0} \frac{R}{f} r$. Similarly, the second order AC signal in Equation (4.8) becomes:

$$\begin{aligned} \hat{I}_{tot}^2(y) = & 2^8 \sum_{q,p,n,m} R_{q,p,n,m} E_q E_p E_n E_m * \\ & * \frac{J_1(v_q)}{v_q} \cos(u_q) \frac{J_1(v_p)}{v_p} \cos(u_p) \frac{J_1(v_n)}{v_n} \cos(u_n) \frac{J_1(v_m)}{v_m} \cos(u_m) \end{aligned} \quad (4.11),$$

where $R_{q,p,n,m} = 1$ for $q+p-n-m = 0$ and $R_{q,p,n,m} = 0$ otherwise.

The last expressions in Equation (4.10) and Equation (4.11) for $D = 100 \mu\text{m}$ are plotted in Figure 4-4 for the same geometrical parameters as in the previous example, yet with group harmonics of $q = 9 \dots 15$. This harmonic selection is technically feasible and ensures two-photon ionization in conjunction with He atoms^[101,103]. The fine structure seen in Figure 4-4, is due to interference of the light from the two apertures while the overall shape is determined by diffraction through a single aperture (Airy pattern). Thus, the signal area is limited by the Airy spot size resulting at the focus of the spherical mirror and is given by $R_{Airy} \approx 1.22 f \lambda_{q0} / D \approx 54.2 \mu\text{m}$ with q_0 the lowest harmonic in the selection. In order to be able to deduce e.g., whether a single attosecond pulse is produced or not, at least three sub-cycle peaks should fit in the observable area. This imposes the condition $R_{Airy} \geq a$. The smaller the diameter D of the apertures the larger the Airy radius. This however drastically reduces the XUV intensity at the focus. Alternatively, one can increase the distance d of the two apertures to obtain shorter distance a between the peaks. The drawback then is that a higher spatial resolution is required to adequately resolve the peaks. As a consequence for optimum operation, a compromise in the selection of the apertures diameter and their distance should be carefully made (see discussion in Section 4.5).

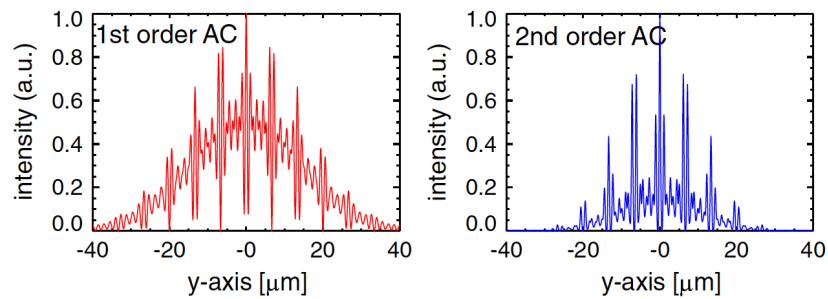


Figure 4-4: Plot of the expression in Equation (4.10) and Equation (4.11) for $q = 9 \dots 15$ and equal amplitudes. The geometry parameters are the same as in Figure 4-3.

4.4 Setup optimization

In this section we perform a detailed study to determine the optimum arrangement for the use of the Single Shot Auto-Correlation (SSAC) device in conjunction with attosecond light sources. The objective is to determine the geometry as to achieve the maximum possible throughput and the best resolution. To be able to consider quite general but realistic cases we apply the formulation presented in Reference [80] for the diffraction integral at the focus of a spherical converging wave. We then consider various masks or geometries for the spherical mirror from where the converging wave emanates.

4.4.1 Calculation of the diffraction integral

The starting point is the expression given in Reference [80] for the calculation of the three-dimensional monochromatic light distribution near focus, namely:

$$U_{tot}(P) \propto \iint_W \frac{e^{j[k_0(s-f)]}}{s} dS \quad (4.12),$$

where $k_0 = 2\pi / \lambda_0$ and λ_0 the wavelength of the converging wave. The point Q with coordinates x_Q, y_Q, z_Q is located on the mirror surface W and P is the observation point with coordinates x_P, y_P, z_P both with respect to a system centered at the focus of the spherical wave. The distance s between the two points Q and P determining the phase factor is derived from:

$$s^2 = (x_P - x_Q)^2 + (y_P - y_Q)^2 + (z_P - z_Q)^2.$$

To apply the method to our case one has to consider three notable differences:

1. The illumination from the spherical surface is restricted to two apertures through an appropriate mask.
2. The illumination is not monochromatic, i.e., there are contributions from a group of harmonics.
3. The time dependence can not be factored out.

In this case the diffraction integral has to be modified as follows:

$$U_{tot}(P, t) \propto \iint_W M(Q) \sum_q e^{j[k_q(s-f) - \omega_q t]} dS \quad (4.13),$$

where $k_0 = 2\pi / \lambda_0$ and $\omega_q = q \omega_0$, $M(Q)$ is the mask on the spherical surface and the sum runs over the harmonic numbers in the group.

If $q = 1$, i.e., monochromatic illumination, then the time dependent factor can be taken out of the integral and the time average intensity is simply $\hat{I}_{tot} \propto U_{tot} \tilde{U}_{tot}$. In the case of a harmonic synthesis, the situation is more complicated. The different frequencies give rise to temporal beating (attosecond pulse train) and over a period the variation is not simply $\propto \cos(\omega t)$. For this reason the evaluation of the time average intensity in case of a group of harmonics needs special attention. The diffraction integral in this case can be written as:

$$U_{tot}(P, t) \propto \sum_q U_q e^{-j\omega_q t} \quad (4.14),$$

where: $U_q = \iint_W M(Q) e^{j\mathbf{K}_q \cdot (\mathbf{s} - \mathbf{f})} dS$.

In analogy to Equation (4.5) the corresponding instantaneous total intensity $I_{tot}(x, y, z, t)$ is given by:

$$\begin{aligned} I_{tot}(x, y, z, t) &\propto \sum_q U_q e^{-j\omega_q t} * \sum_p \tilde{U}_p e^{+j\omega_p t} \\ &\propto \sum_{q,p} U_q \tilde{U}_p e^{-j(\omega_q - \omega_p)t} \end{aligned} \quad (4.15),$$

The time average can now be calculated, and using the same argument for the cross terms as in Equation (4.5) one obtains:

$$\hat{I}_{tot}(x, y, z) \propto \sum_q U_q \tilde{U}_q \quad (4.16),$$

The 2nd order AC signal will be proportional to:

$$\begin{aligned} I_{tot}^2(x, y, z, t) &\propto \left[\sum_{q,p} U_q \tilde{U}_p e^{-j(\omega_q - \omega_p)t} \right]^2 \text{ and thus to} \\ \hat{I}_{tot}^2(x, y, z) &\propto \sum_{q,p,n,m} R_{q,p,n,m} [U_q U_p \tilde{U}_n \tilde{U}_m] \end{aligned} \quad (4.17),$$

where $R_{q,p,n,m} = 1$ for $q+p-n-m = 0$ and $R_{q,p,n,m} = 0$ otherwise.

In what follows we apply these formulas to numerically calculate the second-order AC signal for various masks of practical interest.

4.4.2 Two-aperture mask

As a first example we consider a mask in which two pinholes select a small portion of the XUV beam incident on a spherical mirror. The XUV profile is assumed to be Gaussian with a FWHM waist of $2r_b = 3.0$ mm while the mask geometrical dimensions are the same as those considered for the analytical model in Section 4.3. The XUV profile and the mask are shown in Figure 4-5 along with the patterns in two planes of the 2nd order AC trace. Comparing the line-out along the y -axis of the focal plane pattern obtained through the numerical evaluation of the diffraction integral in Equation (4.17), it is seen that is identical to the one from the analytical model shown in Figure 4-4. This is to be expected since the intensity variation over the pinhole openings of the Gaussian beam and the focusing effect of the converging wave are negligible. The agreement constitutes a reliable confirmation for the validity and correctness of the numerical method based on the diffraction integral.

According to the basic concept of the SSAC device, the pattern in the y - z plane shown in Figure 4-5 contains the information that needs to be recorded. For the specific geometry considered, its

relevant dimensions are quite accessible to measurements assuming a sub- μm resolution capability of the ion microscope to be used. However, due to the large axial extent of the focus, the XUV intensity might not be high enough to produce two-photon ionization. In addition, the two-aperture mask is very inefficient as it exploits a very small part of the incident XUV beam.

4.4.3 Two-slit mask

An alternative setup in which a better use of the available XUV energy is made is the two-slit mask. In this configuration instead of two pinholes there are two slits with width equal to the diameter of the pinhole in the previous example but of length extending over the whole XUV beam profile. This mask is shown in Figure 4-6. The effect is that the focal pattern in the y - z plane and x - y plane has much smaller extent in the x - and z -direction but in the y -direction remains the same. This is depicted in Figure 4-6 where the 2nd order AC signal is shown as calculated for this mask using Equation (4.17). As expected, the line-out of the signal along the y -axis in this case is identical to the one from the previous one. An assessment of the factor gained in intensity using this mask is given in Section 4.5.1.

4.4.4 Beam splitter

In both setups discussed in Paragraph 4.4.2 and Paragraph 4.4.3 it is obvious that in order to obtain an interaction region large enough to record sufficient information, the majority of the XUV energy is lost. This is primarily imposed by the requirement of dispersing the interference pattern to an extent that an ion microscope can "see" the details, i.e., the beats in the focus of the crossed beams. Still, these setups are applicable if the XUV source to be characterized is intense enough and the recording ion microscope possesses adequate resolution. In this section we investigate an alternative setup that would be more appropriate for relatively weak XUV sources. It is based on the wavefront splitting technique and it is shown schematically in Figure 4-7. As no conventional beam splitters exist for XUV radiation, the wavefront, instead of the amplitude of the beam, is divided into two. This can be easily achieved by using a wedge out of proper material as depicted in Figure 4-7. For example, Si exhibits for nearly grazing angle of incidence ψ very high reflectivity and for a wide spectral range (see Figure 4-7.(c)). Furthermore, if the angle of incidence is chosen equal to the Brewster angle $\theta_B(\text{Si}) \simeq 75^\circ$ for $\lambda = 800 \text{ nm}$ and parallel polarization, the same component can be used to substantially suppress the fundamental laser frequency.

After splitting the beam into two, an optical arrangement can be used to cross and focus the two beams under a given angle θ thus generating an interference pattern within a gas jet where the two-photon ionization takes place. We show two possible arrangements: one involving nearly perpendicular reflection and therefore limited to low order harmonics (Figure 4-7(a)) and another employing grazing incidence optics, more appropriate for high-order harmonics (Figure 4-7(b)). The first option imposes the condition $\theta \geq \pi - 2\psi$ while the second has the advantage of independently choosing θ and ψ but is more demanding in bringing the focus of the two beams to coincidence. These schemes have the advantage that the total XUV energy after reflection off a wedge is focused in the gas medium. The main drawbacks are the reflection losses on the wedge and the small focus due to large illumination aperture.

For reasons of comparison we use the same experimental parameters as in the previous examples, i.e., the same group of harmonics $q = 9 \dots 15$ of equal amplitudes and Gaussian XUV beam with a FWHM waist of $2r_b = 3.0 \text{ mm}$. This corresponds to an $1/e^2$ waist of $w_b = \sqrt{2 \ln 2} r_b = 2.5 \text{ mm}$. The

beam however is divided into two equal portions which subsequently are focused by a single optical component and cross each other at their focus. Since in this configuration the illuminated aperture is much larger compared to the previous cases, the condition $w_b \geq a$ necessary to observe more than one attosecond beat at the focus is not satisfied for the same focal length. To compensate for this, the focal length of the spherical mirror must be increased. We choose $f = 100$ cm and an angle $\theta = 2^\circ$. In this case $a = 5.7$ μm and $d = 70$ mm. The focal extent along the y -direction is estimated from $w_{0,y} \approx f \lambda_9 / (\pi w_b) \simeq 22.2$ μm with $w_b = w_b/2$. Here, we consider the focal extent of the $q = 9$ harmonic, i.e., of the longest wavelength and we take the waist of the half beam to be approximately half of the original waist. Accordingly, the focal extent in the x -direction is $w_{0,x} \approx f \lambda_9 / (\pi w_b) \simeq 11.1$ μm . The results of the numerical integration of the diffraction integral in Equation (4.17) are shown in Figure 4-8. It is seen that the estimates of the focal extent agrees very well with the results of the calculation. For the chosen experimental parameters, a readily resolved pattern comprising at least three attosecond beats is produced. The spatial extent (FWHM) of the central peak is $\Delta y \approx 2$ μm which corresponds to $\tau_{as} = \sin \theta \cdot \Delta y / c \simeq 230$ as, which is indeed the duration of the individual attosecond pulses in the train formed by the H9-H15 harmonics if they are phase locked and of equal amplitude.

A variation of the beam splitter method is the use of a split mirror in which the two parts are tilted with respect to the propagation axis. This way a magnified interference pattern is obtained just before the focus. The disadvantage of this setup is that, for realistic conditions, the region to be recorded is located close to the foci of the two half-beams. This would make the weak signal of the AC pattern difficult to distinguish from the signal due to the high intensity prevailing at the foci of the two half-beams.

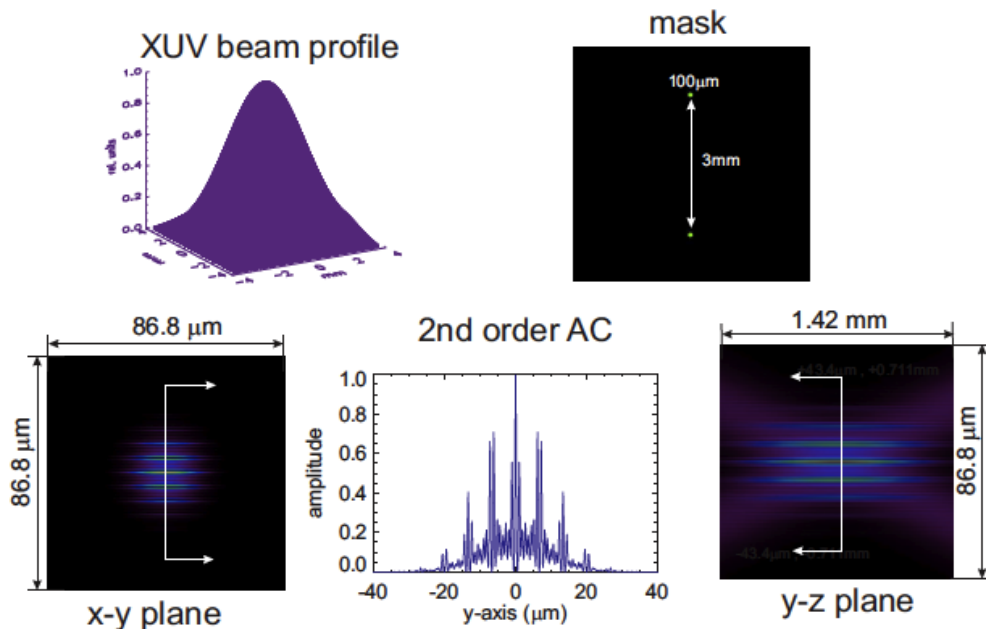


Figure 4-5: The second-order AC pattern due to the interference of the harmonic radiation emanating from two aperture of 100 μm in diameter. **Upper panels:** The profile of the converging XUV beam and the mask imposed to it. **Lower panels:** The 2nd order AC pattern in the two planes around the XUV focus as obtained from the numerical evaluation of Equation (4.17). The geometry parameters and the harmonic selection are the same as in Figure 4-4. ($q = 9 \dots 15$ and equal amplitudes).

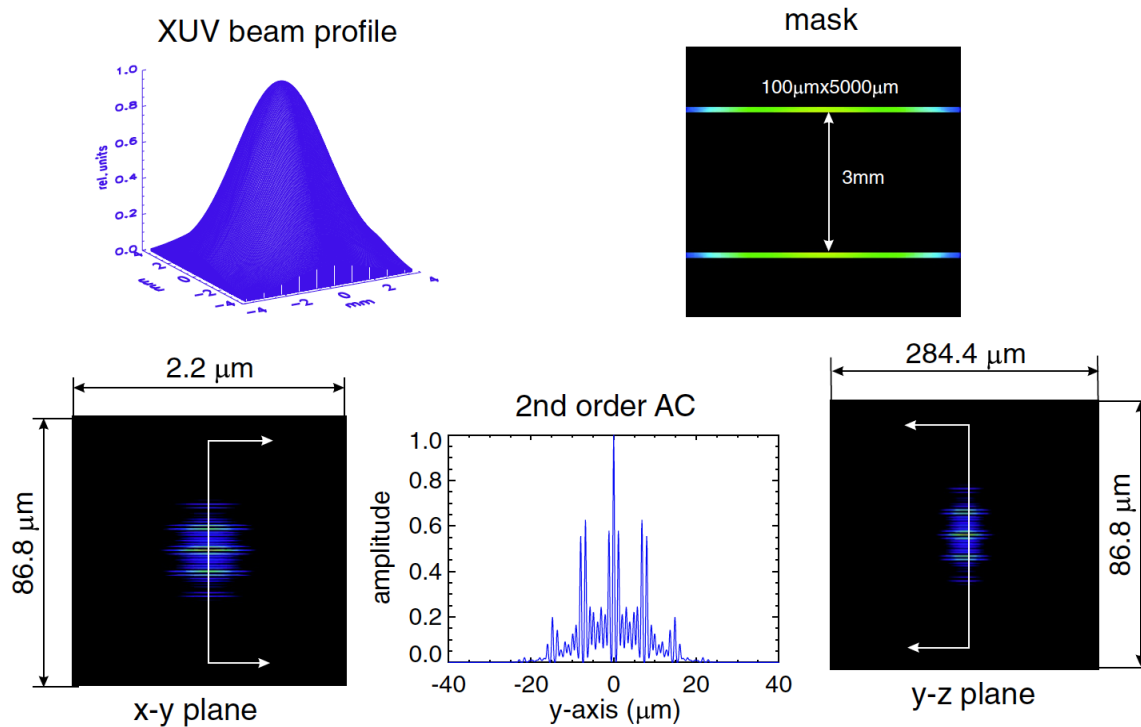


Figure 4-6 : The second-order AC pattern due to the interference of the harmonic radiation emanating from two slits of 100 μm wide and 5 mm long. **Upper panels:** The profile of the converging XUV beam and the mask imposed to it. **Lower panels:** The 2nd order AC pattern in the two planes around the XUV focus as obtained from the numerical evaluation of Equation (4.17). The geometry parameters and the harmonic selection are the same as in Figure 4-4. ($q = 9 \dots 15$ and equal amplitudes)

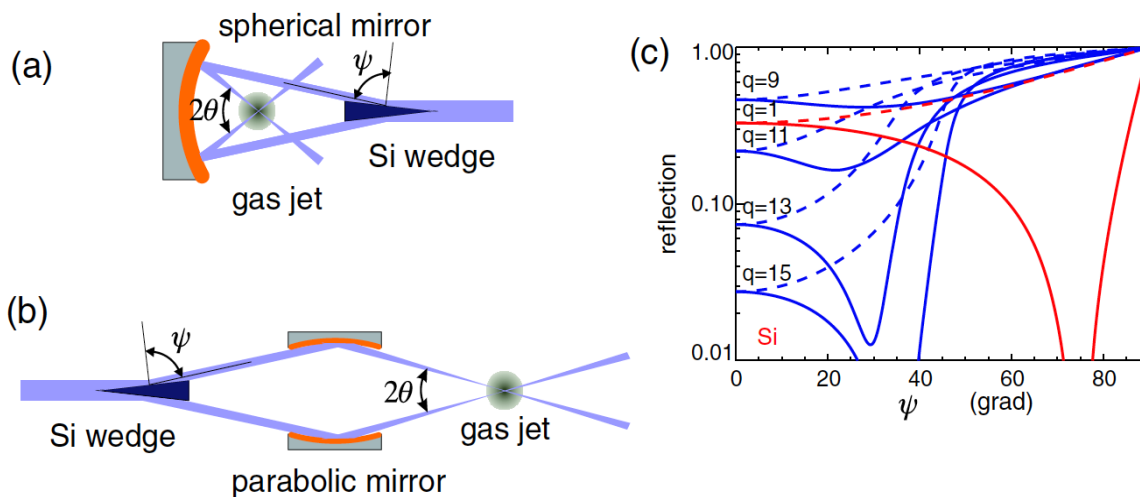


Figure 4-7 : Schematic diagrams of two possible setups for a cross-beam arrangement. **(a)** Setup for low order harmonics (long wavelength XUV emission) and **(b)** for higher order harmonics (short wavelength XUV emission). **(c)** The reflectivity of Si as a function of angle of incidence for parallel (solid line) and perpendicular (dashed line) polarization and for the indicated harmonic orders q .

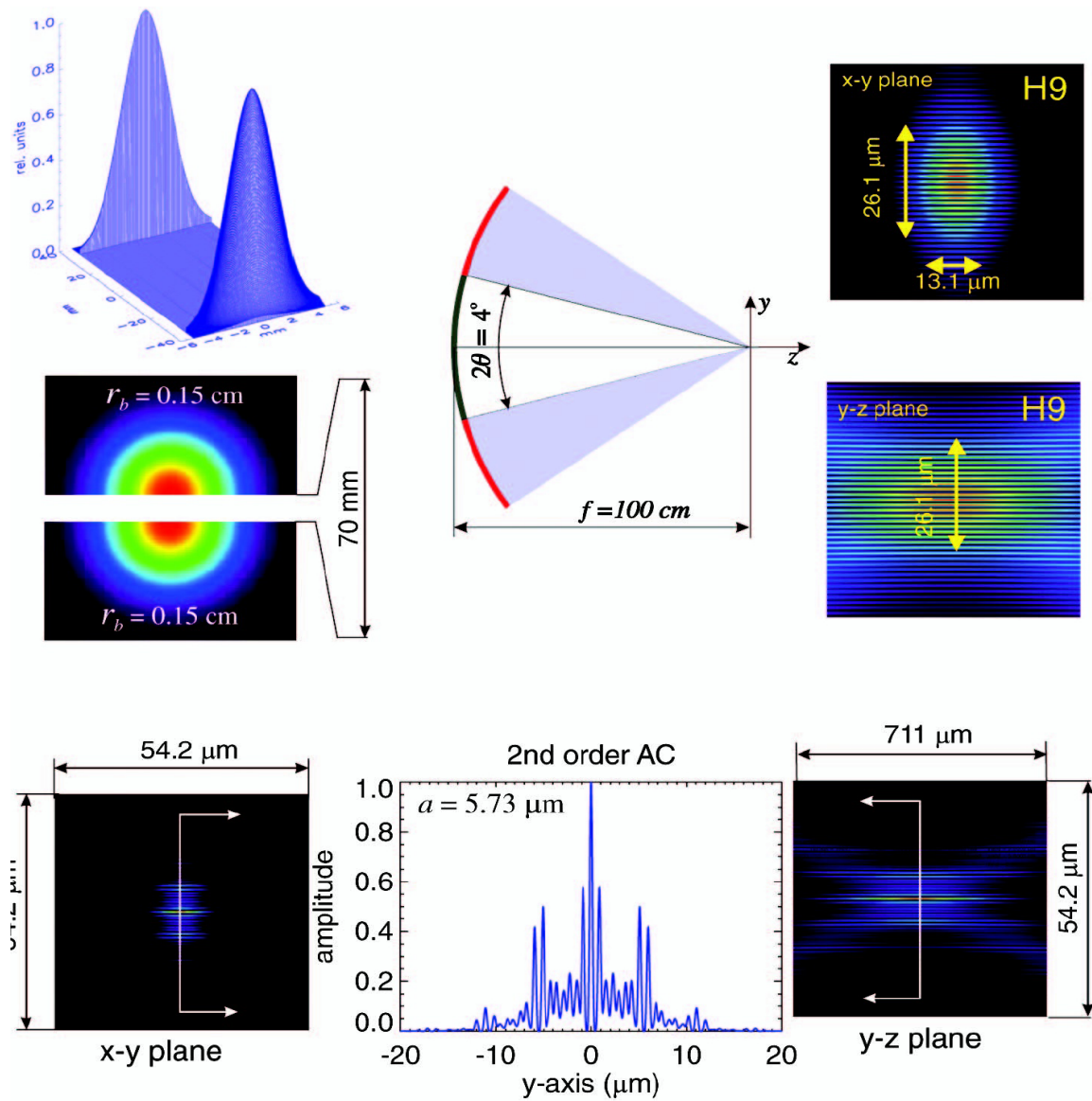


Figure 4-8 : Numerical calculation of the a cross-beam arrangement using a wavefront beam splitter. **The upper panel** shows the illumination geometry and the interference pattern for the H9 harmonic at the focus. The FWHM extent of the focal spot in the two directions is also indicated. **The lower panel** shows the 2nd order signal due to two-photon ionization by the harmonic group of H9-H15. The pattern in the y - z plane is what an ion microscope with enough resolution would record.

4.5 Setup assessment

The criteria on which the most appropriate setup can be chosen depend mainly on two experimental parameters: (a) the spatial resolution of the ion-microscope Δs and (b) the maximum XUV power P_{XUV} available by the source. The given spatial resolution determines the minimum size of the interaction region required to discern enough details to extract the pertinent information. On the other hand, larger interaction region means lower XUV intensity in which case the two-photon process rapidly becomes less efficient and as a result the corresponding signal rapidly deteriorates. It becomes apparent that for a given values of these two parameters, one must carefully navigate through the remaining parameters such as type of mask or arrangement, spherical mirror focal length and angle of intersection in order to obtain the most suitable setup. In what follows we discuss the advantages and disadvantages of each of the setups we have considered and point out the interplay of the various parameters.

4.5.1 Efficiency comparison

Since the application envisaged is based on a two-photon process, it is of outmost importance to examine the efficiency of the overall setup so that an estimate of the achievable intensity can be made. Previous experiments^[101,103,106] have shown that an XUV intensity of $I_{XUV} \geq 10^{11} \text{W/cm}^2$ is needed for recording a volume AC trace. In the scheme we propose here the signal is not spatially integrated as in previous experiments, but a 2-D image of the ionization products is required to deduce the sought after information. This increases the minimum XUV intensity needed for recording an analyzable signal, by at least a factor of 100. It is therefore essential to examine the efficiency of each arrangement we have considered. Here we compare, from the point of view of the mean intensity in the intersection volume, the three different implementations of this autocorrelation method we have discussed so far, i.e.

- (a) Using a mask with two apertures of diameter $D = 100.0 \mu\text{m}$ in a distance of $d = 3.0 \text{ mm}$ from each other on a Gaussian beam with an $1/e^2$ waist of $2w_b = 5.0 \text{ mm}$ and a spherical mirror of 5 cm focal length. (see Paragraph 4.4.2)
- (b) Using a mask with two slits of dimensions $1 \text{ cm} \times 100 \mu\text{m}$ in a distance of 3 mm from each other. (see Paragraph 4.4.3)
- (c) Using a beam splitter (Si-wedge) for the wavefront splitting of the incoming beam into two parts. In order to make them converge and intersect, we use a mirror of $f = 100 \text{ cm}$ focal length. (see Paragraph 4.4.4)

To meaningfully compare the three alternative configurations we assume that in all 3 cases an XUV power P_{XUV} is available and estimate the mean intensity that this power can produced in the interaction volume for each case. Subsequently, we obtain a **Figure of Merit F** as the ratio of the mean intensity achieved at the focal region in each of the arrangements to a reference intensity I_0 . We choose as reference intensity the one obtained by the spherical mirror assumed in the two-aperture and two-slit arrangements but without any mask.

For a Gaussian beam profile, the intensity variation along the z -axis of propagation and in the transverse r -plane is: $I(r, z) = \frac{2P_{XUV}}{\pi w^2(z)} \exp\left[-\frac{2r^2}{w^2(z)}\right]$. Here $w(z) \approx \theta_0 z$ is the waist radius far from focus and $2w_0 = 2\lambda/\pi\theta_0$ the focal spot size. The angle of convergence is estimated from $\theta_0 \approx \arctan(w_b/f)$ where $w_b = w(z=f) = \sqrt{2/\ln 2} r_b$ with r_b the initial beam radius and f the

focal length of the spherical mirror. The focal mean intensity is easily seen to be $I_0 = P_{XUV} / (\pi w_0^2)$. We now estimate F for each of the concrete cases (a)-(c).

(a) At the position of the apertures the intensity is reduced and therefore the power transmitted through each pinhole is:

$$P_{apt} = I(d/2, f) \frac{\pi D^2}{4} = \frac{2 P_{XUV}}{\pi w_b^2} \exp\left[-\frac{d^2}{2 w_b^2}\right] \frac{\pi D^2}{4} \quad (4.18).$$

Given the small dimensions of the aperture, a flat-top distribution can be assumed, which gives rise to an Airy pattern at the focus. The radius of the central disk is then $R_{Airy} \approx 1.22 f \lambda_{q0} / D \approx 54.2 \mu\text{m}$ with $q_0 = 9$ the lowest harmonic in the selection. The mean intensity achieved in this case is then:

$$I_{mean} = 2 \frac{P_{apt}}{\pi R_{Airy}^2} \quad (4.19).$$

The corresponding figure of merit for the concrete example we have considered is $F_a = I_{mean}/I_0 \approx 8 \cdot 10^{-8}$.

(b) The power through each slit with dimensions $l_x = 1\text{cm}$ and $l_y = 100\mu\text{m}$ in this case is:

$$\begin{aligned} P_{slit} &\approx \frac{2 P_{XUV}}{\pi w_b^2} \exp\left(-\frac{d^2}{2 w_b^2}\right) l_y \int_{-l_x/2}^{+l_x/2} \exp\left(-\frac{2x^2}{w_b^2}\right) dx \\ &\approx \frac{2 P_{XUV}}{\pi w_b^2} \exp\left(-\frac{d^2}{2 w_b^2}\right) l_y \sqrt{\frac{\pi}{2}} w_b \end{aligned} \quad (4.20).$$

The pattern at the focus will be elliptical with approximate dimensions $L_x \approx 2 * 1.22 f \lambda_{q0} / l_x \approx 1.1 \mu\text{m}$ and $L_y \approx 2 * 1.22 f \lambda_{q0} / l_y \approx 108.0 \mu\text{m}$. Thus the mean intensity at focus follows as:

$$I_{mean} = 2 \frac{P_{slit}}{L_x L_y} \quad (4.21).$$

As expected the figure of merit for the two slit arrangement increases greatly and is found to be $F_b \approx 2.5 \cdot 10^{-4}$.

(c) In the case of the beam splitter, the only difference from using the whole beam is the splitting of the Gaussian profile into two halves. A rough estimate of the mean intensity at focus from each half can be made using the same arguments as in case (b). The power from each half with dimensions $l_x \approx w_b$ and $l_y \approx w_b / 2$ in this case is simply $P_{XUV} / 2$. Accordingly, the mean intensity at focus is:

$$I_{mean} = \frac{P_{XUV}}{L_x L_y} \quad (4.22).$$

As it was already discussed in Paragraph 4.4.4, the pattern at the focus will be elliptical with approximate dimensions $L_x \approx 2f\lambda_{q0}/(\pi l_x) \simeq 22.2 \mu\text{m}$ and $L_y \approx 2f\lambda_{q0}/(\pi l_y) \simeq 44.2 \mu\text{m}$ for $f = 100 \text{ cm}$ and $q_0 = 9$. The corresponding FWHM values of the elliptical spot $2r_{0,x} \simeq 13.1 \mu\text{m}$ and $2r_{0,y} \simeq 26.2 \mu\text{m}$ are very close to the exact numerical results for the focal spot of H9 shown in Figure 4-8. The figure of merit for the beam splitter arrangement is as expected the highest $F_c \simeq 1.0 \cdot 10^{-3}$.

In case (c) we have not included the reflection losses on the intervening beam splitter. For relative low order harmonics, the diagram in Figure 4-7.(c) indicates that they can be quite low. However in a realistic case, one should consider a loss factor of up to 10, especially if the group of harmonics is comprised of high orders. These losses nevertheless are also present in the other setups ((a) and (b)) as for most of the applications a stage for the suppression of the IR light is required. In this arrangement, the necessity of having long focal length to encompass at least 3 attobeats in the focus results in lower XUV intensity, in the specific example by a factor of $\simeq 400$, but this is compensated by the large apertures (half the XUV beam profile) used. This makes the beam splitter most efficient and in addition the sampling area of the XUV beam profile is more representative of the whole beam in this case.

4.5.2 Parameter selection

From the previous discussion in Paragraph 4.5.1 it becomes apparent that one of the most efficient setups is the beam-splitter arrangement. Given the maximum resolution Δs associated with the ion-microscope, there are two important parameters that will have to be appropriately chosen. They are the angle θ at which the beams intersect each other and the focal length f of the focusing mirror. The angle θ determines the distance a between the attosecond beats [see Equation (4.1)] whereas the focal length defines the focal spot size and therefore the number of attosecond beats it encompasses. To illustrate this interplay we have used Equations (4.10) and (4.11) to calculate the 1st and 2nd order AC for a number of combinations of f and θ values. Instead of assuming a flat-top intensity profile at the source we have assumed Gaussian intensity distribution. This results in replacing the Bessel function in Equations (4.10) and (4.11) with a Gaussian function having the same argument. The rest of the parameters are the same as in the example shown in Figure 4-8 except that for simplicity two complete Gaussian beams are assumed instead of two halves. The results are shown in Figure 4-9 along with the modification of the signal assuming a spatial resolution of $\Delta s = 2 \mu\text{m}$.

There two distinct substructures in the 1st and 2nd order signals. The finer modulation represents the oscillations resulting from the superposition of the harmonic waves while the coarser is due to the beating of these waves giving rise to spatial localization i.e., to the formation of attosecond pulses. It is seen that under finite resolution conditions, the substructure in the 1st order signal disappears to a large extent where, for the 2nd order signal the substructure after the convolution with the instrument function prevails in most of the cases. For $f = 100 \text{ cm}$ and $\theta = 2^\circ$, three attosecond beats are contained in the focal spot as was also obtained by the numerical calculation shown in Figure 4-8. The signal blurring due to finite resolution of the instrument is depicted by the gray shaded curve. In this case the three attosecond peaks are still discernible but the oscillations within the attosecond wave beating disappear and the peak to background ratio is greatly reduced. Despite that, the duration of the peak in the middle of the 2nd order AC trace can be retrieved by careful deconvolution of the signal with the instrument function. For $f = 50 \text{ cm}$ and $\theta = 2^\circ$, the focal spot is half as large, and one cannot be sure whether the middle peak is affected by the focal spot size (see Figure 4-9(b)). For $f = 100 \text{ cm}$ and $\theta = 1^\circ$, the middle peak is spread out to the point of seeing the oscillations within the attosecond beating but the focal spot size cannot accommodate

satellite peaks (see Figure 4-9(c)). This is required to verify the existence of a single attosecond pulse. In contrast, the case illustrated in Figure 4-9(d), corresponding to $f = 100$ cm and $\theta = 5^\circ$, exhibits a number of satellite peaks but due to finite resolution they are smeared out and thus hardly discernible.

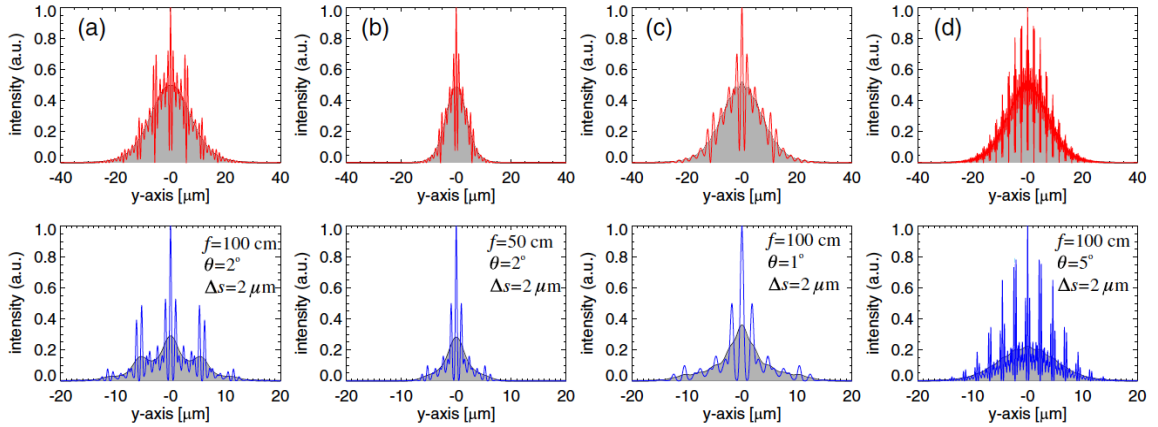


Figure 4-9 : Numerical calculation of the cross-beam arrangement using a wavefront beam-splitter for the indicated combinations of focal lengths f and angles of intersection θ . The upper panel shows the first-order AC trace while the lower the second-order. The apparent signal assuming a spatial resolution of $\Delta s = 2 \mu\text{m}$ is shown as gray shaded area.

It is to be noted here that if the signal level allows it, a complete record of the 2nd order signal in the y - z plane like the one shown in the lower panel of Figure 4-8 can provide some of the most pertinent information even for finite resolution. A line-out of the signal along the axis of propagation of one of the beams contains the spatial characteristics of the beating structure and provides a substantial magnification. It is easily deduced that the modulation period of the attosecond beating in this case is: $a' = \lambda_0 / (4 \sin^2 \theta)$, which for small angles θ is considerably larger than the one given by Equation (4.1). As the instrument resolution is the same over the whole field of view, such a projection might provide a clearer picture of the information sought after, e.g. whether a single or multiple as-pulses are present. This is depicted in Figure 4-10 where the case studied in Paragraph 4.4.4 using the beam-splitter is shown smoothed to a degree corresponding to $\Delta s = 2 \mu\text{m}$. It is seen that a line-out along the axis of propagation of one of the beams exhibits the multiple as-pulse structure. Clearly, it furnishes no additional information compared to a line-out perpendicular to the z -axis but provides considerable magnification.

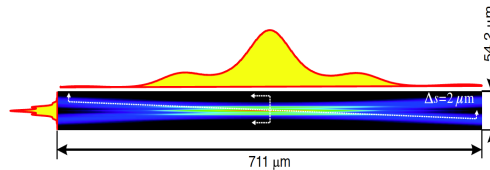


Figure 4-10 : Analysis of the 2D image of the beam-splitter case described in Paragraph 4.4.4 for an instrument resolution of $\Delta s = 2 \mu\text{m}$. The image has been smoothed to a degree corresponding to the finite instrument resolution and scaled to actual proportions. The line-outs along the axis of propagation of one of the beams and transverse to the z -axis are shown by the red yellow filled line.

4.5.3 Ionization estimates

In order to establish to what extent the ion microscope, described at length in Reference [59], can record details of the focal region, we calculate the ion signal expected for a given peak intensity in the interaction region. We consider the case of the Si-wedge beam-splitter discussed in Paragraph 4.4.4 and assume an XUV source delivering an intensity distribution at the overlap region of the form $I_{XUV}(\vec{r}, t) = \exp(-t^2/\tau_{as}^2) I_{peak} F(\vec{r})$. Here τ_{as} is the duration of a single attosecond beat in the train delivered by the source and $I_{peak} F(\vec{r})$ is the spatial intensity distribution in the overlap region where I_{peak} denotes the peak intensity available. We consider the specific example again, i.e., a harmonic composition consisting of the 9th to 15th harmonic, a Ti:sapphire laser frequency ($\lambda_L = 800$ nm) and Helium gas as a two-photon ionization medium^[117]. In general, the method is limited to photon energies in the range between $I_p/2 - I_p$ of the ionization medium. The reason is that for lower photon energies, two-photon ionization is not occurring and for higher photon energies, single-photon ionization will distort the measurement. Low photon energies do not present a problem because choosing Xenon as ionization medium, the 5th harmonic would already two-photon ionize it. For higher photon energies, direct double ionization processes or direct ionization to higher charge states of the atom can be employed instead of single-ionization. This is possible for short pulse durations^[77].

The number of ions N_{ions} per shot for an attosecond pulse train comprising N_{as} attosecond pulses via two-photon ionization is estimated as:

$$\begin{aligned}
 N_{ions} &= N_{as} \cdot \sigma_{He}^{(2)} \cdot \int_{-\infty}^{+\infty} \int_V \rho_{He} \left(\frac{I_{XUV}(\vec{r}, t)}{\hbar \omega_{XUV}} \right)^2 dt dV \\
 &= N_{as} \cdot \sigma_{He}^{(2)} \cdot \rho_{He} \cdot \left[\frac{I_{peak}}{\hbar \omega_{XUV}} \right]^2 \cdot \int_{-\infty}^{+\infty} e^{-\frac{2t^2}{\tau_{as}^2}} dt \cdot \int_V F(\vec{r})^2 dV \\
 &= N_{as} \cdot \sigma_{He}^{(2)} \cdot \rho_{He} \cdot \left[\frac{I_{peak}}{\hbar \omega_{XUV}} \right]^2 \cdot \sqrt{\frac{\pi}{2}} \cdot \tau_{as} \cdot F_V
 \end{aligned} \tag{4.23}$$

The spatial integral $F_V = \int_V F(\vec{r})^2 dV \approx 10^{-9} \text{cm}^3$ is obtained numerically from the time averaged intensity squared distribution given in the bottom row of Figure 4-8. The cross-section for two-photon ionization of He for a mean photon energy of $\hbar \omega_{XUV} \approx 20 \text{eV}$ is in the literature given as $\sigma_{He}^{(2)} \approx 10^{-52} \text{cm}^4 \text{sec}^{[118]}$. Furthermore, we consider a He atom density in the range of $\rho_{He} \approx (1-6) \cdot 10^{18} \text{cm}^{-3}$ corresponding to a pressure of 50 – 250 mbar. As it has already been mentioned for a train formed by the H9 - H15 phase locked harmonics of equal amplitude, the duration of the individual attosecond pulses is $\tau_{as} \approx 230$ as and we assume a train of $N_{as} = 10$ of such attosecond pulses. Using Equation (4.23) we have calculated the number of ions N_{ions} for an XUV source providing a peak intensity in the autocorrelation volume indicated in the first column of *Table 1* and for two values of He ion concentrations.

It is seen that while for $I_{peak} \approx 10^{11} \text{W/cm}^2$ the expected number of ions is in the range of $N_{ions} \leq 10$ the number increases quadratically with intensity to the level of 10000 for $I_{peak} \approx 10^{13} \text{W/cm}^2$. The signal due to this number of ions should be readily detectable by the ion microscope described in Reference [59] at least for $I_{peak} \geq 10^{12} \text{W/cm}^2$.

Table 1		
$\mathcal{I}_{\text{peak}}$ [W/cm ²]	$\rho_{\text{He}} [\times 10^{18} \text{ cm}^{-3}]$	N_{ions}
10^{11}	1.2	1
	6.2	7
10^{12}	1.2	130
	6.2	650
10^{13}	1.2	1.3×10^4
	6.2	6.5×10^4

Table 4-1 : Estimated number of ions for a range of XUV intensity values and He densities.

In view of the “graininess” of the signal due to a limited number of ions, and assuming a finite spatial resolution of the instrument, the question that arises is: what is the minimum XUV intensity that would allow the retrieval of a statistically relevant signal from a single acquisition. To assess this we have distributed the total number of ions N_{ions} in our estimation along the y -axis according to the amplitude of the smoothed 2nd order signal in Figure 4-8. This presumes that the XUV intensity along the z -axis within the recorded area is approximately constant thus allowing binning along the same direction. The number of bins along the y -axis is determined by the spatial resolution of the instrument. Assuming that the field of view of the ion microscope is approximately the same as the one indicated in the lower row of Figure 4-8, there will be $N_{\text{bin}} \sim 27$ bins for $\Delta s = 2 \mu\text{m}$ and $N_{\text{bin}} \sim 54$ bins for $\Delta s = 1 \mu\text{m}$. Let the average number of ions in the j^{th} bin be $\langle \Delta N_{\text{ion}}(j) \rangle$ normalized as to give $\sum_j \langle \Delta N_{\text{ion}}(j) \rangle = N_{\text{ions}}$. We now assume that in a single recording the number of ions in each of the bins are Poisson distributed with expected value (mean) equal to $m = \langle \Delta N_{\text{ion}}(j) \rangle$. Random deviates drawn from a Poisson distribution with that mean would then represent the fluctuations of the number of ions in each bin for a given total number of ions produced. Figure 4-11 depicts simulated signal due to the expected fluctuations for a range of ion number and two instrument resolutions. It becomes apparent that for $N_{\text{ions}} = 50$ the signal recorded is not “clean” enough to reveal the information needed as the fluctuations are too high and mask the details. The situation becomes considerably better for $N_{\text{ions}} = 500$ while for $N_{\text{ions}} = 1000$ a true reproduction of the 2nd order signal is expected even for $\Delta s = 1 \mu\text{m}$. Under these circumstances, one can assess the presence of a single attosecond pulse and estimate its duration. The mean value of the number of ions per bin is $\sim N_{\text{ions}} / N_{\text{bin}}$. Therefore, according to the Poisson distribution properties the corresponding standard deviation is $\sigma = \sqrt{m}$, thus the fluctuations in each bin scale with the total number of ions and bins as $\delta N_{\text{ions}} = \sqrt{N_{\text{bin}} / N_{\text{ions}}}$ (see Figure 4-11).

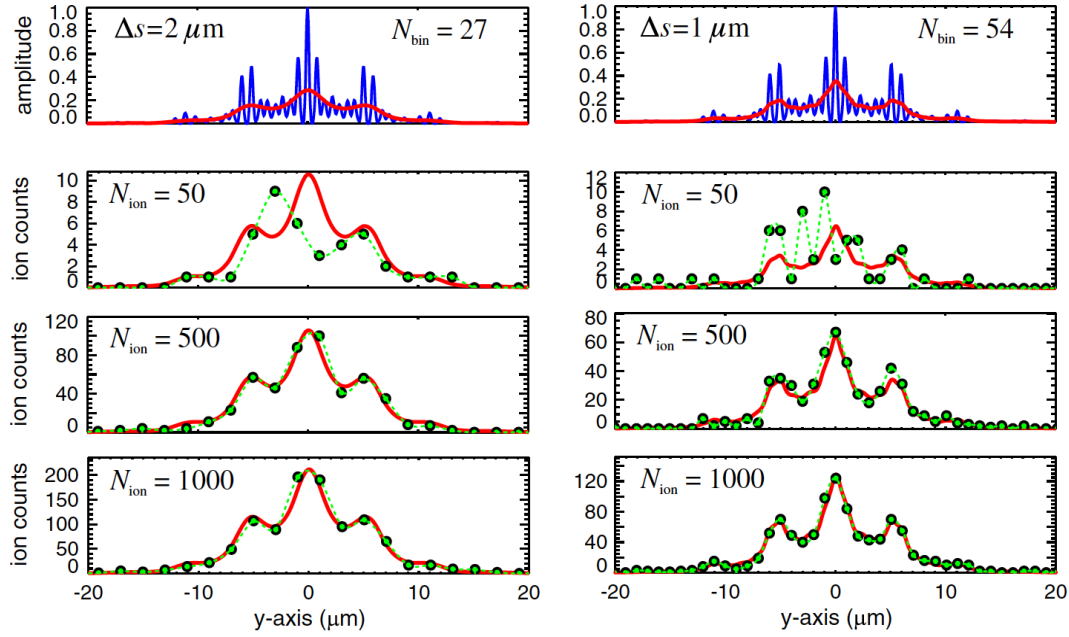


Figure 4-11 : Simulated ion signal for the indicated total number of ions and two different values of spatial resolution. The top row shows a line-out of the time averaged 2nd order signal of the setup shown in Figure 4-8 for infinite resolution (blue line) and convolved with the instrument function for finite resolution (red line) of $\Delta s = 2\mu\text{m}$ (left column) and $\Delta s = 1\mu\text{m}$ (right column). Assuming Poisson distribution for the number of ions in each bin, the statistical signal expected for the total number of ions indicated and the two resolution values are shown in the lower six panels by the green filled points. The green dashed curve is a spline interpolation to guide the eye.

4.6 Summary

We propose here a novel approach to the metrology of attosecond pulses that requires only a single event record. The principle of a single-shot autocorrelator is based on the same idea as in the case of visible or infrared light but it is designed to be used with XUV radiation. The objective is to be able to characterize the output of attosecond pulse sources in a convenient and reproducible way. We have analyzed and investigated the advantages and disadvantages of three different configurations and provided a comparative study. The main parameters associated with each of these setups are summarized in Table 2. In our estimates we have come to the conclusion that a peak XUV intensity of $I_{peak} \approx 10^{12} \text{ W/cm}^2$ in the interaction region will be sufficient to provide an analyzable signal even in a single recording. This implies that the XUV source should deliver enough power, which when focused by a spherical mirror with $f = 5\text{cm}$ would produce a peak intensity of $I_{peak} \approx 10^{15} \text{ W/cm}^2$. This intensity level appears quite within reach^[104,77]. The XUV energy needed to produce this intensity with a train of 10 as-pulses and for ideal focusing conditions is estimated to be $\sim 30 \text{ nJ}$. Although the concept appears feasible and within reach there are a number of practical problems that will have to be addressed before it can be routinely used. To identify these problems an experiment has to be performed with a source of XUV light providing enough intensity to ionize an atomic medium in a two-photon process.

Setup	Characteristic dimensions	f [cm]	\mathcal{F}	Interaction volume dimensions (2nd order) [μm]	Mean intensity at focus [W/cm^2]	Number of ions
Case a Two-aperture mask	$D = 100 \mu\text{m}$ $d = 3 \text{ mm}$	5	$\sim 10^{-7}$	$L_x \sim 28$ $L_y \sim 35$ $L_z \sim 1350$	$\sim 10^8$	~ 0
Case b Two-slit mask	$l_x = 100 \mu\text{m}$ $l_y = 5 \text{ mm}$ $d = 3 \text{ mm}$	5	$\sim 10^{-4}$	$L_x \sim 1$ $L_y \sim 30$ $L_z \sim 35$	$\sim 10^{11}$	~ 6
Case c Beam splitter	$\theta = 2^\circ$	100	$\sim 10^{-3}$	$L_x \sim 10$ $L_y \sim 20$ $L_z \sim 400$	$\sim 10^{12}$	~ 650

Table 4-2 : Summary of the performance for the three setups considered. The reference intensity assumed here is $I_0 = 10^{15} \text{ W}/\text{cm}^2$. The dimensions of the interaction volume have been inferred from the calculated intensity distribution for each case. The number of ions is calculated according to the procedure outlined in Paragraph 4.5.3 for a He density of $\rho_{He} = 6,2 \cdot 10^{18} \text{ cm}^{-3}$. The symbols are defined in the text.

5th Chapter

A compact collinear polarization gating scheme for many-cycle laser pulses

5.1 The Gating Technique

The use of light sources which deliver energetic coherent continuum extreme-ultraviolet (XUV) radiation is highly beneficial for the real-time observation of dynamical processes in the atomic time scale (i.e. atomic unit of time = 24 asec, 1 asec = 10^{-18} sec). The importance of the generation of high photon flux XUV radiation stands on the non-linear processes which can be induced in the target system, and hence on the very interesting XUV-pump-XUV-probe type of experiments which become feasible^[77].

As discussed already in Chapter 2, during 1990's, high-order harmonic generation in rare gases became a topic of interest for the scientific community. The train of pulses which emerges in the time domain, if the harmonics are emitted in phase^[11,119], provides a clear analogy with mode-locked lasers^[48]. Keeping this analogy in mind, people started to think how it would be possible to pick and isolate just one attosecond pulse from the train^[120]. In other words, how it would be possible to create something like a "Pockels cell" operating on the scale of atomic unit of time.

On the above extremely short time scale, it is electronically impossible to build such a "pulse picker" due to the limitations in time of reaction of any electronic equipment. So, any analogy with the Pockels Cells, used extensively in the standard laser technology, stops here. What can be done, as proposed by Corkum et al. in 1994^[120], is to act on the procedure of high-order harmonic generation itself and reduce it on a time scale of one period of the main wavelength of the driving pulse. In this case the spectrum generated does not look anymore like a comb of peaks. It consists instead of a broad XUV quasi-continuum, which corresponds either to a single or to a pair of sub-femtosecond pulses (here the role of the Carrier-Envelope Phase of the driving pulse becomes crucial for the final outcome^[92]).

This confinement of the XUV emission in one period of the main wavelength of the driving field, can be implemented either by using directly one-cycle driving pulses or by using few- or many-cycle driving pulses formulated in such a way that the XUV emission is canceled anywhere but within a small energetic interval of the proper small duration. This interval is called: “the Gate”, and such a formulation of the driving pulse is called: “Gating Technique”. Since the first option remains still an ambitious goal for the scientific community and even the acquisition of an energetic few-cycle pulse laser system remains an expensive desire for many laboratories, Gating Techniques constitute a relatively inexpensive and easy to implement way to generate energetic coherent continuum XUV radiation.

The Gating Technique proposed by Corkum et al. in 1994^[120] relies on the strong dependence of the high-harmonic emission on the ellipticity of the fundamental. Harmonic generation driven by circularly or elliptically polarized laser pulses is indeed much less efficient than that induced by a linearly polarized laser field^[121,122]. The semi-classical explanation is that in a circular polarized laser field the electron is prevented from recombining with the parent ion. Since the high harmonic yield is sensitive to the ellipticity of the laser field, the ellipticity can be exactly the key-feature of a Gating Technique. The harmonic generation can be canceled in a part of the formulated driving pulse with high ellipticity and persists only in a small one-cycle “Gate” of linear polarization (zero ellipticity). In other words, the harmonic generation process can be gated by the polarization of the laser field inside the pulse envelope.

In 1998, it was proposed by Platonenko et al.^[123,124] that pulses with a time-dependent ellipticity could be formed by combining a left-circular pulse and a right-circular pulse of the same main wavelength with a certain delay. This way, an “open Gate” of linear polarization at the center of the formed final pulse is accompanied by wedges of high-elliptical polarization. It is very important that this proposal allows us to keep the most energetic part of the initial (unformed) laser pulse within the gate. The Platonenko et al. scheme is easier to implement than the superposition of two pulses with different main wavelengths as initially proposed by Corkum et al. in Reference [120].

Nevertheless, the idea provided by Platonenko et al. turned out to be feasible only for few-cycle driving laser pulses (< 5 fsec for a main wavelength of 800 nm)^[128,129,131]. For the utilization of the Polarization-Gating approach in high power multi-cycle driving fields, a step further was required. This step concerns the control of the relative field amplitudes between the perpendicular polarized fields in an elliptically modulated driving pulse. This step has been accomplished by P. Tzallas et al.^[125]. By elaborating an Interferometric Polarization Gating (IPG) technique (a schematic presentation of which is shown in Figure 5-1), for the first time coherent continuum XUV radiation has been generated by use of a high power multicycle driving field.

Since 2007, two different types of IPG apparatuses have been invented by people of our group. The first is based on a Double Michelson Interferometer arrangement^[125] (Figure 5-2(a)), while the second on a Double Mach-Zender Interferometer arrangement^[126] (Figure 5-2(b)). The Interferometric Polarization Gating devices succeeded in making many-cycle laser pulses able to generate energetic isolated attosecond pulses. Nevertheless, technical aspects related to lack of handiness and long-term stability led us to seek an alternative idea.

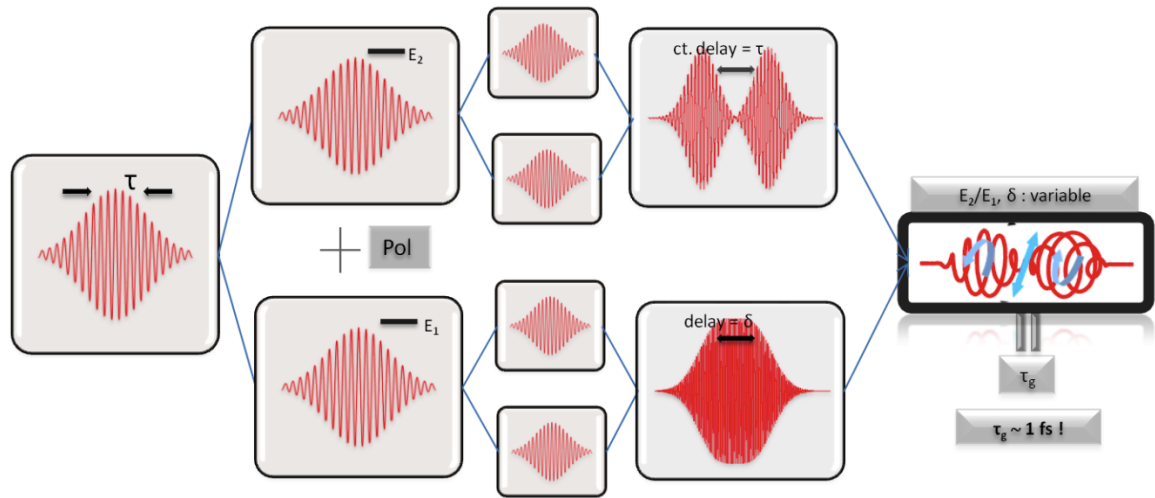


Figure 5-1 : Schematic presentation of the Interferometric Polarization Gating technique. The incoming pulse with duration τ_L is split into two with different amplitudes $E_d = E_2$ and $E_c = E_1$. Subsequently, each one of these pulses is split again into two. In each pair the pulses are appropriately delayed with respect to each other in such a way that those of the first pair interfere constructively (forming a maximum at the center) and those of the second destructively (forming a minimum at the center). The fringe structures (Constructive and Destructive) formed by each pair of the delayed pulses, are polarized perpendicularly to each other. The two structures are superimposed forming a final pulse of modulated ellipticity and with linear polarization only at its central part. The width τ_g of this interval, where the polarization is almost linear, is called “gate width”. {Figure reprinted from Reference [138]}

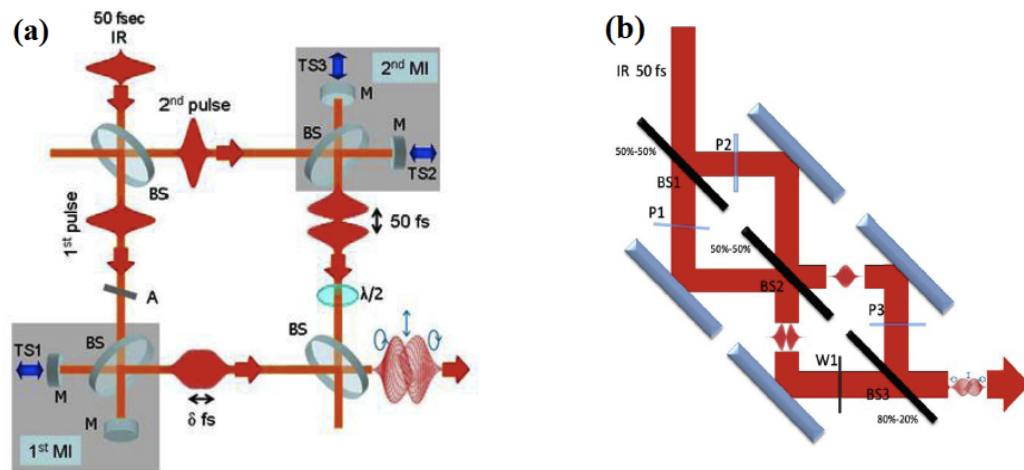


Figure 5-2: (a) IPG apparatus based on a Double Michelson Interferometer arrangement^[125]. BS: beam splitters. M: flat mirrors. TS1,2,3: piezoelectric translation stages. A: intensity attenuator. 1st and 2nd MI: first and second Michelson Interferometers. **(b)** IPG apparatus based on a Double Mach-Zender arrangement^[126]. P1, P2, P3: Delay plates. W1: $\lambda/2$ wave plate. BS1, BS2, BS3: Beam Splitters. BS1, BS2 are 50:50 beam splitters, while BS3 has 20% reflectivity and 80% transmission. {Figure (a) reprinted from Reference [125], Figure (b) reprinted from References [126] and [82]}

5.2 Concept and description of the Collinear Many-cycle Polarization Gating Scheme

In 2003, Tcherbakoff et al.^[127] tried to increase the bandwidth of the harmonics by introducing a linear method to modulate the ellipticity of the fundamental pulse. They used a combination of two quartz quarter wave plates. The first is a multiple-order quarter wave plate (MO) and the second wave plate is a zero-order quarter one (ZO). When the incident polarization is at 45° in respect to the axis of the MO plate, the initial pulse splits into two identical delayed linearly polarized pulses with perpendicular polarizations to each other. The total field of the outgoing pulse results in being circularly polarized at the center and linearly polarized elsewhere. The second wave plate (ZO) is used in order to inverse this scheme. When its axis is rotated at 45° compared to the axis of the first plate, the transmission of the previously shaped pulse through it, changes the circular field into linear and the linear into circular. Consequently, the combination of the two plates transforms an input linearly polarized pulse into a pulse whose polarization changes from circular to linear and back to circular. Using this "waveplate" (WP) scheme, Tcherbakoff et al.^[127] managed to observe a small broadening of the harmonic bandwidth but they didn't succeed on increasing it to the level which can support isolated attosecond pulses.

As described in the introduction of this chapter, the first successful experiment on generating energetic isolated attosecond pulses by using multi-cycle high power fs lasers came in 2007 by P. Tzallas et al.^[125] by utilizing the IPG approach. In the present work, by combining the idea of the IPG approach with the WP scheme, a new Polarization Gating configuration has been developed. Additionally, this new configuration has the advantage to be linear, compact, user-friendly and with long-term stability.

As it was already well-known by the implementation of the Interferometric Polarization Gatings^[125,126], the gate width can be tuned via the ratio $R = E_{p0}/E_{s0}$ of the p -polarization and s -polarization amplitudes (Figure 5-3). Explicitly^[126]:

$$\tau_g \approx \frac{\log_2(A) \tau_L}{2 \delta} \quad (5.1),$$

where:

$$A = \frac{-2R \sqrt{1-B^2} + B(R^2-1)}{B-2R+BR^2} \quad (5.2),$$

R is the ratio above, δ the delay introduced by the MultiOrder (MO) waveplate and:

$$B = \sin(2 \arctan(\varepsilon_{th})) \quad (5.3),$$

with ε_{th} the ellipticity threshold for the harmonic in consideration. As an example of applying the above relations: for $\varepsilon_{th} = 0.1333$ (which is the ellipticity threshold for the 17th harmonic^[131]), and $R \approx 0.45$, a $\tau_g \approx 3.7$ fs is expected to be formed in a 66fs elliptically modulated pulse.

This possibility of tuning the gate width via the ratio R gave the idea to introduce an additional optical element with which it would be possible to control this ratio^[130]. As such was chosen a silicon plate (Si) to be positioned with its surface vector on the plane of incidence. The reflectivity of the plate, for 800 nm wavelength, depends on the angle of incidence θ and on the polarization of the incident light as can be seen in Figure 5-4(e).

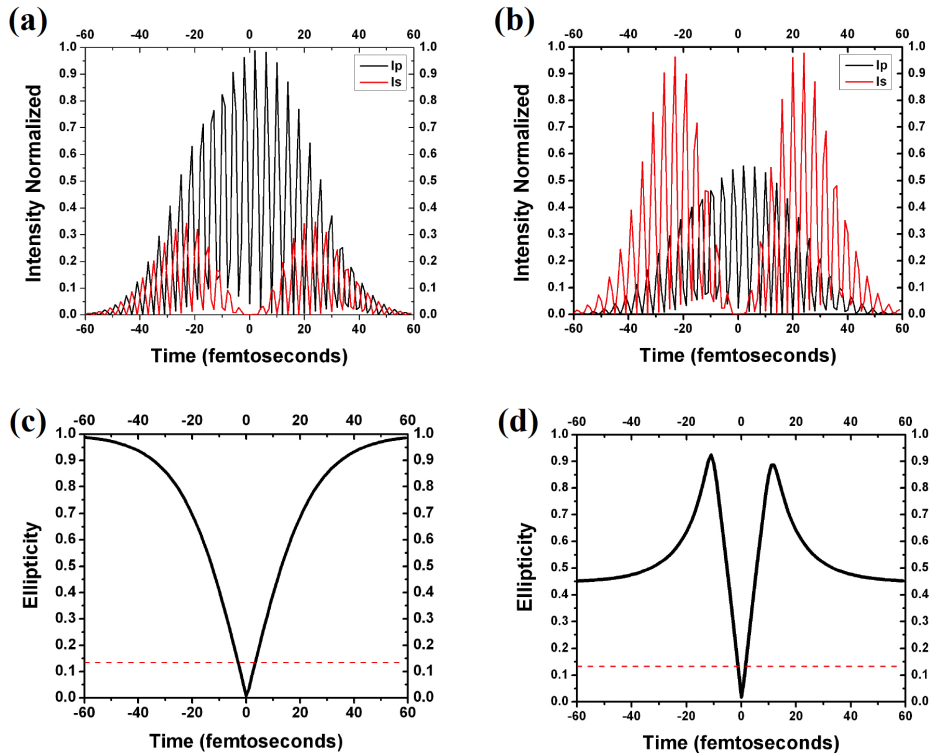


Figure 5-3: Normalized calculated squared fields of the two components are depicted for the formed pulse: with polarization parallel (black color) and vertical (red color) to the plane of incidence. **(a)** for $R = 1$ (this means: without using the Si-plate). **(b)** The squared fields for $R = 0.45$. **(c)** Ellipticity curve calculated corresponding to the pulse in case (a). **(d)** Ellipticity curve calculated corresponding to the pulse in case (b). In (c) and (d), with red dashed line, the ellipticity threshold for the 17th harmonic^[131] is also depicted. The angle of the multi-order quarter wave plate is assumed to be 0. The pulse initially is taken with $\tau_L = 33$ fs duration. Chirp induced to the pulse from the optics has not been taken into account.

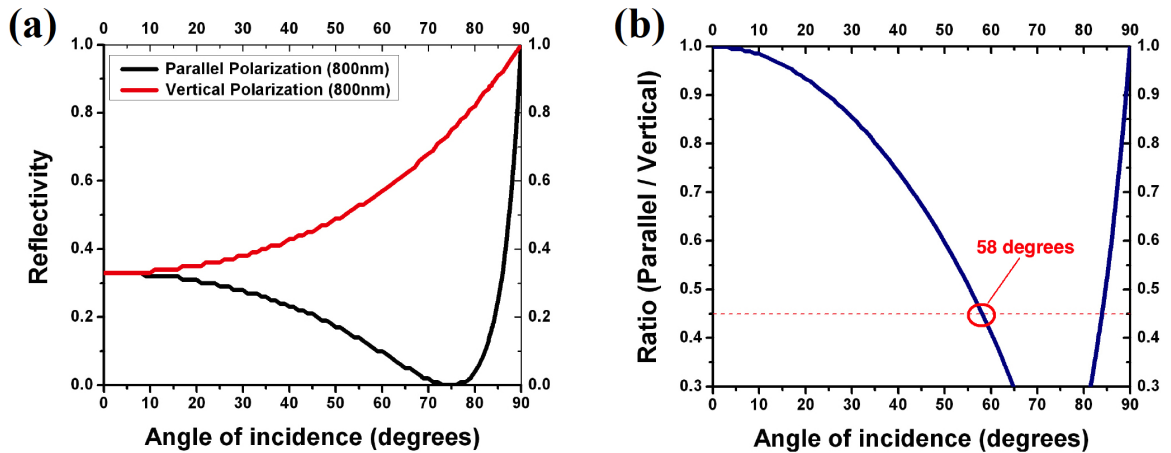


Figure 5-4: **(a)** The reflectivity of the Si plate with respect to the angle of incidence, for parallel (black) and vertical (red) polarization of incident light of wavelength 800 nm^[132]. **(b)** The ratio R (amplitude of p -polarized electric field after reflection to the amplitude of s -polarized electric field after reflection) with respect to the angle of incidence. As it can be seen, there are two distinct values of angle of incidence for which $R = 0.45$. For the second one ($\sim 84^\circ$) the energy, carried by the pulse after reflection, is larger.

Apart from the Si-plate, the other three optical elements of the Collinear Many-Cycles Polarization Gating (CMC-PG) are the waveplates which are schematically shown in Figure 5-5.

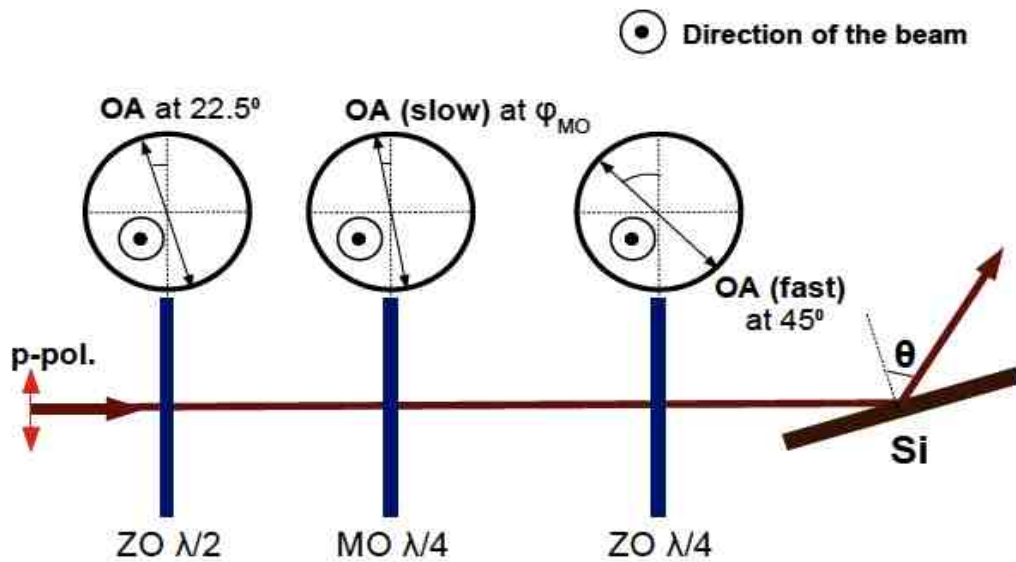


Figure 5-5 : The CMC-PG device as it is used for the generation of the coherent continuum XUV radiation. ZO $\lambda/2$: Zero-order half waveplate, ZO $\lambda/4$: Zero-order quarter waveplate, Si: 15 cm long Silicon plate, MO $\lambda/4$: Multiple-order quarter waveplate. The orientations of the OA of the plates, which are shown at the top, are controlled by rotatable mounts on which the plates have been placed. All the surfaces of the wave-lates are set to be perpendicular to the direction of the IR laser beam which is shown and to be towards the reader.

The first, in the way of the beam, is a 1290 μm thick zero-order (ZO) $\lambda/2$ waveplate with its optical axis (OA) at 22.5° . This waveplate is used just to rotate the polarization of the laser (which is initially p -polarized) by 45° .

The second waveplate is a 1060.7 μm thick multiple-order (MO) $\lambda/4$ waveplate with its slow (ordinary) axis at an angle φ_{MO} relative to the s -direction (vertical direction in the Laboratory). This angle φ_{MO} (the proper value to reach the gating conditions in each case) is proved to be depended on the total chirp induced on the pulse by the optical elements which participate in the experimental setup [see also the discussion in Section 5.4]. The MO waveplate was ordered having in mind the very specific features of the pulse provided by our laser system: FWHM = 33 fs, Central Wavelength = 804 nm. For each experiment, this has to be selected accordingly to the laser pulse features. In our case it provides a delay of 32.83 fs (which means: 12 full cycles and a quarter) to an electromagnetic wave at 804 nm moving with polarization parallel to the ordinary axis with respect to that of the same wavelength moving with polarization parallel to the extraordinary axis. By measuring the duration of the IR laser pulse after the MO plate it is verified that a delay of ~ 33 fs is indeed introduced. This measurement is performed by a 3rd order autocorrelator after the passage of the beam through a p -polarizer. For this measurement, the OA of the ZO $\lambda/2$ waveplate is set at 0° . The green dots in the Figure 5-6(b) show the pulse form when setting one of the Optical Axes (it does not matter which) of the MO plate at 0° (neutral position in this case). The width at the half maximum of the Gaussian fit on the raw data (red line) corresponds to the laser pulse duration

which is found to be 33 fs. The black dots show the pulse form when setting the one of the Optical Axes of the MO waveplate at 45° . The width of this last trace is found to be 66 fs and is in excellent agreement with the overall duration of the double pulse created by the MO waveplate. The outgoing field is elliptically modulated with circular polarization at the center.

Concerning the MO waveplate, it is also very important to recall that the optical bandwidth, in which the plate has roughly the “correct” relative phase change, is limited. This results in the MO waveplate not acting in the same way for each wavelength within the spectral bandwidth of the pulse used [see Figure 5-6(a)].

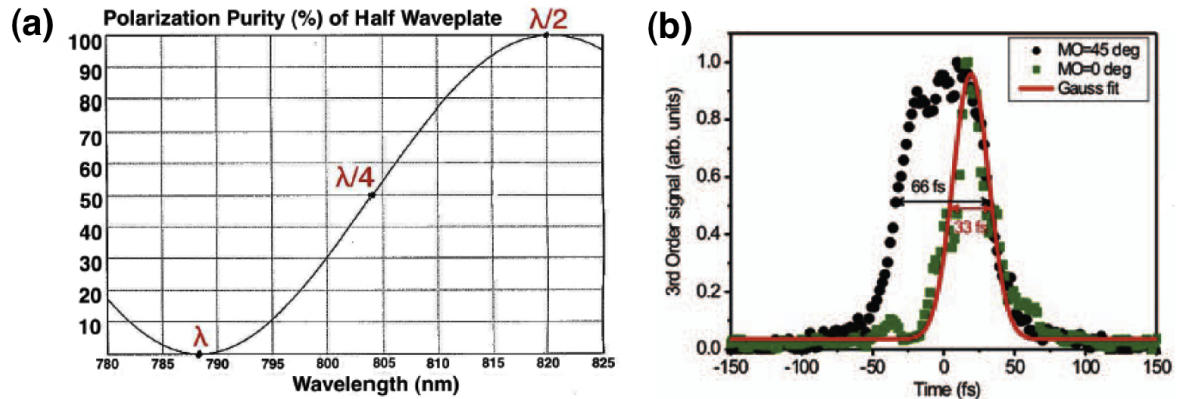


Figure 5-6: (a) The polarization purity of half waveplate with respect to the wavelength for the MO waveplate [function graph sent by EKSMA Optics - <http://eksmaoptics.com/>]. (b) Temporal characterization of the p -polarization IR pulse after passing through the MO plate. Green points: p -polarization IR pulse form for $\varphi_{MO} = 0^\circ$. The red line is a Gaussian fit on the raw data. Black points: p -polarization IR pulse form for $\varphi_{MO} = 45^\circ$.

The third waveplate, in order, is a $1265 \mu\text{m}$ thick zero-order (ZO) $\lambda/4$ waveplate. At gating conditions the fast axis has to be at -45° angle with respect to the s -direction. This way it converts the circularly polarized field at the center of the pulse to a linearly polarized one (parallel to p -direction) and leaves the field circularly or elliptically polarized anywhere else. If the fast axis is at 45° angle with respect to the s -direction, the circularly polarized field at the center of the pulse will become again linear, but parallel to the s -direction this time. The ZO $\lambda/4$ waveplate, together with the ZO $\lambda/2$ waveplate, present roughly the correct relative phase change throughout the optical bandwidth needed.

5.3 Experimental results and discussion

The experiment, which demonstrates the generation of a broadband quasi-continuum XUV radiation by using the CMC-PG, is performed with a CEP unstable 1 kHz repetition rate Ti:sapphire laser system delivering pulses of energy 2mJ/pulse at $\tau_L = 33$ fs duration and central wavelength at 804 nm. The experimental set-up is shown in the Figure 5-7.

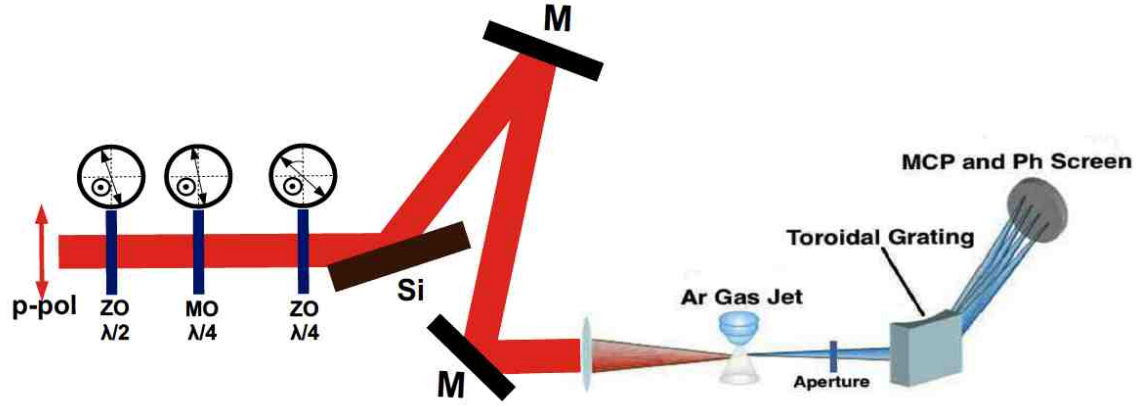


Figure 5-7: The CMC-PG device and the experimental set-up used for the generation of the coherent quasi-continuum XUV radiation.

The Optical Axes of the three waveplates are oriented, with respect to the vertical direction, as described in the previous paragraph, with $\Phi_{MO} \approx 14^\circ$. The angle of incidence θ of the beam on the Si plate has been set at 58° , providing a ratio $R \approx 0.45$ of the p -pol and s -pol field amplitudes [see Figure 5-4(b)]. With these values, a $\tau_g \approx 3.7$ fs is expected to form within a 66 fs elliptically modulated pulse.

The energy of the outgoing pulse was measured to be $E_{out}^{IR} = 120$ μ J and, so, the energy content inside the gate E_g^{IR} is extracted:

$$E_g^{IR} \approx \frac{E_{out}^{IR}}{P(\tau_L, \delta)} \quad (5.4),$$

where:

$$P(\tau_L, \delta) \approx \frac{\tau_{out}^{IR}}{A \tau_g} \quad (5.5),$$

τ_{out}^{IR} is the duration of the outgoing pulse and:

$$A = \frac{E_{out}^{IR}}{\int_{-\tau_{out}/2}^{+\tau_{out}/2} |\vec{E}_{out}^{IR}(t)|^2 dt} \quad (5.6).$$

Using the above formulas, it can be found that: $E_g^{IR} \approx 13$ μ J.

This value of the energy content inside the gate for the CMC-PG is ~ 3 times lower compared to that reached by the Double Mach-Zender IPG (DMZ-IPG) arrangement^[126]. Nevertheless, a higher value of E_g^{IR} can be achieved by setting the angle of incidence on the Si plate at $\sim 84^\circ$. As it can be seen in Figure 5-4(b), the same ratio R results for $\theta = 84^\circ$ as for $\theta = 58^\circ$. In this case E_g^{IR} will be comparable to that obtained by the DMZ-IPG arrangement.

The CMC-PG output beam is focused by 20 cm focal length lens into a pulse gas jet filled with Argon gas where the XUV radiation is generated. The harmonic radiation is monitored by an XUV toroidal grating monochromator in a grazing-incidence configuration, equipped with an imaging detector, coupled to a CCD camera.

The beam focus is placed at ~ 0.5 mm before the gas jet position (arrow in the Figure 5-8(a)) in

order to reduce the contribution from long electron trajectories^[133,134] [see also Chapter 2]. The dependence of the XUV intensity on the focus position, shown in Figure 5-8(a), has been recorded by setting the OA of the ZO $\lambda/2$, MO, and ZO $\lambda/4$ waveplates at 22.5° , 45° and 45° respectively and by using a linearly polarized 33 fs long pulse of 400 μJ energy.

The XUV spectra, which appear in Figure 5-8(b), have been recorded for four different angles of the slow (ordinary) axis of the MO plate ($\varphi_{MO} = 14^\circ, 33^\circ, 45^\circ$). For each angle of the MO-plate, the energy outgoing from the CMC-PG device is kept constant at 120 $\mu\text{J}/\text{pulse}$ in order to permit accurate comparison between them. It has been found experimentally that the value of the angle between the Slow Optical Axis and the vertical direction for which the broader quasi-continuum XUV radiation is obtained, is not at 0° (as intuitively was expected) but at 14° (yellow filled spectrum in Figure 5-8(b)). This unexpected effect is explained by a computer simulation of the experiment [see Section 5.4]. For angles in the range $14^\circ < \varphi_{MO} < 45^\circ$, the harmonic peaks in the spectrum are more pronounced (green and black lines in Figure 5-8(b)). For $\varphi_{MO} = 45^\circ$ (neutral position - the outgoing pulse remains linearly polarized everywhere with 33 fs duration), an XUV spectrum with well confined harmonic frequencies is recorded (black line in Figure 5-8(b)). The inset of Figure 5-8(b) shows the images of an XUV continuum and a frequency comb spectrum recorded respectively for $\varphi_{MO} = 14^\circ$ and $\varphi_{MO} = 45^\circ$.

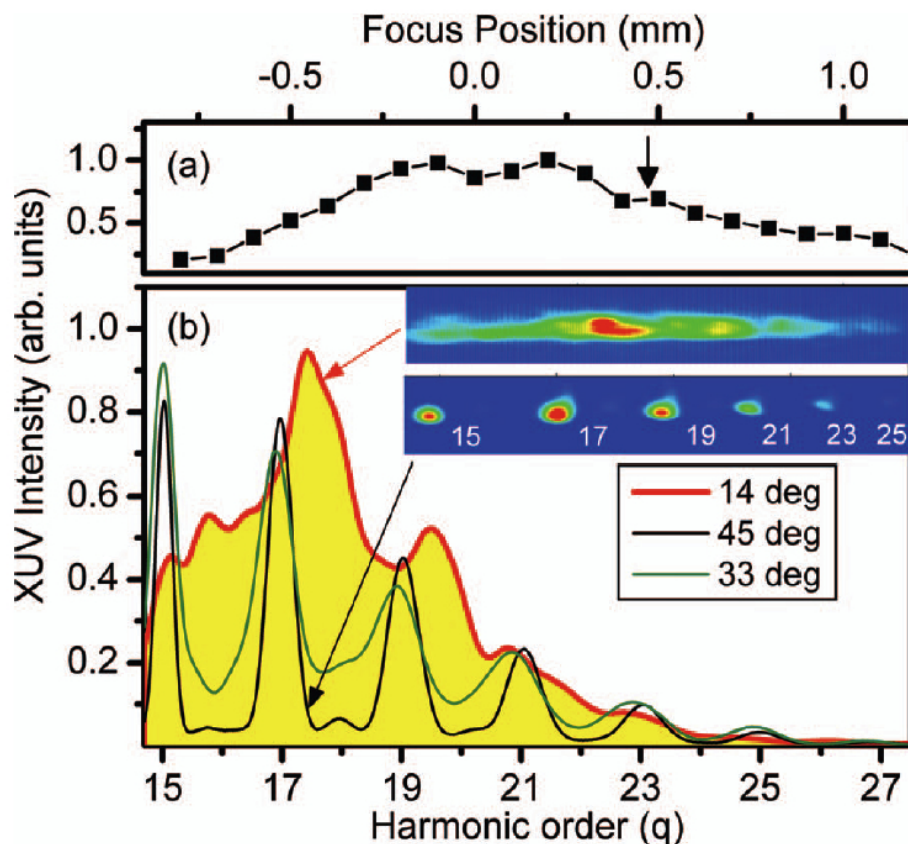


Figure 5-8: (a) Harmonic intensity dependence on the focus position relative to the gas jet, which has been placed at 0 mm position. The arrow depicts the focus position during the experiment. (b) XUV spectra recorded at different values of φ_{MO} . The inset shows the image of an XUV continuum and an harmonic frequency comb spectrum recorded for $\varphi_{MO} = 14^\circ$ and $\varphi_{MO} = 45^\circ$, respectively. For each value of the φ_{MO} , the energy of the IR beam entering into the interaction chamber is 120 $\mu\text{J}/\text{pulse}$. For each spectrum, 5000 shots have been accumulated.

The energy of the XUV continuum emitted at $\varphi_{MO} = 14^\circ$, is found to be ~ 15 times lower compared to the energy of the harmonic spectrum recorded at $\varphi_{MO} = 45^\circ$. This factor is in agreement with the value of ~ 10 , which can be derived by calculating the ratio of the XUV emission for $\varphi_{MO} = 45^\circ$ and $\varphi_{MO} = 14^\circ$:

$$\frac{Y_{XUV}^{45^\circ}}{Y_{XUV}^{14^\circ}} = \left(\frac{I_{(IR)}^{45^\circ}}{I_{(IR)}^{14^\circ}} \right)^p \frac{\tau_{(IR)}^{45^\circ}}{\tau_{(IR)}^{14^\circ}} \quad (5.7).$$

In equation (5.7) the yield of the XUV emission is: $Y_{XUV}^{\varphi_{MO}} \approx \left(I_{(IR)}^{\varphi_{MO}} \right)^p \tau_{(IR)}^{\varphi_{MO}}$ (5.8),

where: $\tau_{(IR)}^{\varphi_{MO}}$ is the duration of the linear part of the outgoing pulse, $I_{(IR)}^{\varphi_{MO}}$ the intensity of the outgoing linearly polarized IR field (the part of the pulse inside the ‘‘Gate’’ when we refer to elliptically modulated pulses), $p \approx 4$ is the nonlinearity factor of the harmonic generation procedure for harmonics close to the ‘‘plateau’’ region^[135].

5.4 Computer simulation - Results and discussion

Calculations of the propagation of the IR beam through the whole optical arrangement are performed, taking into account the reflectivity of the Si-plate and the dispersion of the optical elements in use; namely, the 3 waveplates, the lens and the vacuum windows. The initial pulse is analysed into frequency components and for each color is considered the propagation of the corresponding plane wave. The amplitude of such a monochromatic wave is calculated by the spectral distribution which corresponds to the pulse. That is to say, the pulse is considered as a gaussian one with a **F**ull **W**idth at **H**alf **M**aximum (FWHM) of 33 femtoseconds and with central wavelength $L_0 = 804$ nm. Thus, the inverse Fourier transformed envelope of the field, in the frequency domain, is given by:

$$FE(\omega) = \exp\left(-\frac{\sigma_E^2(\omega - \omega_0)^2}{4}\right) \sigma_E \sqrt{\pi} \quad (5.9),$$

where: $\omega_0 = \frac{2\pi c}{L_0}$ and $\sigma_E = \frac{FWHM}{\sqrt{2 \cdot \ln 2}}$.

The refractive indices of the birefringent materials, for both the Optical Axes (ordinary and extraordinary) and for each wavelength, are calculated using the data provided by the company Melles Griot*. The phase shift imposed to every single spectral component of the pulse passing through the MO, depends on the direction of the polarization in comparison to the optical axis. Thus, for the component of the monochromatic wave with wavelength λ which is parallel to the extraordinary axis, the phase shift is given by:

$$ExitPhaseE(\lambda) := \frac{2\pi}{\lambda} N_e(\lambda) L_M \quad (5.10),$$

* [<http://www.cvimellesgriot.com>]

where L_M is the length of the MO and $N_e(\lambda)$ is the refractive index given by Melles Griot for the specific wavelength λ and polarization parallel to the extraordinary axis. Correspondingly, for the component parallel to the ordinary axis:

$$ExitPhaseO(\lambda) := \frac{2\pi}{\lambda} N_o(\lambda) L_M \quad (5.11).$$

In order to reconstruct the laser pulse after the transmission through the MO, we have to consider the interference of all the spectral components. So, for each one of the field components, with polarization parallel to the extraordinary axis and those with polarization parallel to the ordinary axis, we obtain correspondingly:

$$PulseMultiE(t, \varphi_{MO}) := \cos[\varphi_{MO}] \cdot E_0 \cdot \sum_{\lambda=\lambda_{min}}^{\lambda_{max}} FE\left(\frac{2\pi c}{\lambda}\right) \cdot \exp\left[i \cdot \left(\frac{2\pi c}{\lambda} \cdot t + ExitPhaseE(\lambda)\right)\right] \quad (5.12)$$

$$PulseMultiO(t, \varphi_{MO}) := \sin[\varphi_{MO}] \cdot E_0 \cdot \sum_{\lambda=\lambda_{min}}^{\lambda_{max}} FE\left(\frac{2\pi c}{\lambda}\right) \cdot \exp\left[i \cdot \left(\frac{2\pi c}{\lambda} \cdot t + ExitPhaseO(\lambda)\right)\right] \quad (5.13),$$

where φ_{MO} is the angle between the extraordinary axis and the direction of the pulse polarization before reaching the MO. E_0 is a normalization factor which depends on the partition (the number of steps) used in the frequency domain and is given from:

$$E_0 = \left[\frac{\sigma_E}{\sqrt{2}} \cdot \sqrt{\pi} \cdot NumberSteps \right]^{-1} \quad (5.14).$$

In our calculation, we take into account the interval $[L_{min}, L_{max}] = [704 \text{ nm}, 904 \text{ nm}]$ and we use a partition of 2000 steps.

For the other two waveplates, the zero-order ones, we do not separate the pulse into frequency components, but we use the simple Jones' formalism instead. This is done because the difference in dispersion, between propagations with polarization parallel to each one of the two axis, is not such, concerning the spectral region into consideration, as to impose to be followed a procedure similar to the case of the Multi-order waveplate.

Nevertheless, the additional dispersion (from the vacuum windows, the lens and the 2 zero-order waveplates) is taken into account via an equation similar to the equations (5.10) and (5.11). Namely:

$$ExitPhaseZ(\lambda) := \frac{2\pi}{\lambda} \cdot N_m(\lambda) \cdot L_z \quad (5.15),$$

where $N_m(\lambda)$ is taken to be the mean value of $N_e(\lambda)$ and $N_o(\lambda)$ for any given wavelength λ . The L_z stands for the total thickness of dispersive media the driving pulse meets in its way towards the generating medium. By trying various values for L_z , we can realize the effects of the total chirp induced by the optical components of the setup on the shape of the pulse and on the duration of the ‘‘Gate’’.

In fact, the computer simulation explains well the initially awkward effect the broader quasi-continuum XUV spectrum to be generated not by putting the MO $\lambda/4$ Slow Axis at vertical position but, instead, by putting it at an angle of $\varphi_{MO} \sim 14^\circ$ to the vertical direction. This ‘‘strange’’ offset is shown to be due to the fact that the narrowest ‘‘Gate’’ is not obtained for $\varphi_{MO} = 0^\circ$. If the chirp induced to the pulse by the dispersion of the optical elements is taken into account, the narrowest

“Gate” is obtained for an angle $\varphi_{MO} > 0$ [as it can be seen in Figures 5-9 and 5-10]. It is also proved, by running the simulation supposing the existence of a dispersive medium with various thickness, that this offset angle depends on the total amount of the chirp induced to the pulse.

On the field of the “Gating” techniques, the most important function is the ellipticity throughout the duration of the pulse which comes out from the “Gating” apparatus. This ellipticity function is obtained by the equation^[126]:

$$\varepsilon(t) = \tan \left[\frac{1}{2} \cdot \sin^{-1} \left(\frac{2 \cdot |\vec{E}_s| \cdot |\vec{E}_p|}{|\vec{E}_s|^2 + |\vec{E}_p|^2} \right) \right] \quad (5.16),$$

The width of the “Gate” and its exact position along the pulse can be provided by the function $\varepsilon(t)$ in the equation (5.16). In what follows, we will examine a few characteristic cases.

In the Figure 5-9 one can see, for various values of the φ_{MO} , the intensity envelopes for the p - and s -polarization components of the exiting, from the CMC-PG, pulse together with the ellipticity curve throughout its duration. It is important to notice the lack of symmetry between the cases $\varphi_{MO} = 10^\circ$ and $\varphi_{MO} = -10^\circ$, what is clearly realized also experimentally. It is also important to notice that for $\varphi_{MO} = 10^\circ$, value for which the narrower gate is formed, the “Gate” does not contain the central (most energetic) part of the I_p envelope. Contrarily, the “Gate” contains a part of the envelope with a rising slope.

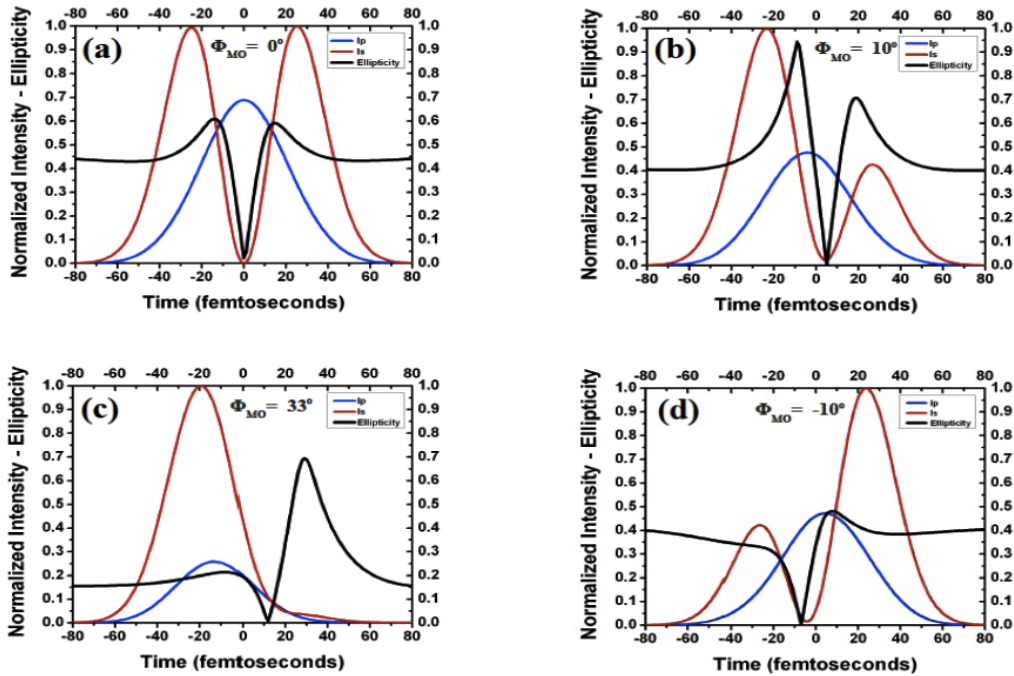


Figure 5-9: (a) For $\varphi_{MO} = 0^\circ$ the “Gate” is opened at the center of the formed pulse and contains the central (most energetic part) of the I_p envelope. (b) For $\varphi_{MO} = 10^\circ$ the “Gate” is the narrowest of all these four cases. The “Gate” is transposed towards the rising part of the formed pulse and contains a part of the I_p envelope with a rising slope. (c) For $\varphi_{MO} = 33^\circ$, the I_p and the I_s components of the formed pulse do not remind much from the typical “Gating Scheme”. The “Gate” becomes very wide, with $\tau_g \sim 10$ fs. In addition to this, the linear polarization inside the “Gate” is not anymore parallel to the p -direction, but starts to be at an angle of 45 degrees with the p -direction (as you can see, inside the Gate, $I_p = I_s$). (d) For $\varphi_{MO} = -10^\circ$ we have a completely different case than for $\varphi_{MO} = 10^\circ$. The envelopes for I_p and I_s are very similar (they are symmetric) to the ones in case (b). Nevertheless, the “Gate” formed is much wider. This is due to the relative phases between the field components in p - and s -direction. These relative phases do not appear in the Figure.

In the Figure 5-10, we transpose in time the previous ellipticity curves in order to make them all to share a common origin. This way we become able to compare their “Gate” widths to each other.

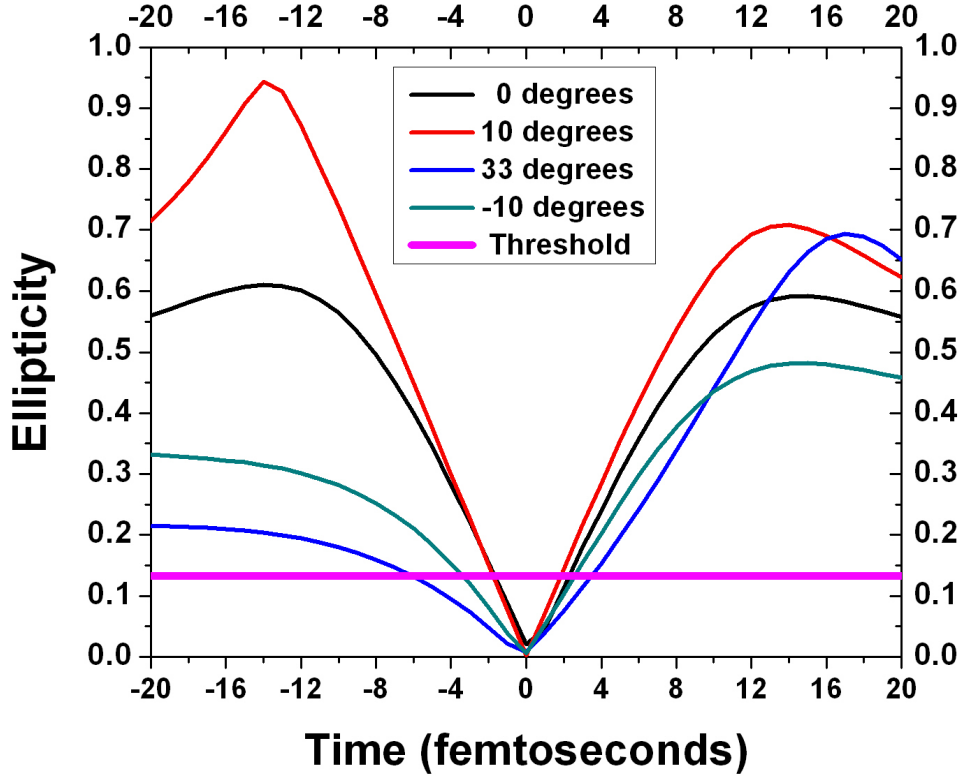


Figure 5-10 : Comparison between the “Gate” widths. The ellipticity curves for the same φ_{MO} values as in the Figure 5-9. The curves are transposed in time, in such a way as to present their minimum value at the same point on the time-axis (which is not at all true, as shown in Figure 5-9). The horizontal purple line marks the ellipticity threshold value (0.133) for the 17th harmonic.

In the Figure 5-11 is shown the dependence of the “Gate” width τ_g on φ_{MO} (green squares). Considering that:

$$\frac{\Delta\omega_q^{\varphi_{MO}}}{\Delta\omega_q^{45^\circ}} = \frac{\tau_q^{45^\circ}}{\tau_q^{\varphi_{MO}}} \quad (5.17),$$

(where $\Delta\omega_q$ is the spectral width of the q^{th} harmonic and $\tau_q^{45^\circ}$ is the duration τ_L of the unformed driving pulse) one is able to compare the results derived from the calculation with the data extracted from the experiment. The harmonic spectral broadening of the 17th harmonic, for various values of the φ_{MO} , is measured and compared with the inverse of the corresponding calculated τ_g . The results are shown in the Figure 5-11, with red circles for the calculated ones and black for the

experimentally obtained ones. The width of the harmonic frequency is measured by fitting a sum of Gaussian functions with their maxima on the central frequencies of the harmonic peaks. For $\varphi_{MO} < 25^\circ$ the Gaussian fitting function does not converge since the large broadening of the harmonics results in a spectral overlap. Nevertheless, it is apparent that for $\varphi_{MO} > 25^\circ$ the experimental values are in good agreement with the calculated ones.

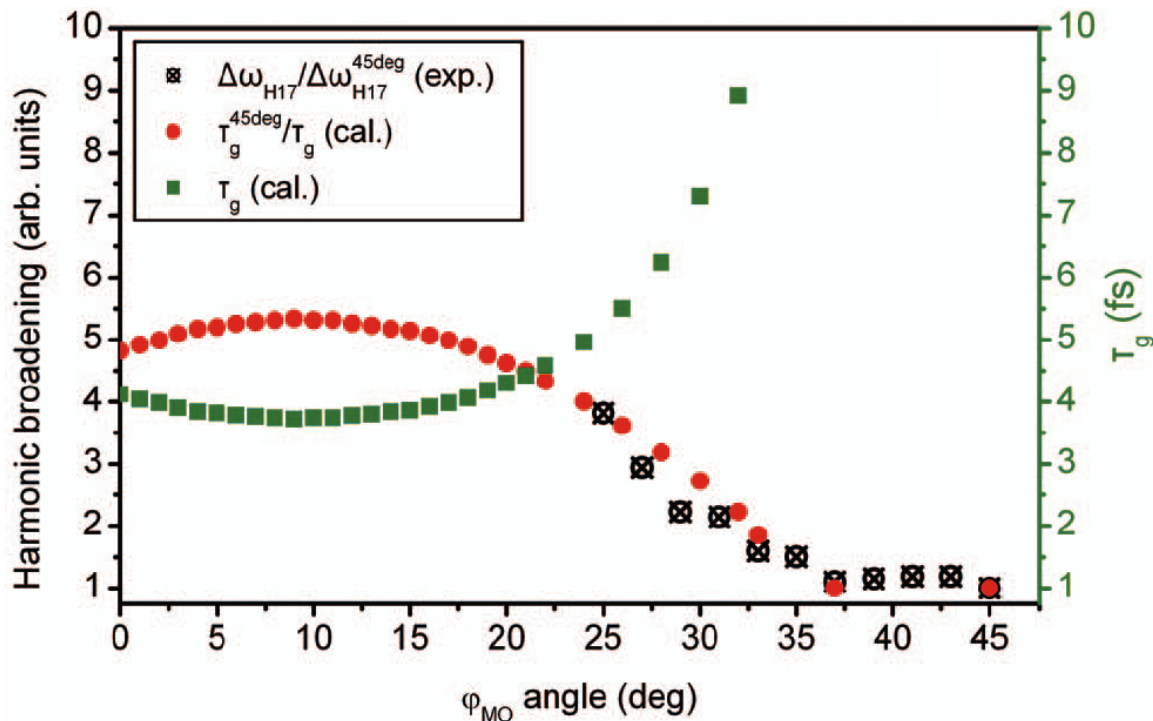


Figure 5-11 : The green squares show the dependence of τ_g on φ_{MO} . The measured and the calculated harmonic spectral broadening are shown in black and red circles, respectively. For each value φ_{MO} , the energy of the IR beam entering the interaction chamber is 120 μ Joules/pulse.

5.5 Conclusions

A broadband coherent quasi-continuum XUV radiation which can support pulses of 200 asec duration has been generated by implementing the above described Collinear Many-Cycle Polarization Gating (CMC-PG) device. For the first time this waveplate-based Polarization Gating Technique is expanded to Many-Cycle laser systems. The thickness of the Multi-Order waveplates, which is connected to the necessary temporal delay δ [see Equation (5.1)], in previous schemes used to impose some limitation because it resulted in large B-integral values and in small energy content inside the “Gate”^[136]. This limitation has been overcome here by the use of the Si-plate as a field amplitude ratio modulator. By using the CMC-PG device, a gate width of ~ 3.7 fs becomes feasible for many-cycle Ti:Sapphire laser systems delivering pulses of ~ 30 fs duration and intensity up to 1 TW/cm².

Nevertheless, limitations still exist concerning to the duration of the initial pulse. For a longer pulse would be needed a Multi-Order waveplate able to induce a bigger temporal delay. This

inevitably means a thicker one which would provide, apart from the larger B-integral value, a bigger degradation on the shape of the formed pulse [see Figure 5-9]. On the other hand, the CMC-PG device would be an ideal tool to be used with high-power laser systems delivering pulses shorter than 30 fs. There, the “Gate” width could become narrower and containing more energy.

REFERENCES

- [1] P. Krehl and S. Engemann, "August Toepler – The first who visualized shock waves", *Shock Waves*, **5**, 1-18 (1995).
- [2] Abraham, H.; Lemoine, J. C. R. *Hebd. Seances Acad. Sci.*, **129**, 206–208 (1899).
- [3] The Nobel Prize in Physics 1956 was awarded jointly to William B. Shockley, John Bardeen, Walter H. Brattain "for their researches on semiconductors and their discovery of the transistor effect".
- [4] Theodore Maiman, "Stimulated Optical Radiation in Ruby". *Nature* **187**: 493–494 (6 August 1960).
- [5] F. J. McClung and R. W. Hellwarth, "Giant Optical Pulsations from Ruby", *J. Appl. Phys.* **33**, 828 (1962).
- [6] A.J. DeMaria, D.A. Stetser, and H. Heynau, "Self mode - locking of lasers with saturable absorbers", *Appl. Phys. Lett.* **8**, 174 (1966).
- [7] P.F. Moulton, "Spectroscopic and laser characteristics of Ti: Al₂O₃", *JOSA B*, **Vol. 3**, Issue 1, pp. 125-133 (1986).
- [8] R.L. Fork, C.H. Brito Cruz, P.C. Becker, and C.V. Shank, "Compression of optical pulses to six femtoseconds by using cubic phase compensation", *Optics Letters*, **Vol. 12**, Issue 7, 483-485 (1987).
- [9] Ahmed H. Zewail, "Femtochemistry: Atomic-scale dynamics of the chemical bond using ultrafast lasers", *Nobel Lecture*, December 8, 1999.
- [10] T.W. Hansch, "A proposed sub-Femtosecond pulse synthesizer using separate phase-locked laser oscillators", *Opt. Comm.*, **80**, 71 (1990).
- [11] Gy. Farkas and Cs. Tóth, "Proposal for attosecond light pulse generation using laser-induced multiple-harmonic conversion processes in rare gases", *Phys. Lett. A*, **168**, 447-450, (1992).
- [12] O. Faucher, P. Tzallas, E.P. Benis, J. Kruse, A. Peralta Conde, C. Kalpouzos, and D. Charalambidis, "Four-dimensional investigation of the 2nd order volume autocorrelation technique", *Appl. Phys. B*, DOI 10.1007/s00340-009-3559-z, (2009).
- [13] Rick Trebino, "Frequency-Resolved Optical Gating: The Measurement of Ultrashort Laser Pulses", Springer (2002).
- [14] P. M. Paul, E.S. Toma, P. Breger, G. Mullot, F. Augé, Ph. Balcou, H.G. Muller, P. Agostini, "Observation of a train of attosecond pulses from high harmonic generation", *Science*, **Vol. 292**, no. 5522, pp. 1689-1692, (2001).
- [15] N. A. Papadogiannis, B. Witzel, C. Kalpouzos, and D. Charalambidis, "Observation of Attosecond Light Localization in Higher Order Harmonic Generation", *Physical Review Letters*, **83**, 4289 (1999).
- [16] T. Zuo, A. D. Bandrauk, and P. B. Corkum, "Laser induced electron diffraction: a new tool for probing ultrafast molecular dynamics", *Chem. Phys. Lett.* **259**, 313–320 (1996).
- [17] J. Itatani, et al., "Tomographic imaging of molecular orbitals". *Nature* **432**, 867–871 (2004).
- [18] M. Uiberacker et al., "Attosecond real-time observation of electron tunnelling in atoms", *Nature* **446**, 627–632 (2007).

- [19] M. Drescher et al., “Time-resolved atomic inner-shell spectroscopy”, *Nature* **419**, 803–807 (2002).
- [20] Paul Dirac, “*The Principles of Quantum Mechanics*”, Oxford University Press (1930).
- [21] Keldysh, L. V., 1964, *Zh. eksp. teor. Fiz.*, 47, 1945 [English translation: 1965, *Soviet Phys. JETP*, **20**, 1307].
- [22] Reiss H. R., 1980, *Phys. Rev. A*, 22, 1786; see also REISS H. R., 1992, *Prog. Quant. Electron.*, **16**, 1.
- [23] Faisal, F. H. M., 1973, *J. Phys. B*, 6, L89.
- [24] Volkov D.M., *Zs. f. Phys.*, 1935, V.94, 25.
- [25] Misha Yu Ivanov, Michael Spanner, and Olga Smirnova, “Anatomy of strong field ionization”, *Journal Of Modern Optics*, **52**, 165-184, (2005).
- [26] M. Ammosov, N. B. Delone, and V. P. Krainov, “Tunnel ionization of complex atoms and atomic ions in a varying electromagnetic-field,” *Sov. Phys. JETP-USSR*, **91**, 6, 2008–2013 (1986).
- [27] A. McPherson, G. Gibson, H. Jara, U. Johann, T.S. Luk, I.A. McIntyre, K. Boyer, and C.K. Rhodes, “Studies of multiphoton production of vacuum-ultraviolet radiation in the rare gases”, *J. Opt. Soc. Am B*, **4**, 595 (1987).
- [28] Ferray, M. et al., “Multiple-harmonic conversion of 1064-nm radiation in rare gases”, *J. Phys. B* **21**, L31–L35 (1988).
- [29] P. Agostini, F. Fabre, G. Mainfray, G. Petite, & N. K. Rahman, “Free-free transitions following 6-photon ionization of xenon atom”. *Phys. Rev. Lett.* **42**, 1127–1130 (1979).
- [30] Kulander, K. C. & Shore, B. W. “Calculations of multiple-harmonic conversion of 1064-nm radiation in Xe”, *Phys. Rev. Lett* **62**, 524–526 (1989).
- [31] Shore, B. W. & Knight, P. L. “Enhancement of high optical harmonics by excess-photon ionization”, *J. Phys. B* **20**, 413–423 (1987).
- [32] Gontier, Y. & Trahin, M. “Frequency-conversion involving Raman-like processes above the ionization threshold”, *IEEE J. Quant. Electron.* **18**, 1137–1145 (1982).
- [33] Kuchiev, M. Y. “Atomic antenna”, *JETP Lett.* **45**, 404–406 (1987).
- [34] P. B. Corkum, “Plasma Perspective on Strong-Field Multiphoton Ionization”, *Phys. Rev. Lett* **71**, 1994 (1993).
- [35] K. C. Kulander, K. J. Schafer, and J. L. Krause, in *Proceedings of the Workshop, Super Intense Laser Atom Physics (SILAP) III*, edited by B. Piraux, A. L’Huillier and J. Rzaewski (Plenum Press, New York) (1993).
- [36] M. Lewenstein, Ph. Balcou, M. Yu. Ivanov, Anne L’Huillier, and P. B. Corkum, “Theory of high-harmonic generation by low-frequency laser fields”, *Physical Review A*, **49**, 2117 (1994).
- [37] Zenghu Chang, “*Fundamental of Attosecond Optics*”, CRC Press (2011).
- [38] P. Salieres, T. Ditmire, M.D. Perry, A. L’Huillier, and M. Lewenstein, “Angular distributions of high-order harmonics generated by a femtosecond laser”, *J.Phys.B: At. Mol. Opt. Phys.* **29**, 4771-4786, (1996).

- [39] Zenghu Chang, "Controlling attosecond pulse generation with a Double Optical Gating", *Physical Review A* **76**, 051403(R) (2007).
- [40] Th. Auguste, P. Monot, L.A. Lompré, G. Mainfray, and C. Manus, *J. Phys. B* **25**, 4181 (1992).
- [41] M. Lewenstein, P. Salieres, A. L'Huillier, "Phase of the atomic polarization in high-order harmonic generation", *Physical Review A*, **52**, 4747 (1995).
- [42] D.B. Milosevic, W. Becker, "Role of long quantum orbits in high-order harmonic generation", *Physical Review A*, **66**, 063417 (2002).
- [43] P. Debye, "Näherungsformeln für die Zylinderfunktionen für grosse Werte des Arguments und unbeschränkt veränderliche Werte des Index" *Math. Ann.*, **67**, pp. 535–558 (1909).
- [44] Philippe Balcou, Pascal Salieres, Anne L'Huillier, and Maciej Lewenstein, "Generalized phase-matching conditions for high harmonics: The role of field-gradient forces", *Physical Review A*, **55**, 3204 (1997).
- [45] J.W.G. Tisch, R.A. Smith, J.E. Muffet, M. Ciarrocca, J.P. Marangos, and M.H.R. Hutchinson, "Angularly resolved high-order harmonic generation in helium", *Phys. Rev. A*, **49**, R28 (1994).
- [46] J. Peatross and D.D. Meyerhofer, "Angular distribution of high-order harmonics emitted from rare gases at low density", *Phys. Rev. A*, **51**, R906 (1995).
- [47] P. Salieres, T. Ditmire, K.S. Budil, M.D. Perry, and A. L'Huillier, "Spatial profiles of high-order harmonics generated by a femtosecond Cr:LiSAF laser", *J.Phys.B* **27**, L217 (1994).
- [48] A. E. Siegman, *Lasers* (University Science, Mill Valley, California, 1986).
- [49] P. Salieres, A. L'Huillier, and M. Lewenstein, "Coherence Control of High-Order Harmonics", *Physical Review Letters*, **74**, 3776 (1995).
- [50] Philippe Antoine, Anne L'Huillier, and Maciej Lewenstein, "Attosecond Pulse Trains Using High-Order Harmonics", *Physical Review Letters* **77**, 1234 (1996).
- [51] M. Bellini, C. Lynga, A. Tozzi, M.B. Gaarde, T.W. Hansch, A. L'Huillier, and C.G. Wahlstrom, "Temporal Coherence of Ultrashort High-Order Harmonic Pulses", *Physical Review Letters*, **81**, 297 (1998).
- [52] M. Protopapas, C. H. Keitel, and P. L. Knight, "Atomic physics with super-high intensity lasers", *Rep. Prog. Phys.* **60**, 389-486 (1997).
- [53] Anne L'Huillier et al., "High-order harmonic-generation cutoff", *Physical Review A* **48**, R3433 (1993)
- [54] F. Krausz and M. Ivanov. "Attosecond physics". *Rev.Mod. Phys.*, **81**:163–234, (2009).
- [55] D. Shafir, H. Soifer, B.D. Brunner, M. Dagan, Y. Mairesse, S. Patchkovskii, M.Yu. Ivanov, O. Smirnova, and N. Dudovich, "Resolving the time when an electron exits a tunnelling barrier", *Nature* **485**, 343 (2012).
- [56] O. Raz et al., *Nature Phot.* **6**, 170 (2012).
- [57] P. Salieres et al., *Science* **292**, 902 (2001).
- [58] Y. Mairesse, A. de Bohan, L. J. Frasinski, H. Merdji, L. C. Dinu, P. Monchicourt, P. Breger, M. Kovacev, R. Taieb, B. Carr, H. G. Muller, P. Agostini, and P. Salieres. "Attosecond synchronization of high-harmonic soft x-rays". *Science*, **302**(5650):1540–1543, (2003).
- [59] M. Schultze, B. Bergues, H. Schröder, F. Krausz, and K. L. Kompa. "Spatially resolved measurement

- of ionization yields in the focus of an intense laser pulse". *New Journal of Physics*, 13(3):033001, (2011).
- [60] N.N. Das Gupta and M.L. De, "The electron microscope - its past and present", (1968)
- [61] W. Hittorf, *Ann.Phys.Lpz.*, **134**, 8 (1868).
- [62] E. Goldstein, *Berlin Monat*, 284 (1876).
- [63] W. Crookes, *Phil. Trans. Roy. Soc.*, **170**, 135 (1879).
- [64] H. Hertz, *Wiederman's Annalen*, **19**, 782 (1883).
- [65] Ph. Lenard, *Ann. der Phys.*, **51**, 225 (1894).
- [66] J. Perrin, *C.R. Acad. Sci. Paris*, **121**, 1130 (1895).
- [67] J.J. Thomson, *Phil. Mag.*, **44**, 293 (1897).
- [68] E. Wiechert, *Ann. der Phys.*, **69**, 739 (1899).
- [69] H. Busch, *Ann. Phys. Lpz.*, **81**, 974 (1926).
- [70] H. Busch, *Arch. Electrotech.*, **18**, 583 (1927).
- [71] C. J. Davisson and C. J. Calbick, *Phys. Rev.*, **38**, 585 (1931).
- [72] E. Bruche and H. Johannson, *Ann. Phys.*, **15**, 145, (1932).
- [73] Figure reprinted from F. Hinterberger, *Physik der Teilchenbeschleuniger und Ionenoptik*, Springer-Verlag Berlin, 1997
- [74] A. Adams and F.H. Read, "Electrostatic cylinder lenses II: Three element einzel lenses", *Journal of Physics E: Scientific Instruments*, Volume 5, Printed in Great Britain, (1972).
- [75] E. J. Takahashi, et al. "High-throughput, high-damage-threshold broadband beam splitter for high-order harmonics in the extreme-ultraviolet region", *Opt. Lett.* **29**, 507 (2004).
- [76] C. Vozzi, et al. "Generalized molecular orbital tomography", *Nature Phys.* **7**, 822 (2011).
- [77] P. Tzallas, E. Skantzakis, L. A. A. Nikolopoulos, G. D. Tsakiris, and D. Charalambidis. "Extreme-ultraviolet pump-probe studies of one-femtosecond-scale electron dynamics". *Nat. Phys.*, **7**:781, (2011).
- [78] C. Corsi, A. Pirri, E. Sali, A. Tortora, and M. Bellini, "Direct Interferometric Measurement of the Atomic Dipole Phase in High-Order Harmonic Generation", *Phys. Rev.Lett.* **97**, 023901 (2006).
- [79] C. M. Heyl, J. Gudde, U. Hofer, and A. L'Huillier, "Spectrally Resolved Maker Fringes in High-Order Harmonic Generation", *Phys. Rev. Lett.* **107**, 033903 (2011).
- [80] Max Born and Emil Wolf. "Principles of Optics". Pergamon Press, Oxford, (1985).
- [81] K.J. Schafer, B. Yang, L.F. DiMauro, and K.C. Kulander, "Above Threshold Ionization Beyond the High Harmonic Cutoff", *Phys. Rev. Lett.* **70**, 1599 (1993).
- [82] Emmanouil Skantzakis, *phD Thesis*, University of Crete (2011).
- [83] A. Zair, M. Holler, A. Guandalini, F. Schapper, J. Biegert, L. Gallmann, U. Keller, A.S. Wyatt, A.

Monmayrant, I.A. Walmsley, E. Cormier, T. Auguste, J.P. Caumes, P. Salières, “Quantum Path Interferences in High-Order Harmonic Generation”, *Phys. Rev. Lett.* **100**, 143902 (2008).

[84] M. B. Gaarde, J. L. Tate and K. J. Schafer, “Macroscopic aspects of attosecond pulse generation”, *J. Phys. B* **41**, 132001 (2008).

[85] K. Varjú, Y. Mairesse, B. Carré, M. B. Gaarde, P. Johnsson, S. Kazamias, R. López-Martens, J. Mauritsson, K. J. Schafer, Ph. Balcou, A. L’huillier and P. Salières, “Frequency chirp of harmonic and attosecond pulses”, *J. Mod. Opt.* **52**, 379 (2005).

[86] R. Zerne, C. Altucci, M. Bellini, M.B. Gaarde, T.W. Hansch, Anne L’Huillier, C. Lynga, and C.-G. Wahlstrom, “Phase-Locked High-Order Harmonic Sources”, *Phys. Rev. Lett.* **79**, 1006 (1997).

[87] M. Bellini and T.W. Hansch, *Appl. Phys. B*, **65**, 677 (1997).

[88] I.K. Kominis, G. Kolliopoulos, D. Charalambidis, P. Tzallas, “Quantum Information Processing at the Attosecond Timescale”, (to be submitted).

[89] X.F. Li, A. L’Huillier, M. Ferray, L.A. Lompré, and G. Mainfray, “Multiple-harmonic generation in rare gases at high laser intensity”, *Physical Review A*, **39**, 5751 (1989).

[90] Anne L’Huillier and Ph. Balcou, “High-Order Harmonic Generation in Rare Gases with a 1-ps 1053-nm Laser”, *Physical Review Letters*, **70**, 774 (1993).

[91] M. Hentschel, R. Kienberger, Ch. Spielmann, G. A. Reider, N. Milosevic, T. Brabec, P. Corkum, U. Heinzmann, M. Drescher, and F. Krausz. “Attosecond metrology”. *Nature*, 414:509–513, (2001).

[92] A. Baltuska, Th. Udem, M. Uiberacker, M. Hentschel, E. Goulielmakis, Ch. Gohle, R. Holzwarth, V. S. Yakovlev, A. Scrinzi, T. W. Hansch, and F. Krausz. “Attosecond control of electronic processes by intense light fields”. *Nature*, 421:611, (2003).

[93] F. Quéré, J. Itatani, G.L. Yudin, and P.B. Corkum. “Temporal characterization of attosecond pulses”. In Ferenc Krausz, Georg Korn, Paul Corkum, and Ian A. Walmsley, editors, *Ultrafast Optics IV*, volume 95 of *Springer Series in OPTICAL SCIENCES*, pages 259–270. Springer New York, (2004).

[94] H.G. Muller. “Reconstruction of attosecond harmonic beating by interference of two-photon transitions”. *Appl. Phys. B*, 74:s17–s21, (2002).

[95] Y. Mairesse and F. Quéré. “Frequency-resolved optical gating for complete reconstruction of attosecond bursts”. *Phys. Rev. A*, 71:011401, (Jan 2005).

[96] Markus Drescher, Michael Hentschel, Reinhard Kienberger, Gabriel Tempea, Christian Spielmann, Georg A. Reider, Paul B. Corkum, and Ferenc Krausz. “X-ray pulses approaching the attosecond frontier”. *Science*, 291(5510):1923–1927, (2001).

[97] R. Kienberger, E. Goulielmakis, M. Uiberacker, A. Baltuska, V. Yakovlev, F. Bammer, A. Scrinzi, Th. Westerwalbesloh, U. Kleineberg, U. Heinzmann, M. Drescher, and F. Krausz. “Atomic transient recorder”. *Nature*, 427:817–821, (2004).

[98] E. Goulielmakis, M. Uiberacker, R. Kienberger, A. Baltuska, V. Yakovlev, A. Scrinzi, Th. Westerwalbesloh, U. Kleineberg, U. Heinzmann, M. Drescher, and F. Krausz. “Direct measurement of light waves”. *Science*, 305:1267–1269, (2004).

[99] J. Gagnon, E. Goulielmakis, and V.S. Yakovlev. “The accurate FROG characterization of attosecond pulses from streaking measurements”. *Applied Physics B*, 92:25–32, (2008).

- [100] Y. Kobayashi, T. Sekikawa, Y. Nabekawa, and S. Watanabe. “27-fs extreme ultraviolet pulse generation by high-order harmonics”. *Opt. Lett.*, 23(1):64–66, (Jan 1998).
- [101] P. Tzallas, D. Charalambidis, N. A. Papadogiannis, K. Witte, and G. D. Tsakiris. “Direct observation of attosecond light bunching”. *Nature*, 426:267–271, (2003).
- [102] Yasuo Nabekawa, Toshihiko Shimizu, Tomoya Okino, Kentaro Furusawa, Hirokazu Hasegawa, Kaoru Yamanouchi, and Katsumi Midorikawa. “Conclusive evidence of an attosecond pulse train observed with the mode-resolved autocorrelation technique”. *Phys. Rev. Lett.*, 96:083901, (Feb 2006).
- [103] Y. Nomura, R. Horlein, P. Tzallas, B. Dromey, S. Rykovanov, Zs. Major, J. Osterhoff, S. Karsch, L. Veisz, M. Zepf, D. Charalambidis, F. Krausz, and G. D. Tsakiris. “Attosecond phase-locking of harmonics emitted from laser-produced plasmas”. *Nat. Phys.*, 5(2):124–128, (2009).
- [104] Yasuo Nabekawa, Toshihiko Shimizu, Tomoya Okino, Kentaro Furusawa, Hirokazu Hasegawa, Kaoru Yamanouchi, and Katsumi Midorikawa. “Interferometric autocorrelation of an attosecond pulse train in the single-cycle regime”. *Phys. Rev. Lett.*, 97:153904, (Oct 2006).
- [105] P. Heissler, P. Tzallas, J. M. Mikhailova, K. Khrennikov, L. Waldecker, F. Krausz, S. Karsch, D. Charalambidis, and G. D. Tsakiris. “Two-photon above-threshold ionization using extreme-ultraviolet harmonic emission from relativistic laserplasma interaction”. *New Journal of Physics*, 14(4):043025, (2012).
- [106] Katsumi Midorikawa, Yasuo Nabekawa, and Akira Suda. “XUV multiphoton processes with intense high-order harmonics”. *Progress in Quantum Electronics*, 32(2):43 – 88, (2008).
- [107] P. A. Carpeggiani, P. Tzallas, A. Palacios, D. Gray, F. Martín, and D. Charalambidis. “Tracing molecular dynamics at the femto-/atto-second boundary through extreme-ultraviolet pump-probe spectroscopy”. *ArXiv:1304.6914*.
- [108] I. Grguras, A. R. Maier, C. Behrens, T. Mazza, T. J. Kelly, P. Radcliffe, S. Dusterer, A. K. Kazansky, N. M. Kabachnik, Th. Tschentscher, J. T. Costello, M. Meyer, M. C. Hoffmann, H. Schlarb, and A. L. Cavalieri. “Ultrafast x-ray pulse characterization at free-electron lasers”. *Nat. Photon.*, 6(12):852–857, (2012).
- [109] Y. Mairesse, O. Gobert, P. Breger, H. Merdji, P. Meynadier, P. Monchicourt, M. Perdrix, P. Salieres, and B. Carré. “High harmonic xuv spectral phase interferometry for direct electric-field reconstruction”. *Phys. Rev. Lett.*, 94:173903, (May 2005).
- [110] Eric Cormier, Ian A. Walmsley, Ellen M. Kosik, Adam S. Wyatt, Laura Corner, and Louis F. DiMauro. “Self-referencing, spectrally, or spatially encoded spectral interferometry for the complete characterization of attosecond electromagnetic pulses”. *Phys. Rev. Lett.*, 94:033905, (Jan 2005).
- [111] J. Janszky, G. Corradi, and R.N. Gyuzalian. “On a possibility of analysing the temporal characteristics of short light pulses”. *Optics Communications*, 23(3):293 – 298, (1977).
- [112] F. Salin, P. Georges, G. Roger, and A. Brun. “Single-shot measurement of a 52-fs pulse”. *Appl. Opt.*, 26(21):4528–4531, (Nov 1987).
- [113] P. Simon, H. Gerhardt, and S. Szatmari. “A single-shot autocorrelator for uv femtosecond pulses”. *Measurement Science and Technology*, 1(7):637, (1990).
- [114] A. Brun, P. Georges, G. Le Saux, and F. Salin. “Single-shot characterization of ultrashort light pulses”. *Journal of Physics D: Applied Physics*, 24(8):1225, (1991).
- [115] L. A. A. Nikolopoulos, E. P. Benis, P. Tzallas, D. Charalambidis, K. Witte, and G. D. Tsakiris. “Second order autocorrelation of an XUV attosecond pulse train”. *Phys. Rev. Lett.*, 94:113905, (Mar 2005).

- [116] P. Heissler, R. Horlein, J. M. Mikhailova, L. Waldecker, P. Tzallas, A. Buck, K. Schmid, C. M. S. Sears, F. Krausz, L. Veisz, M. Zepf, and G. D. Tsakiris. “Few-cycle driven relativistically oscillating plasma mirrors: A source of intense isolated attosecond pulses”. *Phys. Rev. Lett.*, 108:235003, (Jun 2012).
- [117] N.A. Papadogiannis, L.A.A. Nikolopoulos, D. Charalambidis, G.D. Tsakiris, P. Tzallas, and K. Witte. “On the feasibility of performing non-linear autocorrelation with attosecond pulse trains”. *Applied Physics B*, 76(7):721–727, (2003).
- [118] Alejandro Saenz and P. Lambropoulos. “Theoretical two- three- and four-photon ionization cross sections of helium in the xuv range”. *Journal of Physics B: Atomic, Molecular and Optical Physics*, 32(23):5629, (1999).
- [119] S. E. Harris, J. J. Macklin, and T. W. Hensch, *Opt. Commun.* **100**, 487 (1993).
- [120] P. B. Corkum, N. H. Burnett, and M. Y. Ivanov, *Opt. Lett.* **19**,1870 (1994);
- [121] P. Antoine, A. L’Huillier, M. Lewenstein, P. Salières, and B. Carre, *Phys. Rev. A* **53**, 1725 (1996).
- [122] Bing Shan, Shambhu Ghimire, and Zenghu Chang, *Phys. Rev. A* **69**, 021404(R) (2004).
- [123] V.T. Platonenko and V.V. Strelkov, “Generation of a single attosecond X-Ray pulse”, *Quantum Electron.* 28, 749 (1998)
- [124] V. T. Platonenko and V. V. Strelkov, “Single attosecond soft-x-ray pulse generated with a limited laser beam” *J. Opt. Soc. Am. B* **16**, 435 (1999).
- [125] P. Tzallas et al. “Generation of intense continuum extreme-ultraviolet radiation by many-cycle laser fields”, *Nature Physics* **3**, 846 (2007).
- [126] E. Skantzakis, P. Tzallas, J. Kruse, C. Kalpouzos, and D. Charalambidis, “Coherent continuum extreme-ultraviolet radiation in the sub-100-nJ range generated by a high-power many cycle laser field”, *Opt. Lett.* **34**,1732 (2009).
- [127] O. Tcherbakoff et al. “Time-gated high-order harmonic generation”, *Phys. Rev. A* **68**, 043804 (2003)
- [128] V.V. Strelkov et al. “Generation of Attosecond Pulses with ellipticity-modulated fundamental”, *Appl. Phys. B* **78**, 879 (2004)
- [129] V.V. Strelkov et al. “Single attosecond pulse production with an ellipticity-modulated driving IR pulse”, *J. Phys B* **38**, L161 (2005)
- [130] G. Kolliopoulos et al. “A compact collinear polarization gating scheme for many cycle laser pulses”, *Review of Scientific Instruments* **83**, 063102 (2012)
- [131] I.J. Sola et al. “Controlling attosecond electron dynamics by phase-stabilized polarization gating”, *Nature Phys.* **2**, 319 (2006)
- [132] “Handbook of Optical Constants of Solids”, edited by Edward D. Palik, Naval Research Laboratory Washington D.C.
- [133] J.E. Kruse et al. “Persistent quantum interfering electron trajectories”, *Phys. Rev. A* **82**, 033438 (2010).
- [134] J.E. Kruse et al. “Inconsistencies between two attosecond pulse metrology methods: A comparative study”, *Phys. Rev. A* **82**, 021402(R) (2010).
- [135] C.G. Wahlstrom et al. “High-order harmonic generation in rare gases with an intense short-pulse

laser”, *Phys. Rev. A* **48**, 4709 (1993).

[136] D. Charalambidis et al., “Exploring intense attosecond pulses”, *New J. Phys.* **10**, 025018 (2008).

[137] Anne L’Huillier, K.J. Schafer and K.C. Kulander; “High-order Harmonic Generation in Xenon at 1064nm: The Role of Phase-Matching”, *Phys. Rev. Lett* **66**, 2200 (1991).

[138] P. Tzallas et al *Progress in Ultrafast Intense Laser Science*, Springer, Book chapter 8, p.163 (2011).